# Concentration and Size Distribution of Microparticles in the NGRIP Ice Core (Central Greenland) during the Last Glacial Period

Dissertation
zur Erlangung des
Doktorgrades der Naturwissenschaften

im Fachbereich Geowissenschaften
der Universität Bremen

vorgelegt von

Urs Ruth

Bremen, im April 2002

**Urs Ruth**

Institut für Umweltphysik
Universität Heidelberg
Im Neuenheimer Feld 229
D-69120 Heidleberg
Urs.Ruth@iup.uni-heidelberg.de

Alfred-Wegener-Institut
für Polar- und Meeresforschung
Columbusstraße
D-27568 Bremerhaven

This is a reprint of a dissertation submitted to the
Department of Geosciences of the University of Bremen in April 2002.
It is published as report number 428 of the *Berichte zur Polar- und Meeresforschung* (ISSN 1618-3193). It is available electronically at:
http://www.ub.uni-heidelberg.de/archiv/2291

Die vorliegende Arbeit ist die inhaltlich unveränderte Fassung einer Dissertation, die im April 2002 dem Fachbereich Geowissenschaften der Universität Bremen vorgelegt wurde.
Sie ist in den *Berichten zur Polar- und Meeresforschung* (ISSN 1618-3193) als Band Nummer 428 veröffentlicht Die Arbeit ist elektronisch erhältlich unter:
http://www.ub.uni-heidelberg.de/archiv/2291

# Contents

# Abstract

The concentration and size distribution of mineral microparticles were investigated in the deep North Greenland Ice Core Project (NGRIP) ice core continuously from 1405 m to 2930 m depth. The measurements were accomplished using a novel, optical detector which is based on laser light attenuation by individual particles. The device works on a flow-through basis, and together with sample preparation via continuous melting it allows for very time efficient analyses at high depth resolution. The presented work also covers the partial development and the application of a continuous ice core melting setup as well as analytical systems of electrolytical conductivity and acidity.

In the NGRIP ice core, the concentration of microparticles was found to be around 70 $\mu$g kg$^{-1}$ during Preboreal Holocene and 8000 $\mu$g kg$^{-1}$ during the last glacial maximum (LGM). Variations by typically a factor of 8 of the insoluble particle mass and number concentrations were encountered across the rapid Dansgaard/Oeschger transitions within the last glacial period.

The ($Ca^{2+}$)/(insoluble microparticle) mass ratio was investigated in various selected core sections. Relatively low $Ca^{2+}$ contents were found concurring with high crustal concentrations. Such systematic variations were observed on long time scales ($>$ 1000 years) and also on seasonal to multi-annual time scales. Strong enhancements of the ($Ca^{2+}$)/(insoluble microparticle) ratio by up to a factor of 3 were found during volcanic events due to increased dissolution of $CaCO_3$ by volcanogenic acids. These findings limit the use of $Ca^{2+}$ as an unequivocal quantitative reference species for mineral dust.

Systematic variations of the size distribution were observed with the tendency towards larger particles during colder climates. The lognormal mode of the volume distribution was found at about 1.3 $\mu$m diameter during Preboreal Holocene and 1.7 $\mu$m diameter during peak LGM. Size changes occurred largely synchronous with concentration changes. By use of a simple, semi-quantitative model picture it is inferred that (i) the observed variations mainly reflect changes of the airborne particle size distribution over Greenland, and that (ii) these size changes probably are a consequence of changed particle transit times from the source to the ice sheet. Long range transport times shorter by 25% during the LGM with respect to Preboreal Holocene can explain the observed size changes. Further, it is estimated that these changes in transport can account for a concentration increase of less than 1 order of magnitude and clearly cannot explain the total observed concentration increase during LGM. Therefore, source intensifications must have occurred synchronously to changes of long range transport. Furthermore, a higher variability of the lognormal mode was observed during warmer climates as reflected by increased point-to-point variability and also by increased distribution widths for the multi-year samples considered. It thus is inferred that atmospheric circulation was more variable during such times.

# Kurzzusammenfassung

Die Konzentration und Größenverteilung mineralischer Mikropartikel wurde im tiefen Eisbohrkern des North Greenland Ice Core Project (NGRIP) kontinuierlich von 1405 m bis 2930 m Tiefe untersucht. Die Messungen wurden mit einem neuartigen, optischen Detektor durchgeführt, dessen Nachweisverfahren auf der Abschwächung von Laserlicht durch einzelne Partikel beruht. Das Gerät arbeitet im kontinuierlichen Durchfluss, und in Verbindung mit einer kontinuierlichen Schmelzapparatur ermöglicht es sehr Zeit-effiziente Analysen bei gleichzeitig hoher Tiefenauflösung. Die vorliegende Arbeit umfasst außerdem die teilweise Entwicklung sowie die Anwendung von einer kontinuierlichen Eiskern-Schmelzapparatur und von Analysesystemen für elektrolytische Gesamtleitfähigkeit und Azidität.

Im NGRIP Eiskern betrug die Mikropartikelkonzentration ca. 70 $\mu$g kg$^{-1}$ während des präborealen Holozäns und ca. 8000 $\mu$g kg$^{-1}$ während des letzten glazialen Maximums (LGM). Starke Variationen der Massen- und Anzahlkonzentration um typisch einen Faktor 8 wurden während der eiszeitlichen Dansgaard/Oeschger-Ereignisse festgestellt.

Das Massenverhältnis ($Ca^{2+}$)/(unlösliche Partikel) wurde in mehreren Tiefenhorizonten untersucht. Relativ niedrige $Ca^{2+}$-Gehalte wurden während hoher Staubkonzentrationen beobachtet. Solche systematischen Variationen wurden sowohl auf langen Zeitskalen (> 1000 Jahre) als auch auf saisonalen bis multiannualen Zeitskalen festgestellt. Erhöhungen des ($Ca^{2+}$)/(unlösliche Partikel)-Verhältnisses um mehr als einen Faktor 3 wurden in Vulkanhorizonten beobachtet und sind vermutliche auf verstärkte Auflösung von $CaCO_3$ durch vulkanogene Säure zurückzuführen. Dies schränkt die Verwendung von $Ca^{2+}$ als eindeutige, quantitative Referenz für Mineralstaub ein.

Es wurden systematische Variationen der Größenverteilung beobachtet mit einem Trend zu größeren Partikeln in kälteren Klimaperioden. Die log-normale Mode der Volumenverteilung liegt im präborealen Holozän bei ca. 1.3 $\mu$m Durchmesser und bei ca. 1.7 $\mu$m Durchmesser im Hoch-LGM. Veränderungen von Größe und Konzentration treten weitgehend gleichzeitig auf. Mit Hilfe eines einfachen, halb-quantitativen Modellbildes kann geschlossen werden, dass (i) die beobachteten Größenvariationen hauptsächlich Veränderungen der luftseitigen Größenverteilung über Grönland widerspiegeln und dass (ii) diese Größenveränderungen vermutlich auf Veränderungen der Transportzeit der Partikel von der Quelle zum Eisschild zurück geführt werden können. Hierbei können um 25% kürzere Ferntransportzeiten während des LGMs die beobachtete Größenveränderung erklären. Desweiteren kann abgeschätzt werden, dass solche kürzeren Transportzeiten eine Konzentrationserhöhung von weniger als einer Größenordnung bewirken und nicht die beobachtete Konzentrationserhöhung während des LGMs erklären können. Daher müssen gleichzeitig zu Veränderungen des Ferntransportes auch Veränderungen der Quellstärke eingetreten sein. Außerdem wurde eine höhere Variabilität der log-normalen Mode während warmer Klimaperioden beobachtet; daraus kann geschlossen werden, dass die atmosphärische Zirkulation zu solchen Zeiten variabler gewesen ist.

# Chapter 1

# Introduction

Ice cores provide a wealth of paleo-climatic information. Well-stratified ice core records can reach back in time continuously for several 100 000 years. The spectrum of archived information is immense and reaches from stable isotope ratios of the water molecule, which allow a temperature reconstruction of the atmosphere, over past atmospheric aerosol content to greenhouse gas concentrations. This makes it possible to study past climates and the degree of natural climate variability.

The ice core record from Camp Century (North West Greenland) for example revealed large climatic fluctuations that occurred during the last glacial period with extremely rapid transitions between cold and warm states [*Dansgaard et al.*, 1969]. And the record from Vostok (East Antarctica) showed amongst other things that the present atmospheric concentration of the greenhouse gas $CO_2$ is unprecedented during the last 420 000 years and that also the current rate of increase exceeds that of previous, naturally occurring changes [*Petit et al.*, 1999].

Ice core research not only provides reconstructions of past environmental conditions. It also allows to study the causes and feed back mechanisms of past climate changes because multiple atmospheric trace species are stored in one archive simultaneously. The insights from ice core studies have a lot of implications for climate research and ultimately yield crucial information also for the understanding of today's climate. Such knowledge is essential for reliable assessments of anthropogenic climate change for the past as well as for the future.

The reconstruction of past atmospheric aerosol loads is a central topic in ice core research. Aerosols are solid or liquid particles suspended in the atmosphere. They have a driving influence on Earth's climate through multiple mechanisms (e.g. [*Prospero et al.*, 1983; *Ramanathan et al.*, 2001]). They enhance the scattering and absorption of solar radiation (direct climatic forcing), but they also produce brighter clouds that

reduce the amount of solar irradiance reaching the ground (indirect climatic forcing). This is also the case for the mineral dust aerosol (e.g. [*Sokolik et al.*, 2001]). Mineral dust deposited in Greenland consists of windblown microparticles that are entrained into the atmosphere during dust storms and are carried long distances. The main source of mineral dust transported to Greenland has been traced to the East Asian deserts [*Biscaye et al.*, 1997].

The concentration of dust in Greenlandic ice cores was found 100-fold increased during the Last Glacial Maximum (LGM, about 20 000 years ago) compared to present day (e.g. [*Steffensen*, 1997]), which involved strong alterations of paleoclimatic forcings. Yet, the mineral dust concentrations are not only a climatic forcing factor, they also are indicative for past climatic situations. However, the reasons for the strong increase observed are still disputed. In particular it is uncertain to which extend it was caused by enhanced source strength (which would imply an increased atmospheric dust load along the whole transport pathway) or to which extent it resulted from more efficient transport of dust to Greenland (which would imply an increased dust load at high latitudes especially but less so at lower latitudes).

Mineral dust holds a soluble and an insoluble fraction, the latter of which also is called '(insoluble) microparticles'. Calcium (Ca) is the most abundant element of the soluble fraction; and since $Ca^{2+}$ can be readily measured using standard ion chromatography (IC) the $Ca^{2+}$ ion concentration has often been taken as a proxy parameter for dust so far. However, the ratio of $Ca^{2+}$ to insoluble dust is known to be variable [*Steffensen*, 1997], and systematic investigations of this variability are needed. Such investigations have not been performed yet as not much data of the total, i.e. the soluble and insoluble dust mass have been available. This is because the Coulter counting technique, which is the standard measurement technique for insoluble microparticles, is very work intensive as well as susceptible to perturbations.

Dust permits not only the study of its concentration or composition but also of its size distribution. The size distribution is expected to be modified by the transport and deposition of particles. Therefore, archives of aeolian dust may allow far-reaching inferences on the properties of past atmospheric transport. However, until now the interpretation of observed changes of the size distribution has been poor and also not much data has been available.

The drilling of the North Greenland Ice Core Project (NGRIP) ice core enabled further investigations of the mineral dust aerosol in polar ice. The NGRIP drill site is located in central Greenland at (75.1N,42.3W) about 300 km NNW of the summit region on an ice divide. Figure 1.1 shows the location of the NGRIP core and other Greenlandic ice coring sites.

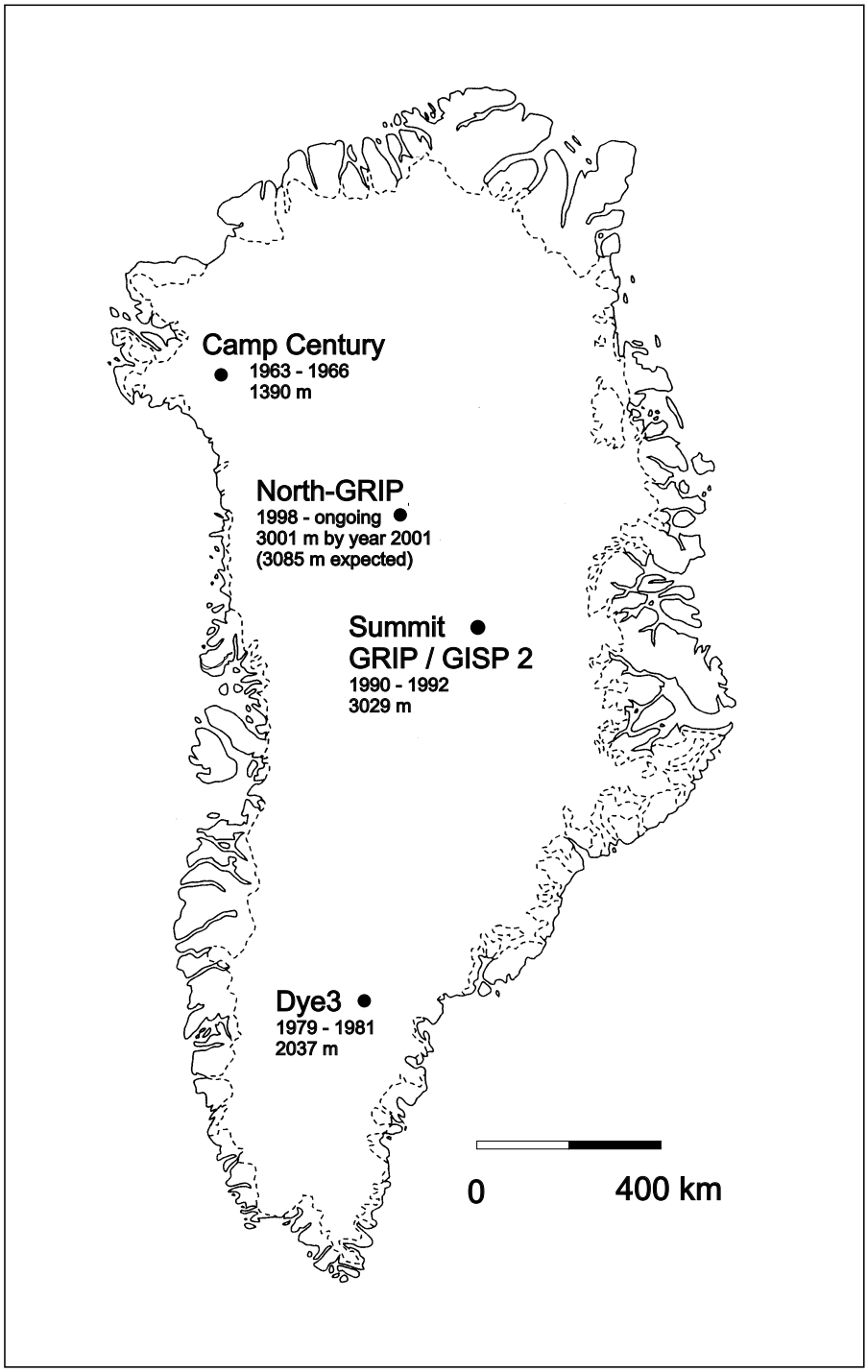


Figure 1.1: Map of Greenland showing the location of deep ice coring sites. Periods of active drilling and ice thicknesses are indicated. Modified after [*Fischer*, 1997].

During the NGRIP-2000 field season an analytical laboratory was operated and extensive analyses of tracer concentrations were performed. These included the deployment of a novel type of microparticle counter which is based on laser light attenuation. The new counter is easy handling and in combination with a continuous ice core melting setup allows for very efficient sample processing already in the field. This effort resulted in a high resolution profile of microparticle concentration and size distribution covering almost the entire last glacial period.

In this work, the novel particle detector is described, and a method of size calibration is presented (chapters 3, 4, 5, and appendix A). In case studies the $Ca^{2+}$ / (insoluble dust) mass ratio is investigated for long term as well as short term variations (chapter 4). In chapter 5 the microparticle concentration and size distribution profiles from the NGRIP core are presented and discussed. A highly simplified but quantitative model picture is developed for the interpretation of the particle size.

Chapter 6 is not directly connected to the NGRIP particle measurements. It deals with the conservation of atmospheric $HNO_3$ in ice cores and with post-depositional changes of the $NO_3$ concentration in polar ice.

The work of chapters 4 and 6 is in press at *Annals of Glaciology, Vol. 35*; the work presented in chapter 5 is submitted to the *Journal of Geophysical Research* for publication.

**Additional activities** In the course of this work extensive effort was put into the continuing development and operation of a continuous ice core melting setup for home laboratory applications. This not only included the analysis of microparticles, which is described methodically in chapter 3, but also the dedicated deployment of the electrolytical conductivity signal. Furthermore, a setup for the direct measurement of acidity was established. These developments were applied for comprehensive analyses of the 180 m long B25 ice core from Berkner Island (Antarctica) and several shallow firn cores from the new drilling cite in Severnaya Semlya (Russian Arctic). The Berkner Island core, which spans about the last 1200 years, was analyzed in a continuous flow type fashion for electrolytical conductivity, microparticle content, and $Ca^{2+}$- and $NH_4^+$-concentrations in subseasonal resolution. About 2000 discrete samples were automatically prepared and as yet have partly been measured for $F^-$, $MSA^-$, $Cl^-$, $NO_3^-$, $SO_4^{2-}$ and $H^+$ concentrations. This will be the basis for a core chronology through annual layer counting and is expected to reveal the history of the Weddell Sea region. The scientific results of these measurements will be presented elsewhere, however, selected methodical aspects are documented here in appendices B – D (in German).

# Chapter 2

# The mineral aerosol

## 2.1 Origin and composition

The mineral aerosol consists of mineral material suspended in the atmosphere. It may be present as fine grained particles or in a dissolved form within water droplets or ice crystals. In ice core analyses, a distinction between the soluble fraction and the insoluble one is useful, the latter of which is also referred to as mineral microparticles. Commonly, the mineral aerosol is also called mineral *dust*. It originates predominantly from large deserts or semiarid areas that are subject to wind erosion.

In the source areas loose, fine grained material is produced by weathering processes. *Pye* [1987] distinguishes between frost weathering, aeolian abrasion, insolation weathering, salt weathering, chemical weathering, and others. All theses mechanisms are not mutually exclusive but may occur in combinations with each other. Physical weathering causes the breakage of crystalline material due to increased mechanical stress. Chemical weathering causes the disintegration of parent material by dissolution along lines of crystal weakness through chemical reactions. Often $CO_2$ or organic acids present in the soil enhance this process. Physical weathering mechanisms tend to prevail in cold and arid climates, whereas chemical weathering is favored by warm and wet climates. The different types of weathering are therefore associated with different mineralogical compositions (e.g. kaolinite vs. chlorite).

The largest soluble fraction of aeolian dust is made up by Calcium carbonate $CaCO_3$. Therefore $Ca^{2+}$ ions are often taken as a proxy parameter for dust in ice cores. However, the elemental and mineralogical composition of dust underlies regional variations which also affects its Ca content. The Ca content of loesses, for example, ranges from below 10% to more than 30% [*Pye*, 1987]. The Aluminum content of crustal material is more homogeneous (about 8% for average continental crust [*Bowen*, 1979]).

Therefore, Al surely would be a better proxy for the concentration of the insoluble dust fraction, and probably also for the total dust concentration. But as oppose to Ca, Al cannot be measured easily by standard IC.

Archives of aeolian dust hold information on climatic situations in the source areas and about past wind fields. Terrestrial sediment profiles (e.g. [*Sarnthein*, 1978; *Lamy et al.*, 1999; *Lagroix and Banerjee*, 2002]), marine sediment cores (e.g. [*Janecek and Rea*, 1985; *Rea*, 1994]), and ice cores (e.g. [*Thompson and Mosley-Thompson*, 1981; *Steffensen*, 1997; *Petit et al.*, 1999]) have been studied as archives of aeolian dust. From these it has been inferred that during the last glacial period the atmospheric dust load was much higher and that wind or storm patterns may have been different.

Provenance studies of aeolian dust can be based on particle mineralogy and isotopic composition. The mineralogy depends on the parent material and on environmental conditions in the source areas (e.g. [*Maggi*, 1997]). The isotopic composition of mineral materials differs in rocks from different lithologies and geologic ages, which hold individual isotope ratios e.g. of $^{206}$Pb /$^{207}$Pb or $^{87}$Sr /$^{86}$Sr. As these ratios are preserved during weathering and transport they may be deployed to identify the source region of windblown microparticles. This was done by *Biscaye et al.* [1997] and *Grousset et al.* [1992] who thereby identify East Asian deserts respectively Patagonian deserts as the most probable source areas for dust carried to Greenland and Antarctica. For Greenland it seems surprising that neither the Sahara nor the North American deserts are the dominant sources. For dust transport during the Pleistocene, the role of East Siberia remains unclear to date. This region probably was ice free polar desert during the last glacial period [*Felzer*, 2001], however, no reference samples for isotopic comparisons have yet been available to confirm or negate its importance as a dust source to Greenland during the last glacial.

## 2.2 Entrainment

Wind erosion may take place on soils that are unprotected by vegetation and sufficiently dry. During a dust storm particles are moved horizontally, and three distinct modes of transport have been identified: surface creep, saltation and suspension [*Bagnold*, 1941]. Large soil particles (typically greater than 0.5 mm) move in a rolling fashion called *surface creep*, whereas smaller particles (typically 0.05 to 0.5 mm) move in a hopping manner called *saltation*. Fine particles (typically smaller than 0.05 mm) may remain in *suspension* for longer periods of time. About 50% to 80% of the total soil movement takes place through saltation, whereas only $\approx$ 1% of the total mass is

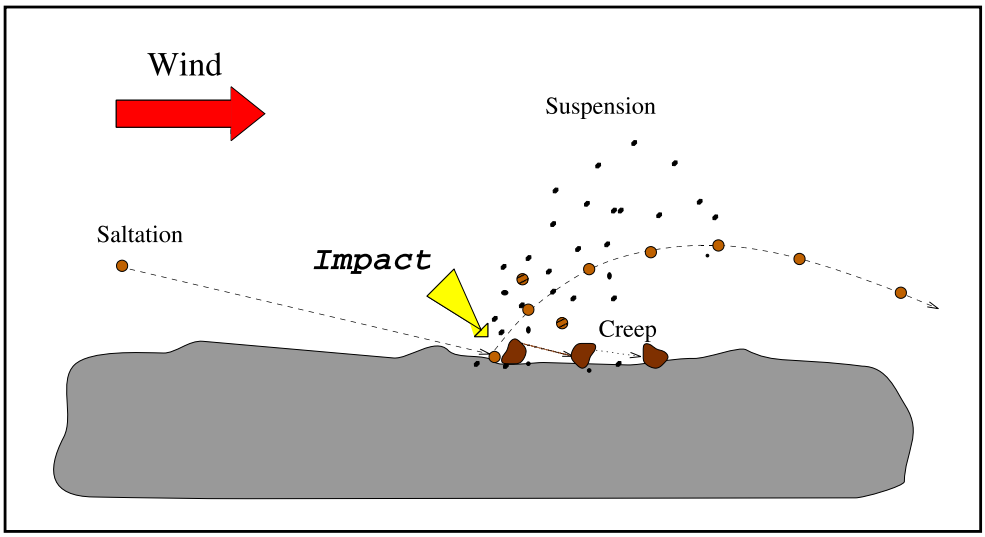


Figure 2.1: Schematic illustration of particle entrainment by saltation bombardment. Modified after [*Hua*, 1999].

moved by suspension [*Gillette et al.*, 1974]. Although suspension makes up only a small fraction of the total soil movement it is the only process that allows particles to get associated with long range transport and be carried long distances. These particles are usually referred to as *dust* particles, whereas the others are called *sand* particles.

Most notable is that saltating grains are a driving mechanism for all three modes of particle movement. This is illustrated in Figure 2.1. The saltating grains are usually lifted a few 10 cm above the ground and as they impact on the surface part of their kinetic energy is transferred to other particles. This may trigger surface creep and lift other small and fine particles into the air resulting in a chain reaction. This process is called saltation bombardment. It may also cause the disintegration of polycrystalline particles and thus the production of fine grained material.

The mobilization of dust underlies various environmental influences. First of all (and trivial) is the occurrence of strong surface winds or storms, and second the surface wind speed $u$ during such events. In field experiments the flux of fine particles was found to depend on $u^j$ with the exponent $j$ ranging from 2 [*Alfaro and Gomes*, 2001] to 4 [*Gillette and Passi*, 1988]. The efficiency of saltation bombardment crucially depends on soil moisture content, i.e. on the aridity of the source region. Further, the presence of non-erodible objects such as vegetation or rocks may be rate limiting, as they decrease the surface wind speed and act as catchers of particles yet aloft. The soil texture also plays an important role for dust production, as surface crusts lessen the amount of material available for mobilization. The entrainment of dust in general is a strongly

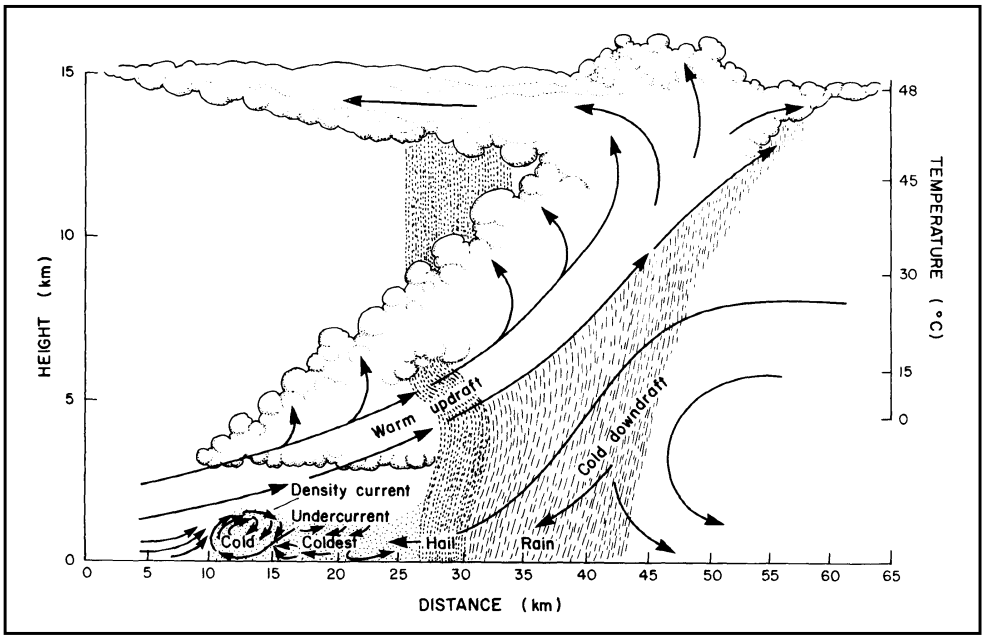


Figure 2.2: Schematic of a dust storm of the squall-line type; from [*Pye*, 1987].

episodic process with a few single events contributing almost the total annual flux.

## 2.3 Transport

Once lifted off the ground the small suspended microparticles may be lifted further to long range transport heights and carried long distances. During transport they are exposed to removal processes by wet and dry deposition. Wet deposition is all removal related to precipitation including in-cloud ("rain-out") and below-cloud ("wash-out") scavenging as well as nucleation scavenging, whereas dry removal includes e.g. sedimentation or impaction. Uplift may be very efficient in convective cells as sketched in Figure 2.2 but wet removal may also be very strong there. The tropics with the inner tropical convergence zone and with high rates of precipitation resemble an effective barrier against dust transport across the equator. This results in separate dust cycles in the northern and southern hemispheres.

Long range transport takes place above the planetary boundary layer. The dust is transported in dust plumes or hazes. For dust delivered to Greenland zonal transport from the East Asian source areas is achieved in the regions of the planetary westerly winds. Meridional transport into the polar cell is provided by the low pressure systems that develop along the polar front. During the last glacial period the temperature gradient between the Arctic and the tropics presumably was much stronger than today

due to a larger temperature difference between the polar regions and the tropics as well as due to an equatorward extended polar vortex. This resulted in increased baroclinicity and may have strengthened both the zonal as well as the meridional transport [*Andersen and Ditlevsen*, 1998; *Tegen and Rind*, 2000].

Dust transport to Greenland is influenced by the seasonal monsoon cycle in the source region and by the seasonal weakening and strengthening of the polar front around the Arctic. This leads to seasonally occurring so-called Arctic Haze-bands [*Rahn and Borys*, 1977] and also results in a strong seasonality of the dust flux to the Greenlandic ice sheet. This is mirrored by a pronounced maximum of the microparticle concentration in snow observed in late winter / early spring [*Steffensen*, 1985].

During transport significant in-cloud processing may occur. A large percentage of clouds evaporates again without producing rain. This may lead to a series of washing and coating for a particle. In cloud droplets the soluble fraction may be removed from the particle, and during subsequent evaporation of the droplet all dissolved material present may turn into a coating around the particle. Hereby the original composition of the particle is not necessarily restored as fractionating processes may occur or additional dissolved matter may have been present in the droplet. In-cloud processing is capable of changing the composition as well as the size distribution of airborne particles [*Wurzler et al.*, 2000].

Often archives of aeolian dust are interpreted in the context of atmospheric circulation. As *Rea* [1994] already pointed out it should be noted that dust storms occur most episodically. Therefore the information drawn from the dust deposits is characteristic for storm events predominately and not necessarily also for mean atmospheric flow.

## 2.4 Deposition

Aerosols are moved from the air to the ground by numerous processes, and a classification into wet and dry deposition is useful. Wet deposition is associated with precipitation events whereas dry deposition includes all processes not directly connected to precipitation.

Particles are incorporated into precipitation via several mechanisms: They are consumed as condensation nuclei during the formation of clouds. Further, Brownian diffusion especially causes small particles to move into already existing cloud droplets. In addition a "micro advection" of particles is caused by Stefan-flow, which is a stream of air and water vapor towards a condensing cloud droplet.

Apart from these in-cloud processes there is the below-cloud scavenging (or "wash-

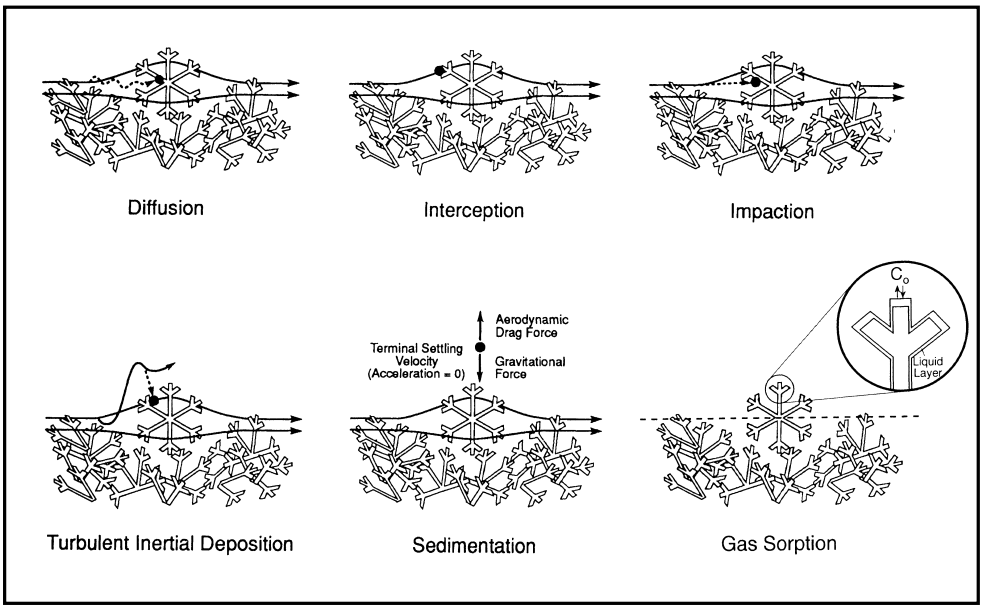


Figure 2.3: Illustration of dry deposition mechanisms for particles to snow; from [*Davidson et al.*, 1996].

out") of particles. Here, particles are removed from the atmosphere by falling precipitation. Large particles may be scavenged directly by the falling drop or crystal. For smaller particles aerodynamical influences become more important making direct scavenging impossible; however, very small particles may move into falling precipitation by diffusion processes.

Dry deposition mechanisms of particles to the snow are summarized in Figure 2.3. Sedimentation is the gravitational settling of particles in the atmosphere; it is most effective for large particles, whereas diffusion is significant only for small particles. Interception, impaction and turbulent inertial deposition are three varieties of inertial deposition. All these processes except sedimentation require a vertical concentration gradient of particles in the air above the ground and they may be rate limited through insufficient vertical exchange.

The dry and wet deposition flux of particles, i.e. the mass transferred per unit area and time, may be parameterized using effective dry and wet deposition velocities $v_D$ and $v_W$. Assuming temporally constant conditions (i.e. considering long term means only) the particle flux $F_D$ to the ice sheet due to dry deposition can be written as $F_D = v_D c_L$ (with $c_L$: concentration of particles in the air). Likewise the flux $F_W$ due to wet deposition can be expressed as $F_W = P c_N$ (with $P$: precipitation rate, and $c_N$: concentration of particles in new snow). With the scavenging ratio $\varepsilon = c_N/c_L$ the total flux $F$ can be expressed as $F = (v_D + \varepsilon P)c_L$. Approximating that the precipitation

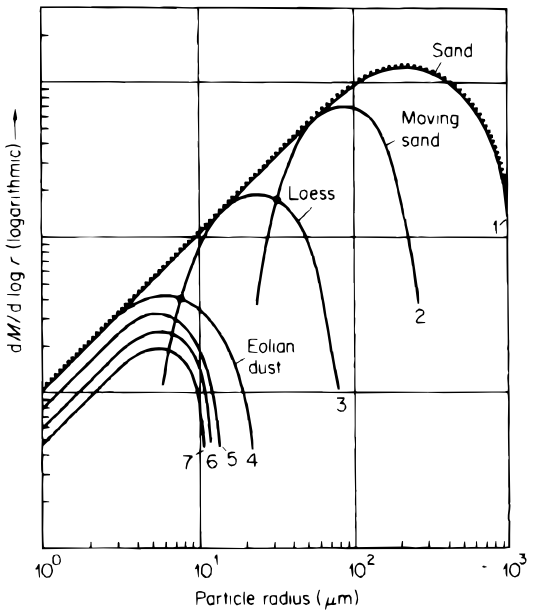


Figure 2.4: Size fractions of sand by wind induced transport, schematic. The original distribution 1 is fractionated into major fractions 2, 3, and 4 as a function of distance from the source. Curves 5, 6, and 7 depict the change in concentration due to both wet and dry removal from the atmosphere. The sum of curves 2, 3, and 4 should be equal to the original curve 1. From [*Junge*, 1979].

$P$ equals the accumulation $A$ this yields for the particle concentration $c_F$ in the firn: $c_F = F/A = (v_D/A + \varepsilon)c_L$. This expression may be used to infer $v_D$ and $\varepsilon$ from ice core studies if a systematic variation of $c_F$ with $A$ is encountered (e.g. [*Fischer et al.*, 1998; *Stanzick*, 2001]).

## 2.5 Size distribution

The size distribution of particulate matter in the source region susceptible to transport during a storm spans a very large range; it reaches from sub-micron to millimeter sized particles (see Figure 2.4). However, as already mentioned in section 2.2 the size range of particles that may remain suspended in the air for considerable time terminates at around 20 to 50 $\mu$m diameter. Therefore, the size distribution of the aeolian dust fraction is largely independent from that of the source itself.

*Gillette et al.* [1974] find that the wind speed has little influence on the size distribution of the airborne fraction in the investigated range from 2-10 $\mu$m diameter. And also *D'Almeida and Schütz* [1983] observe that dust storms do not change the size distribution of particles aloft below 10 $\mu$m diameter. Only above 10 $\mu$m the abundance

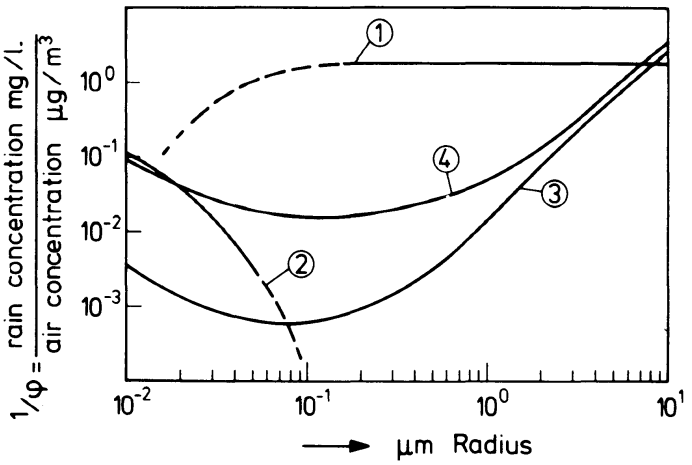


Figure 2.5: Calculated size fractionation due to precipitation. (1) nucleation, (2) attachment, (3) below cloud scavenging, (4) dry deposition. From [*Junge*, 1977].

of large airborne particles increases during strong surface winds. Because here only those particles are considered that are carried long distances the fraction larger than 10 $\mu$m may be disregarded. Therefore, it may be assumed that the size distribution of airborne particles a few meters above the ground is independent from the source strength.

Once airborne, the size distribution of an ensemble of particles may be changed by wet and dry deposition. All wet and dry removal processes are size fractionating and therefore modify the size distribution of the remaining particles. As large particles are preferentially removed the size distribution shifts towards smaller particles during long range transport. For the same reason the size distribution is shifted towards larger particles during deposition onto the ice sheet.

The size fractionation of wet removal mechanisms is depicted in Figure 2.5. It shows predictions of the scavenging efficiency depending on particle size for the most important processes. Curve (1) depicts the uptake of aerosols as condensation nuclei. Curve (2) describes the attachment to cloud droplets by Brownian diffusion and Stefan-flow. (3) is the pick up by falling raindrops (wash-out), and (4) is dry deposition.

Calculations of the dry deposition velocity are shown in Figure 2.6. Deposition is efficient for small particles due to their high diffusivity. Deposition is also high for large particles due to sedimentation; here, the deposition velocity has a slope of 2 in the log-log plot which reflects Stokes law of viscose friction. For intermediate sized particles the deposition is governed by inertial scavenging. This mechanism is influenced by the friction velocity $u_*$ and the surface roughness $z_0$ in a complicated way. As a rule of thumb, $u_*$ may be taken as a few percent of the average wind speed. $z_0$ may be taken as

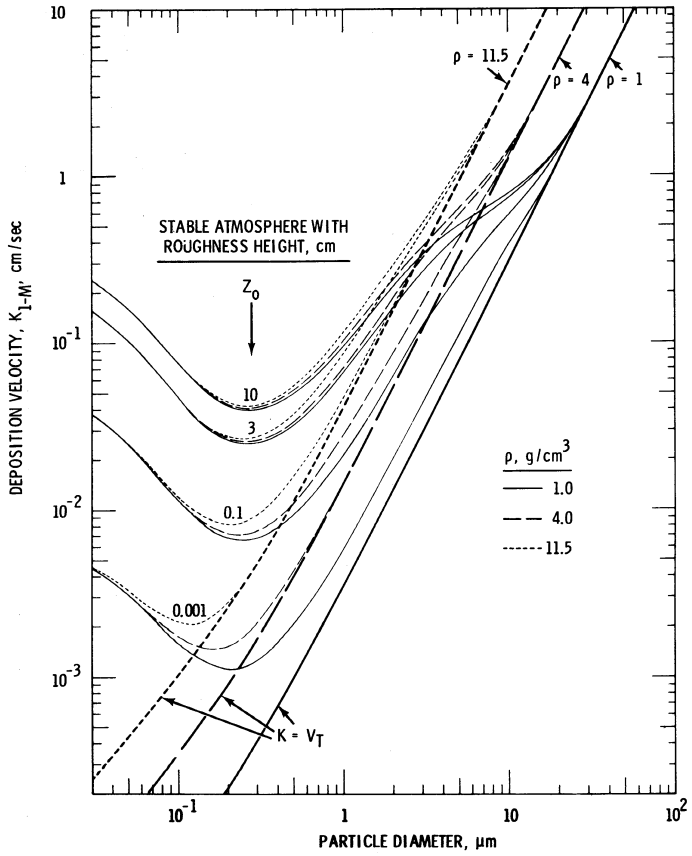


Figure 2.6: Calculated dry deposition velocities at 1 m for $u_* = 20$ cm s$^{-1}$. From [*Sehmel*, 1980].

10% to 20% of the physical surface roughness, and a snow surface may be represented by $z_0 = 0.1$ cm [*Sehmel*, 1980]. Further literature may be found at [*Nicholson*, 1988; *Wesely and Hicks*, 2000].

Both, wet and dry removal processes exhibit a minimal effectiveness in the size range around roughly 1 $\mu$m diameter. Therefore, it is not surprising to find the maximum of the mode of aeolian dust carried long distances in this size range. However, as the deposition mechanisms active in this size range are complicated and not very well understood further investigations are clearly needed. This is especially relevant for predictions of size shifts during deposition depending on variable micrometeorological conditions.

# Chapter 3

# Particle counting and sizing

In this chapter a novel laser sensor for microparticle measurements is presented. Its measurement principle and the size calibration are described. Further more, practical laboratory experiences are reported, and the parametrization of the particle size distribution with the lognormal distribution function is discussed. Information on the use and calibration of the laser sensor is also given in the methodical sections of chapters 4 and 5, and in appendix A.

## 3.1 Measuring techniques for microparticle analysis

There are various methods to measure the concentration and size distribution of microparticles in ice cores. Most of these methods use liquid samples; under certain circumstances some of the optical methods described below even work the ice directly. All methods are either based on single particle detection or on the assessment of the bulk particle content.

Filtration of a liquid sample with consequent microscopy or element analyses is a practiced method. But it is not applied regularly and does not reach a high depth resolution. Further, it only yields either a size distribution or the particle concentration but not both at the same time.

The Coulter Counter method is well established for ice core analyses (e.g. [*Petit et al.*, 1981; *Geis*, 1988; *Steffensen*, 1997]); here, single particle volumes are measured in liquid samples. The big advantage of this method is that the volume of the particle is measured independently from its shape. Size distribution and particle concentration are obtained simultaneously and the size range covered is approximately from 0.5 $\mu$m to

20 $\mu$m diameter, which is appropriate for the analysis of windblown mineral particles in remote regions. The disadvantages of the Coulter method are, however, that extensive sample preparation is required, that the measuring procedure is tedious and that the device is very delicate and susceptible to external disturbances.

Optical methods usually use the intensity of 90° scattered light to infer the particle concentration. This principle may be applied to individual liquid samples [*Hammer*, 1977] or using a flow-through setup [*Ram and Illing*, 1994]. It also works directly on bubble-free ice [*Ram and Koenig*, 1997]. Very recently, also the successful application of a borehole logger has been reported [*Bay et al.*, 2001]. All these applications may yield a particle concentration, but they do not yield a size distribution. Also, no calibrated high-resolution profiles have yet been published, which indicates calibration problems.

The advantage of these optical methods is the rapidity of the measurement. If the measurement is performed directly on ice only little sample preparation is necessary. For measurements on liquid samples a continuous flow setup can be used, which allows very efficient sample preparation via controlled longitudinal sample melting (see [*Röthlisberger et al.*, 2000] and appendix B, in German). Here, ice core aliquots of typically 1 m length are continuously melted in a controlled and contamination-free fashion and the work-intensive preparation of individual samples can be omitted. This method enables continuous measurements and a very high depth resolution.

In the work presented here a novel optical measuring technique has been used. It is based on the detection of transmitted rather than scattered light. Like the Coulter method it performs single particle detection and simultaneously yields particle concentration and size distribution. Therefore, the efficiency of optical counting may be used without lacking size information.

## 3.2 The laser sensor: measurement principle and operational parameters

The particle detector was developed by *Klotz GmbH*, Bad Liebenzell (Germany) for general purpose laboratory applications. For ice core analyses it was specifically modified in a close collaboration of *Klotz* and the *Institut für Umweltpysik* of the University of Heidelberg and its applicability was verified by *Saey* [1998] and *Armbruster* [2000]. Within the work presented here it was deployed for the first time during a field season.

The device works on a flow-through basis. The sample liquid is pumped through a very small measuring cell of quarz and stainless steel. There, it is illuminated perpendicularly to its flow direction by a laser beam with 670 nm wavelength. The measuring

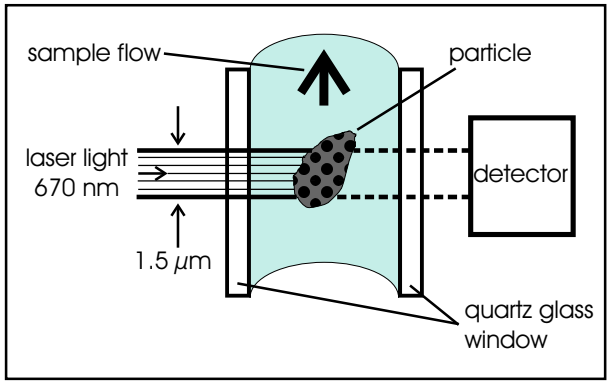


Figure 3.1: The detection cell of the laser particle detector.

cell has a cross section of 250 $\mu$m × 230 $\mu$m (perpendicular to flow direction). The laser beam is only 1.5 $\mu$m high but covers the detection cell across its full width. Thus, the surveyed volume is 250 $\mu$m × 230 $\mu$m × 1.5 $\mu$m (see Figure 3.1). The transmitted light is measured by a photo diode. When a microparticle passes through the laser beam the transmitted light is attenuated by geometric shadowing and scattering processes. This leads to a negative peak, which is detected and sorted by height into one of up to 32 channels. The channels may be adjusted freely within the size spectrum.

An internal storage can hold accumulated size distribution data, which later may be transferred to a computer for processing. Size distribution data may be accumulated over sample intervals manually controlled by the user or automatically controlled based on a specified time interval or accumulated counts. The device has an analog output which's voltage is proportional to the momentary count rate. This can be used for high resolution profiling. Essential to the detection method are the dimensions of the laser beam. The very narrow beam strongly enhances the sensitivity of detection by decreasing the steady background signal for the photo diode and reducing the problem of forward scattering.

Coincidence losses may occur at very high count rates due to dead time of the detector electronics after each count; this type of loss would influence the measured concentration but not the size distribution. Coincidence losses due to the simultaneous presence of more than one particle in the surveyed volume would lead to the registration of one large instead of two small particles and therefore alter the measured size distribution; however, coincidence losses of the second type occur very rarely and therefore the size distributions remain intact even if coincidence of the first type should occur.

To ensure a linear conversion of the measured concentration the analog output is

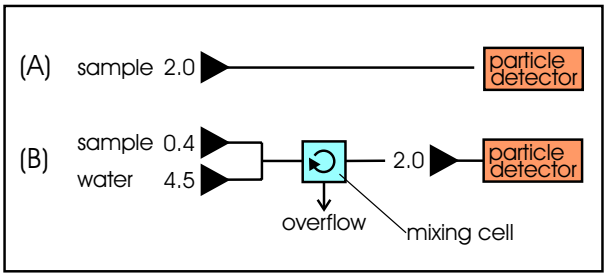


Figure 3.2: The dilution setup. Numbers denote flow rates in ml $min^{-1}$. Samples with moderate or low microparticle concentration could be measured directly (A). Samples with high concentrations were diluted with particle-free carrier water (B).

| Parameter | Value |
|---|---|
| min. particle diameter | 1.0 $\mu$m |
| optimal flow rate | 2 (1.3 - 4.0) ml $min^{-1}$ |
| max. count rate (analogue output) | 4000 $s^{-1}$ |
| background count rate | typ. 2 $s^{-1}$ |

Table 3.1: Parameters of the laser sensor. The range given for the optimal flow rate indicates an interval where operation was found appreciable. The maximal count rate is limited due to internal settings of the analog output only (see [*Saey*, 1998] for details).

limited to a maximum count rate of 4000 $s^{-1}$. To avoid data loss at high concentration therefore the count rate was reduced by reducing the sample flow rate. However, as low flow rates enhance sample dispersion in the flow system particle-free carrier water was added to the sample in a T-junction. After the two liquid streams were joined the sample was dispersed in a mixing cell of approximately 0.4 ml volume. The mixing improved the homogeneity of the sample at the detector and ensured that the overflow of the mixing cell would not fractionate between sample and carrier water. The dilution setup is sketched in Figure 3.2.

The sample liquid is not contaminated or altered through the measurement and may be further used for other applications (e.g. ion chromatography). The most important parameters of the laser sensor are given in Table 3.1.

## 3.3 The laser sensor: size calibration

The inter-relation of peak height and particle size is very complex, first because the microparticles are not spherical, and second because detection is based on complicated

optical processes. For large particles with a diameter $d \geq 5$ $\mu$m geometric shadowing is the most important process [*Saey*, 1998]; for smaller particles scattering processes become increasingly important (Mie-scattering). For both processes peak height does not only depend on particle volume but also on its geometrical shape, its material (optical density), and on the orientation which the particle randomly has when it passes the laser beam. Considering such a complexity the analytical calculation of the characteristic curve linking peak height with particle size seems hopeless. A good calibration, however, could empirically be achieved via the comparison with Coulter Counter measurements.

For the calibration, several sections of the NGRIP ice core were measured simultaneously with the lasers sensor and a Coulter Counter. Subsequently the laser sensor data was shifted on the size axis to fit the Coulter Counter data. This is legitimate because the counting efficiencies of the two counters have been shown to be equal [*Saey*, 1998]. In praxis, the size adjustment was done starting at the upper end of the size spectrum, where the calibration of the laser sensor can independently be achieved through measurements of monodispersed latex spheres of known diameter. Also, the emergence of particle count rates from zero when going from larger to smaller particles can be recognized clearly in both data sets and provides a linkage for the two distributions. Figure 1 on page 69 shows a set of size spectra that were used for the calibration of the NGRIP data. For details see also the description of the calibration in chapter 5 on page 48.

It was noticed, however, that the flow setup may influence the size distribution to an extent not negligible. This effect was especially strong when the dilution setup was in use. Individual calibrations were therefore needed to compensate for the changes of the respective flow setup used. Listings of the calibrations and respective technical details are given in appendix A.

Assessing the accuracy of the calibrations is difficult because there are not many Coulter Counter measurements available for a comparison. However, the modes of lognormal fits of the Coulter Counter or of the laser sensor data differ by typically 0.1 $\mu$m as can be seen from Figure 1 on page 69. Since this difference is probably largely due to non-identical sample populations (for explanation see there) it may be inferred that the error of the calibration itself is likely less than 0.1 $\mu$m. Double measurements of several samples – one time performed with and one time without the dilution setup – agreed also within 0.1 $\mu$m tolerance.

In future applications the laser sensor should again be calibrated via Coulter Counter measurements together with the flow setup used to compensate for the influence of the flow setup. Systematic investigations of the size and the stability of the influence of

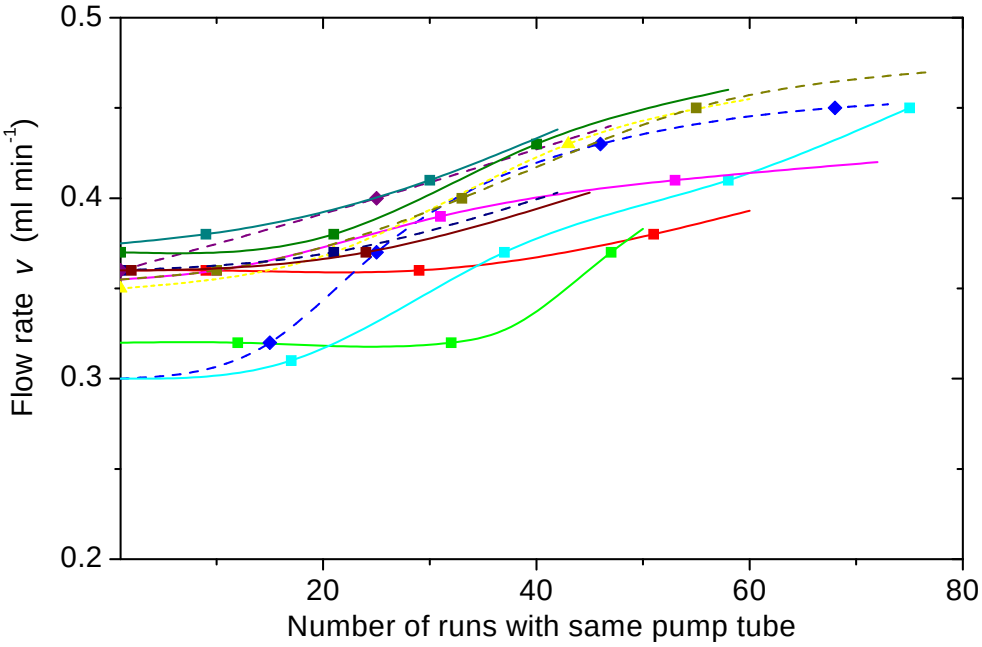


Figure 3.3: Change of the flow rate during the lifetime of a pump tube of the NGRIP measurements. Symbols represent flow rate checks. Lines show spline interpolations. The duration of one particle measurement run is approximately one hour.

the flow setup are desirable to enhance the reliability of the calibrations.

## 3.4 Determination of flow rates

To calculate the particle number concentration $C_N$ not only the total number of counts $N$ but also the associated volume $V$ of sample liquid needs to be measured. During high resolution profiling the momentary count rate $n$ is recorded and needs to be divided by the flow rate $v$, as $C_N = N/V = n/v$. Therefore, to infer the particle concentration the flow rate must also be accurately known.

Peristaltic pumps and Tygon pump tubes were used to feed the sample through the particle detector. (See Figure B.3 on page 111 for an example of a flow setup.) These pumps are easy to maintain and cause only little sample dispersion. On the other hand, the flow rates are not constant as the pump tubes deteriorate with regular wear and tear. Therefore, in the course of the measurements during the NGRIP 2000 field campaign all flow rates relevant to the particle measurement were checked daily. Figure 3.3 illustrates the change of flow rates of various pump tubes. It can be noticed that during the use of a pump tube over several days its flow rate increases by typically

15% and in extreme cases by up to 50%. The difference between two flow rate checks on consecutive days, which spanned usually 15 to 20 particle measurement runs, is typically 5% to 10%.

To assign a flow rate to each particle measurement run the measured flow rates were non-linearly interpolated. The interpolation was based on cubic splines, but it was ensured that no additional local maxima or minima were produced. However, the flow rate was not always measured right after and right before the exchange of a pump tube; in these cases the flow rate data needed to be extrapolated beyond the first and last point of measurement. Hereby it was aimed for an usual development so that the resulting curve fitted well into the existing group. The error of the pump rate assigned to each run after the interpolation performed is estimated to 5%.

In future applications the flow rates should be checked more frequently and especially right before and right after a pump tube is exchanged. An even better improvement would be the use of a calibrated continuously working flow meter because sometimes conventional flow rate measurements are not feasible even if needed, e.g. if a pump tube unexpectedly breaks down.

## 3.5 Parameterization of the size spectrum

The lognormal distribution is broadly used for the description of size distribution in aerosol sciences [*Davies*, 1974; *Patterson and Gillette*, 1977] and was also adopted to parameterize microparticle size distributions in ice cores, e.g. [*Royer et al.*, 1983; *De Angelis et al.*, 1984; *Wagenbach and Geis*, 1989; *Steffensen*, 1997]. Other approaches such as the empirical law by Junge [*Junge*, 1963] are not used much any more in this field. In a new investigation *Delmonte et al.* [2002] found that size spectra with a very high size resolution are slightly better described with the 4-parameter Weibull than with the 3-parameter lognormal distribution. But the mathematical properties and the physical interpretability of its parameters are strong advantages of the lognormal function. And as the data considered here has only a low size resolution the lognormal distribution can be used without drawbacks.

**Mathematics of the lognormal distribution** In the following the notation of [*Herdan and Smith*, 1953] is adopted. Further information can be found in [*Cadle*, 1955] or [*Aitchison and Brown*, 1957].

The probability density $p(x)$ is called *lognormal* if $q(z)$ is a normal distribution and

$p(x) = q(z)$ for $z = \ln x$, i.e.

$$p(x) = A\frac{1}{\sqrt{2\pi}\ln\sigma}e^{-\frac{1}{2}\left(\frac{\ln x - \ln\mu}{\ln\sigma}\right)^2}$$

with:
$A$: the total integral of the distribution;
$\mu$: the geometric mean of the distribution (here identical with the median), as $\ln\mu = \overline{\ln x_i} = \frac{1}{N}\sum \ln x_i = \ln\left(\prod x_i\right)^{\frac{1}{N}}$; and
$\sigma$: geometrical standard deviation of the distribution, i.e. the standard deviation of ratios about $\mu$, as $\ln\sigma = \sqrt{\frac{1}{N}\sum\left(\ln x_i - \overline{\ln x_i}\right)^2} = \sqrt{\frac{1}{N}\sum\left(\ln\frac{x_i}{\mu}\right)^2}$.

The probability $P$ to find a value $z_0$ within an interval $[a, b]$ is given by $P\left(z_0 \in [a,b]\right) = \int_a^b q(z)dz = \int_{\ln a}^{\ln b} p(x)d\ln x$. When going from a continuous to a discrete distribution with bins $i$ the probability $P_i$ to find a value in the $i$-th bin is $P_i = p(x_i)\left(\Delta\ln x\right)_i$ where $x_i$ is a suitably chosen value in the $i$-th bin and $\left(\Delta\ln x\right)_i$ is the width of this bin on a logarithmic scale. If all bins are equidistantly spaced on a logarithmic scale then all factors $\left(\Delta\ln x\right)_i$ are equal and it is $P_i \propto p(x_i)$. This means in particular that with a logarithmically-equidistant spacing of bins the most probable value – the so-called *mode* $m$, which is the maximum of $P(x)$ – falls together with the maximum (identical with the geometric mean) $\mu$ of the density distribution $p(x)$. This situation is illustrated in Figure 3.4-B.

However, if the bin spacings are equidistant on a linear scale then all factors $(\Delta x)_i$ are equal and using $\left(\Delta\ln x\right)_i = \frac{(\Delta x)_i}{x}$ it is found that $P_i \propto \frac{1}{x_i}p(x_i)$. In this case the mode $m$, i.e. the most probable value, is not identical with $\mu$ but instead $m = \mu e^{-(\ln\sigma)^2}$. Also the arithmetic mean $\overline{x}$ is different from $m$; it is given by $\overline{x} = \mu e^{+\frac{1}{2}(\ln\sigma)^2}$. This is illustrated in Figure 3.4-A.

Figure 3.4 illustrates the differences between linear (A) and logarithmic (B) bin- (or axis-) spacing. The linear spacing has the advantage that it is area-conservative, i.e. equal areas represent equal probabilities; but the mathematical properties of the linearly spaced distribution are somewhat obscure. The logarithmic spacing on the other hand has the advantages that the full size range may be covered adequately and above all that the mathematical description is easier to grasp because the mode (most probable value), the geometric mean (maximum of the density distribution), and the arithmetic mean all are identical. In the following we will therefore always consider logarithmic densities $\frac{dN}{d\ln d}$ for the size distribution by counts or $\frac{dV}{d\ln d}$ for the size distribution by volume, and $\mu$ will be referred to as the mode. The size distributions shown in chapter 5 in addition are plotted on a logarithmic y-axis to better reproduce the great dynamic range of the distributions; in such log-log-scaling the shape of the

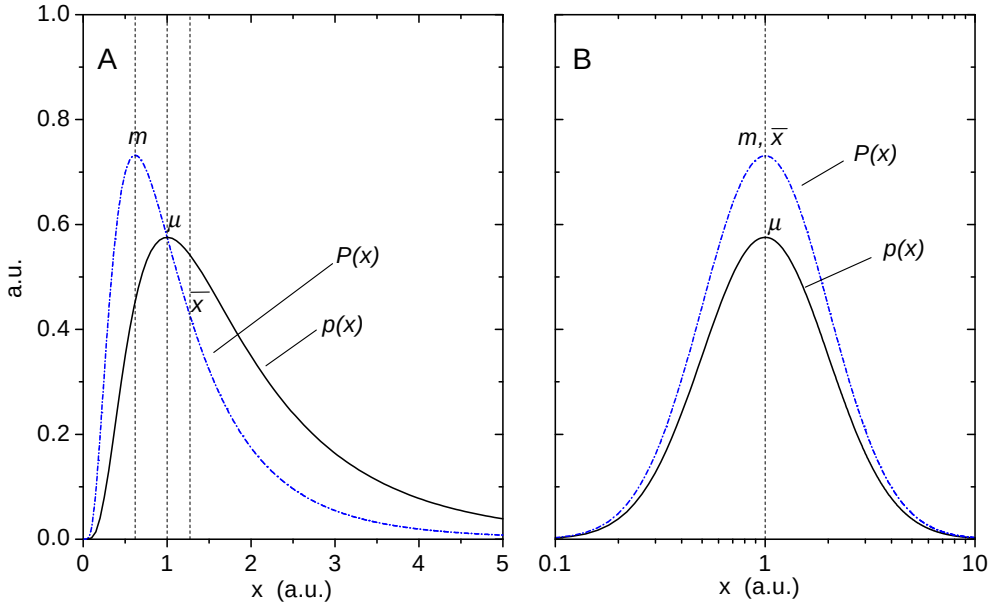


Figure 3.4: The lognormal distribution with linear (A) and logarithmic (B) bin- or axis-spacings. Shown is for both cases the probability density $p(x)$ and the probability $P(x)$ for bins equidistant on the respective axis. Indicated are the most probable value $m$ (the mode, which is the maximum of $P(x)$), the geometric mean $\mu$ (= median), which is the maximum of $p(x)$, and the arithmetic mean $\overline{x}$.

lognormal distribution is parabolical.

The mathematical advantages of the lognormal distribution particularly lie in the properties of its moment-functions. The $l$-th moment of a probability distribution $q(z)$ is the expectation of $z^l$, i.e. $\int z^l p(z)dz$. With the lognormal distribution the lognormal character is preserved when going from the distribution from one moment to that of another. In doing so, the parameters transform as follows:

$$\ln\mu \mapsto \ln\mu' = \ln\mu + l(\ln\sigma)^2, \quad \text{i.e.} \quad \mu' = \mu e^{l(\ln\sigma)^2}, \quad \text{and}$$

$$\ln\sigma \mapsto \ln\sigma' = \ln\sigma \quad \text{i.e.} \quad \sigma' = \sigma.$$

The meaning of the most important moments are listed in table 3.2 together with their transformation properties. The transformation are of practical relevance e.g. for the transition from a size distribution by number to one by volume, or reverse. First it is remarkable that the distributions by number and by volume may both be lognormal at the same time. Further, the transformation properties are most simple: Given for example the size distribution of particle *volumes* with mode $\mu_V$ and standard deviation $\sigma_V$ then the parameters $\mu_N$ and $\sigma_N$ of the size distribution of particle *numbers* are

| $l$-th Moment | Significance | $\ln \mu' = \ldots$ |
|---|---|---|
| 0 | $d^0$ : number | $\ln \mu$ |
| 1 | $d^1$ : length | $\ln \mu + 1(\ln \sigma)^2$ |
| 2 | $d^2$ : surface | $\ln \mu + 2(\ln \sigma)^2$ |
| 3 | $d^3$ : volume | $\ln \mu + 3(\ln \sigma)^2$ |

Table 3.2: Moments of the lognormal distribution and their significance.

obtained through the transformation from the 3rd to the 0th moment:

$$\ln \mu_N = \ln \mu_V - 3(\ln \sigma)^2, \quad \text{and}$$

$$\sigma_N = \sigma_V.$$

The reverse transition from the distribution by number to the distribution by volume is obtained correspondingly through the transformation from the 0th to the 3rd moment. The distribution by surface area may be inferred likewise (see Table 3.2).

**Practical application** The size distribution that can be obtained from the laser sensor is in the format of a number distribution. Thereby the size range covered by the detector lies in the upper flank of the number distribution of microparticles and does not include the maximum (the mode). The lack of the maximum in the distribution data leads to higher uncertainties in curve fitting to determine the parameters of the distribution. However, the covered size range includes the maximum of the volume distribution; this provides more rigid boundary conditions for the curve fit and improves the accuracy of the determined parameters. Therefore, the curve fit is performed after the distribution by numbers is transformed to a distribution by volume.

For the transformation of the measured data to a distribution by volume the accumulated counts in each bin are converted to an accumulated volume. To do so a characteristic mean single particle volume $v_i = \frac{4\pi}{3}\left(\frac{\overline{d}_i}{2}\right)^2$ is assigned to each bin; in a first approximation the characteristic diameter of each bin is taken as $\overline{d}_i = \sqrt{d_i^+ d_i^-}$ where $d_i^+$ and $d_i^-$ are the upper and lower bin boundary, respectively. In the data considered in this work the bins are chosen rather wide ($d^+/d^- \approx 1.3$); therefore, the size distribution of the data *within* each bin is accounted for by successive refinements in the choice of $\overline{d}_i$. For that purpose $\overline{d}_i$ is calculated for each bin in a "next order approximation" from the optimized fit function; then the transformation of the measured data to a volume distribution and the curve fitting are redone using the new values for $\overline{d}_i$. This procedure is repeated until no significant corrections of the fit parameters are

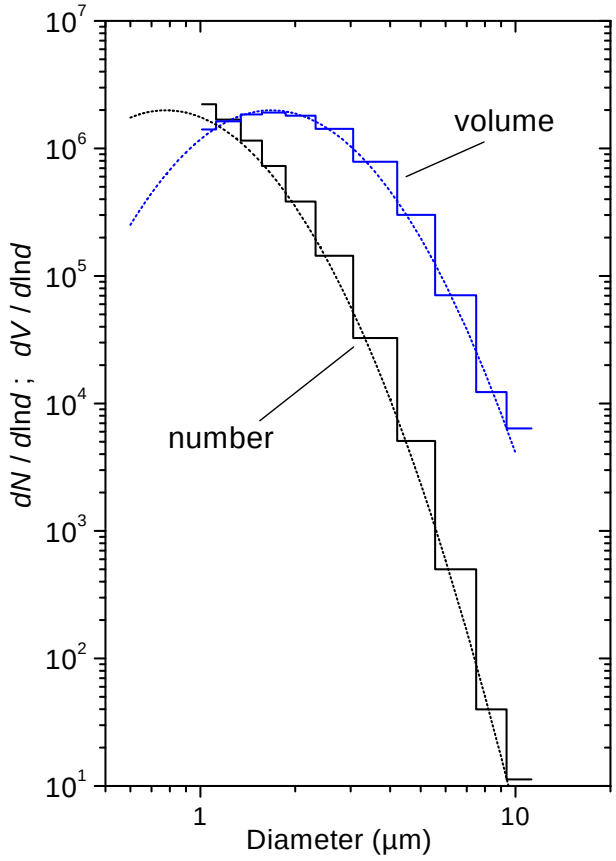


Figure 3.5: Size distribution by number and by volume. The fit is performed on the volume distribution as it provides more rigid boundary conditions. The mode $\mu_V$ was found at 1.68 $\mu$m which corresponds to $\mu_N = 0.87$ $\mu$m (with $\sigma = 1.66$). The data shown is that of a NGRIP sample from the LGM period.

observed (usually after two iterations). The corrections of $\overline{d}_i$ yields small improvements to the fit parameters.

The curve fitting is done via parameter optimization using a MATLAB-script based on the Nelder-Mead algorithm. As a measure for the error the relative quadratic error sum between measurement data $y_i$ and model data $z_i$ is taken in the form of $\sum(\ln y_i - \ln z_i)^2$. This yields better results than considering the absolute errors because the distribution data covers several orders of magnitude in some size spectra, and otherwise the fit would be dominated by a few points close to the maximum.

Figure 3.5 gives an example of the size distribution of a NGRIP sample by number and by volume. The optimized fit curve is included for both forms of the distribution. It was obtained as described above from the distribution by volume and subsequently transformed to the distribution by number. The data range considered for the curve

fit is from 1.0 $\mu$m to 7.5 $\mu$m.

# Chapter 4

# High resolution microparticle profiles at NGRIP: Case studies of the calcium – dust relationship

Urs Ruth, Dietmar Wagenbach, Matthias Bigler, Jørgen P. Steffensen, Regine Röthlisberger, and Heinz Miller

*Annals of Glaciology*, Volume 35 (2002), in press

# High resolution microparticle profiles at NGRIP: case studies of the calcium - dust relationship

Urs Ruth[1,2], Dietmar Wagenbach[1], Matthias Bigler[3], Jørgen P. Steffensen[4], Regine Röthlisberger[3], and Heinz Miller[2]

[1]Institut für Umweltphysik, University of Heidelberg, Germany

[2]Alfred Wegener Institut für Polar- und Meeresforschung, Bremerhaven, Germany

[3]Climate and Environmental Physics, University of Bern, Switzerland

[4]Department of Geophysics, University of Copenhagen, Denmark

Annals of Glaciology, Volume 35 (2002), in press

## ABSTRACT

A novel flow-through microparticle detector was deployed concurrently with continuous flow analyses of major ions during the NGRIP 2000 field season. The easy handling detector performs continuous counting and sizing. In this deployment the lower size detection limit was conservatively set to 1.0 µm equivalent spherical particle diameter, and a depth resolution of ≤ 1 cm was achieved for microparticle concentrations. The dust concentration usually followed the $Ca^{2+}$ variability. Here results are presented from an inspection of the Ca/dust mass ratio in 23 selected intervals, 1.65m long each, covering different climatic periods including Holocene and last glacial maximum (LGM). A ($Ca^{2+}$)/(insoluble dust) mass ratio of 0.29 was found for Holocene and 0.11 for LGM. Changes of the Ca/dust ratio also occur on an annual to multi-annual time scale exhibiting the same pattern, i.e. a lower Ca/dust ratio for higher crustal concentrations. Moreover, the $Ca^{2+}$/dust ratio may increase significantly during episodic events such as volcanic horizons due to enhanced dissolution of $CaCO_3$. This questions the notion of deploying Ca2+ as a quantitative mineral dust reference species and stresses the importance of variable source properties or fractionating processes during transport and deposition.

## INTRODUCTION

The atmospheric mineral dust load, mainly composed of insoluble mineral particles, is an important part of Earth's climatic system as it is involved in direct and indirect radiative forcing processes (e.g. Tegen and Fung, 1994). Equally, the amount, size distribution and composition of dust deposited on polar ice sheets may hold valuable information about both, positions and climatic conditions of source areas, as well as about long range transport and deposition processes (Biscaye and others, 1997; Fuhrer and others, 1999). Over the last climatic cycle, Greenland as well as Antarctic mineral dust records exhibit changes on a huge dynamic range (e.g. Hansson, 1994; Steffensen, 1997; Petit and others, 1999). In Greenland these changes occurred very rapidly and were coinciding with changes in $\delta^{18}O$ at rapid climatic transitions within the last Pleistocene as has been inferred from high resolution measurements of $Ca^{2+}$ and ECM on the GRIP and GISP2 ice cores (Taylor and others, 1997; Fuhrer and others, 1999).

The concentration of Ca ions ($Ca^{2+}$) is often being used as a proxy parameter for total mineral dust in ice cores as it represents the major part of the readily dissolved fraction of the dust aerosol. But the soluble proportion of dust is not constant over different climatic periods (Steffensen, 1997), so using $Ca^{2+}$ as a proxy may give a distorted view of the total dust concentration. However, also dust measurement techniques have specific disadvantages. Only low resolution profiles or selected continuous sections have been measured for insoluble microparticles using the well established Coulter counting technique (e.g. Steffensen, 1997) because it requires extensive sample preparation and handling. And high resolution continuous dust measurements using 90° laser light scattering off melt water (Hammer and others, 1985) or off ice (Ram and Koenig, 1997) yield no size distribution information or are difficult to calibrate.

Here we introduce a novel laser sensor device for microparticle measurements deployed for continuous recordings of microparticle concentration and size distribution during the North Greenland Ice Core Project (NGRIP) 2000 field season. Apart from the methodical aspects, we present and discuss case studies of the dust concentration focussing on the $Ca^{2+}$/dust ratio under inconspicuous conditions as well as in volcanic horizons.

## EXPERIMENTAL SETUP

During the NGRIP 2000 field season, extensive scientific processing was performed shortly after retrieval of the ice core. This included the operation of a warm laboratory for continuous flow analyses (CFA) of $Ca^{2+}$, $Na^{+}$, $NH_4^{+}$, $SO_4^{2-}$, $NO_3^{-}$, $H_2O_2$ and HCHO concentrations, and of electrolytical conductivity (Röthlisberger and others,

2000). Concurrently, continuous microparticle counting and sizing was performed. Discrete liquid samples were collected at 55 cm resolution for subsequent ion chromatography (IC) analysis; and over selected depths, discrete samples for IC and acidity measurements at approx. 6 cm resolution were also collected by an automatic sampler. The contamination free sample water for all these analyses was drawn from the inner area of a melt head, where the ice was melted at approx. 4 cm $min^{-1}$. For an overview of the setup see Figure 1. By these means the core was continuously analyzed from approx. 1400 m to 2930 m depth.

**The particle sensor**

The particle sensor, for general purpose laboratory applications, is from Klotz GmbH, Bad Liebenzell, Germany, and was specifically modified in collaboration with the Institut for Environmental Physics of the University of Heidelberg (Saey, 1998; Armbruster, 2000). The sample water is pumped through the detection cell, where it is illuminated by a 1.5 µm by 250 µm wide laser light beam of 670 nm wavelength. The transmitted light is measured by a photo diode detector (see Figure 2). When a particle passes through the detection area the transmitted light is attenuated by shadowing and scattering which results in a negative peak of transmitted light. The peak is counted and sorted by height into 32 bins, that can be adjusted to appropriate size intervalls.

The inter-relation of peak height and particle size is complex. Geometric shadowing is combined with scattering processes, both depending not only on particle volume but also on particle shape, material and orientation. A size calibration was achieved by measuring NGRIP ice core samples from different climatic periods with a Coulter counter and tying the laser sensor measurements of identical depths to the Coulter counter spectra. The calibration measurements showed the particle detection limit to be approx. 0.8 µm of spherical equivalent particle diameter. For our measurements, we used 1.0 µm diameter as the lower detection limit to be safely above the level of detector noise.

In our measuring procedure, size distributions were averaged over 1.65 m intervals. Respective results including size calibration will be presented elsewhere (Ruth, in preparation). The bulk particle number concentration was obtained continuously. To do so, the momentary count rate, converted to an analogue output signal, was recorded and the flow rate regularly measured. The continuously recorded data was later reduced to 1 mm depth intervals. Dust mass concentrations were inferred by integrating the particle size distributions that were obtained for each 1.65 m section and a material density of 2.7 g $cm^{-3}$; on average, this yielded that 1000 count $ml^{-1}$ are equivalent to 5.6 µg $kg^{-1}$. For each section, the relative error of particle mass is about 15% due to size calibration uncertainties and varying pump rates.

To avoid coincidence distortion of the measurements the output signal is cut off by the counter electronics if the counting rate exceeds 4000 particles $s^{-1}$, so the sample flow needs to be decreased for high particle concentrations. However, as flow rates below 1 ml $min^{-1}$ increase the sample dispersion in the flow system, the sample water from glacial age ice, which has a considerably higher dust concentration, was diluted with 0.2 µm prefiltered carrier water. Hereby an effective sample flow of approx. 0.15 ml $min^{-1}$ could be established while keeping the flow through the sensor above 2 ml $min^{-1}$. The dilution setup allowed for measuring concentrations lower than 15 µg $kg^{-1}$ and in excess of 15,000 µg $kg^{-1}$, thus, covering the full dynamic range from Holocene to last glacial maximum (LGM). When used without the dilution system, the detection limit in terms of minimal count rate was about 200 particles $ml^{-1}$; this value however is dependent on the flow rate.

As used in our setup, the depth resolution of the microparticle measurement – expressed as the observed 1/e-depth of a step signal – is ≤ 1 cm. It is generally similar to the depth resolution of most other CFA-components, often slightly better. Apart from the melt rate, the depth resolution is limited by the conical surface of the melt head, by dead volumes and by longitudinal sample dispersion in the flow system. The impairment in depth resolution from using the dilution system was around 10%. In ice with low particle concentration, the counting statistics also impose a limit on the depth resolution by raising the error of a data point if the number of counts for this data point is low, thus, demanding an increase of interval width for each data point. However, the contribution of this statistical effect is more than one order of magnitude less than that of the mentioned physical factors.

Microparticle concentrations are reported here for the size fraction from 1.0 µm to 11.5 µm equivalent spherical diameter in µg $kg^{-1}$. The mass fraction not measured below 1.0 µm accounts for about 10% assuming a typical lognormal volume distribution.

**List of samples**

From the whole NGRIP core profile 23 sections, each 1.65 m long, are taken for this study. These sections cover depths from 1420 m to 2921 m and represent various climatic periods including Holocene and LGM. For all sections $\delta^{18}O$ data are already available (personal communication from NGRIP members, 2000). For some sections acidity and standard IC anion data is also available and will be included in our discussion. Table 1 gives an overview of all selected sections, many of which contain volcanic horizons.

## RESULTS AND DISCUSSION

### A: The high resolution profiles

Articulate variations of the dust concentration are observed throughout large sections of the core. Figure 3 shows two 1.65 m long sections of the microparticle and $Ca^{2+}$ profiles, one out of the Holocene and one out of the LGM. Typical peak heights for microparticles are about 6 times ($Ca^{2+}$: 4 times) the background value in the Holocene and about 2.2 times ($Ca^{2+}$: 2.0 times) in the LGM section. Based on a preliminary estimate of annual layer thicknesses $\lambda$, which was done by applying the GRIP ages from Johnson and others (1997) to identified horizons in the NGRIP core, we expect that the variations may correspond to annual variations in the Holocene section; in the LGM section partly annual and partly multi-annual variations may be resolved. The insoluble dust profile, therefore, may assist the dating by annual layer counting based on other high resolution profiles, such as ECM, $Ca^{2+}$, $Na^{+}$, or visual stratigraphy (e.g. Meese and others, 1997).

### B: Variation of the $Ca^{2+}$-to-dust ratio

Normally, a good correspondence is observed between insoluble microparticle and $Ca^{2+}$ concentrations for Holocene ice as well as for glacial age ice. The correlation coefficients for the two examples shown in Figure 3 are 0.92 (Holocene) and 0.89 (LGM) after slight smoothing of both signals (see below). A similarly high correlation is found throughout the whole core. This at first sight may be seen as a general confirmation for the use of $Ca^{2+}$ concentrations as a proxy for the insoluble mineral dust variability.

A more detailed examination of the $Ca^{2+}$/dust ratio reveals, however, distinct differences between the Holocene and the glacial section. To inspect these, the $Ca^{2+}$/dust ratio was calculated for each data point and smoothed to weaken artifacts arising from incorrect peak phasings and from different peak shapes caused by signal noise, different sample dispersion or different response characteristics of the two detection systems. For the smoothing a 5.0 cm wide hanning window was used, i.e. a gliding average using a cosinusoidal weighting function. The smoothed $Ca^{2+}$/dust ratio is included in Figure 3. It varies significantly on the same depth scale as peaks occur in the crustal concentrations and tends to be enhanced during low dust levels. The (mean $Ca^{2+}$) / (mean dust) ratio of the two sections are ~ 0.29 for Holocene and ~ 0.11 for LGM, which is similar to earlier findings from Steffensen (1997) based on established Coulter counter and standard IC measurements.

For all ice core sections listed in Table 1 the $Ca^{2+}$/dust mean ratios were calculated; hereby horizons with strong acid inputs, that showed unusually high $Ca^{2+}$/dust values (see below), were excluded. Figure. 4 shows the such derived (mean $Ca^{2+}$) / (mean dust) ratios plotted against $\delta^{18}O$; mean microparticle concentrations are also shown. A gradual trend to lower mean ratios for isotopically colder samples is exhibited. It can be excluded that the observed trend is an artifact arising from possibly higher relative errors of the measurements for isotopically warmer samples, which have lower concentrations of $Ca^{2+}$ and dust; even Holocene concentrations are well above detection limit, and both systems responded very linearly to sample concentrations. Also the $Ca^{2+}$ fraction derived from sea salt aerosol does not contribute significantly.

In order to compare the measured $R_0$ = ($Ca^{2+}$)/(insoluble dust) ratios with data on the elemental composition of airborne mineral dust or source material, the ratios $R_0$ need to be converted to $R$ = (total Ca) / (total dust). It is: $R = a\frac{1}{(bR_0)^{-1} + c}$, where $a$ = (total Ca) / ($Ca^{2+}$) $\approx 1$ is the ratio of total Ca to dissolved $Ca^{2+}$, $b \approx 0.9$ is the correction for the dust fraction not measured below 1.0 µm, and $c = 2.5$ is the mass ratio of $CaCO_3$ to Ca, assuming that the dissolved dust fraction predominantly consisted of $CaCO_3$ or of species with similar mass. This approximation yields ratios of 0.16 for Holocene and 0.08 for LGM. This Holocene value is in weak agreement with a mean ratio of 0.09 (range: 0.06 – 0.18) deduced from measurements of total Ca and Al in recent Greenland firn by atomic absorption spectroscopy (Boutron, 1978), but it is larger than the value of 0.05 deduced from total Ca and Al analyses in Summit aerosol by Colin and others (1997). For comparison to both references, the reported Al masses were used to infer the total dust mass by assuming a crustal abundance of 8%.

The trend to lower observed values of $Ca^{2+}$/dust for lower $\delta^{18}O$ remains under dispute as several explanations may be invoked. These include possible changes of source areas and properties, or of fractionating transformation and removal processes during long range transport or deposition (e.g. Hansson, 1994; Wurzler and others, 2000). The observed effect may also possibly be explained by slower dissolution of $Ca^{2+}$ due to alkaline conditions of glacial ice, which would lead to lower observed $Ca^{2+}$ concentrations by the immediate CFA-detection method used here.

Changes of mineral dust source areas are a controversial topic in the literature. De Angelis and others (1997) – by comparing their $Ca^{2+}/Mg^{2+}$ ratios to Bowen (1979) – deduce mean sediment sources for present day and marine carbonate sources for the last glacial. Biscaye and others (1997) – based on mineralogical and isotopic studies – propose no significant change of source area during times of variable dust fluxes within the last glacial. Hinkley and others (1997) – on the basis of mineralogical studies – presume a present day tropospheric background aerosol uniformly composed of average

crustal rock and not of carbonates. Maggi (1997) finds that weathering processes may have been changed with climate; but little is known about how this might have affected the relative abundances of $CaCO_3$ or $CaSO_4$ in the dust aerosol (Pye, 1987). A comparison of our data with Ca abundances in crustal material (Bowen, 1979) (see Table 2) suggests that marine carbonates or limestone sediments could have contributed significantly only during Holocene and that that during LGM mean crust and other sediments would have dominated. Various soils could have contributed at all times.

In the data presented here, it may be noteworthy that the variations of the $Ca^{2+}$/dust ratio that occur on an annual to multi-annual scale follow the same pattern as the variations just discussed on a long time scale. As can be seen in Figure 3 the $Ca^{2+}$/dust ratio is small during large dust concentrations, which at least for the Holocene may be driven by variability in the transport efficiency as known for the Arctic Haze phenomenon (Rahn and Borys, 1977). It seems possible that also on an annual time scale these variations may be attributed to changing source areas or may be closely linked to changing fractionation processes during long range transport.

**C: Special events in the microparticle and $Ca^{2+}$ profiles**

Figure 5 shows an example of a 1.65 m long section from the time between GRIP interstadials 1 and 2 which exhibits several anomalies (denoted by $\alpha - \delta$). Event $\alpha$ is a strong dust layer (note that the microparticle concentration got cut off by the detector electronics). Event $\delta$ is an increase of the $Ca^{2+}$/dust ratio caused by a $Ca^{2+}$ peak that has no corresponding microparticle peak; only $NO_3^-$ exhibits a pronounced peak that may be related (e.g. Wolff, 1984). Events $\beta$ and $\gamma$ arise from two very strong $Ca^{2+}$ peaks coinciding with only small insoluble dust peaks; they have a $Ca^{2+}$/dust ratio about 100% and 200% higher than the typical value. Coinciding are very strong peaks in $SO_4^{2-}$ and also enhancements of ECM, acidity, and $F^-$ (not shown) indicating volcanic horizons. These phenomena were observed during cold glacial times predominately, but they also occured during warm interstadials.

From our size distribution measurements we can rule out that the observed increase of the $Ca^{2+}$/dust ratio during events $\beta$ and $\gamma$ is only an artifact resulting from a dust size distribution severely shifted towards larger particles during these events. High inputs of acid however may lead to enhanced $Ca^{2+}$/dust ratios by promoting the rapid dissolution of calcite particles or $CaCO_3$ coatings. Indeed, all 13 anomalous $Ca^{2+}$/dust enhancements investigated in this study are accompanied by a clear $SO_4^{2-}$ peak, indicating a strong input of acid (see Table 1).

An ionic balance was evaluated using major ion concentrations and acidity data for 10 of these sections, and it was found to be rather constant – not zero, at a low μeq

$kg^{-1}$ level – across the disturbed horizons, which indicates that no unmeasured ionic species contributed substantially during these events. From the ionic balance, of course, it still cannot be distinguished to which extent $SO_4^{2-}$ derived from $H_2SO_4$ or from mineral $CaSO_4$. But it seems much more probable that during volcanic events the predominant part of $SO_4^{2-}$ originates from volcanic $H_2SO_4$ and that the $Ca^{2+}$ peak is produced by enhanced dissolution of $CaCO_3$ during in-cloud processing or pre-analytical sample melting.

## CONCLUSIONS

The novel particle sensor proved to be a reliable tool even under field conditions; it provided the total particle concentration at ≤ 1 cm depth resolution backed up by size distribution information. Thus, calibrated records of insoluble particle mass concentrations are obtained. Variations of the Ca/dust mass ratio were seen during long term climatic changes as well as on annual or multiannual time scales. This suggests variable source properties or variable fractionation during transfer, which should be investigated in more detail. If $Ca^{2+}$ measurements are used as a quantitative proxy for mineral dust care must be taken when considering data across climatic transitions, at volcanic horizons, or at subseasonal resolution.

A dedicated investigation of Ca ion solubility in glacial meltwater and its implications for the CFA and IC analytical methods is essential as we are currently limited in our interpretation by this uncertainty. To elucidate possible variations in dust source areas and properties, or of changes in fractionation processes during long range transport, routine analysis of crustal reference elements like Al are needed as they would help to infer the total – i.e. soluble and insoluble – crustal concentration.

## ACKNOWLEDGEMENTS

The North-GRIP project is directed and organised by the Department of Geophysics at the Niels Bohr Institute for Astronomy, Physics and Geophysics, University of Copenhagen. It is being supported by funding agencies in Denmark (SNF), Belgium (NFSR), France (IFRTP and INSU/CNRS), Germany (AWI), Iceland (RannIs), Japan (MECS), Sweden (SPRS), Switzerland (SNF) and the United States of America (NSF). We wish to thank all the funding bodies and field participants. Chris Zdanowicz is thanked for his helpful comments to improve the manuscript.

## REFERENCES

Armbruster, M., 2000, *Stratigraphical dating of high alpine ice cores over the last 1000 years (in German)*, M.Sc. thesis, Institut für Umweltphysik, University of Heidelberg, Heidelberg.

Biscaye, P. E., F. E. Grousset, M. Revel, S. Van der Gaast, G. A. Zielinski, A. Vaars, and G. Kukla, 1997, Asian provencance of glacial dust (stage 2) in the Greenland Ice Sheet Project 2 Ice Core, Summit, Greenland, *Journal of Geophysical Research*, 102 (C12), 26765-26781.

Boutron, C., 1978, *Influences of aerosols of natural and antropogenic origin on the chemistry of polar snows (in French)*, Ph.D thesis, , University of Grenoble, Grenoble.

Bowen, H. J. M., 1979, *Environmental Chemistry of the Elements*, Academic Press, London.

Colin, J. L., B. Lim, E. Herms, F. Genet, E. Drab, J. L. Jaffrezo, and C. I. Davidson, 1997, Air-to-snow mineral transfer - crustal elements in aerosols, fresh snow and snowpits on the Greenland ice sheet, *Atmospheric Environment*, 31 (20), 3395-3406.

De Angelis, M., J. P. Steffensen, M. Legrand, H. Clausen, and C. Hammer, 1997, Primary aerosol (sea salt and soil dust) deposited in Greenland ice during the last climatic cycle: Comparison with east Antarctic records, *Journal of Geophysical Research*, 102 (C12), 26681-26698.

Fuhrer, K., E. W. Wolff, and S. J. Johnsen, 1999, Timescales for dust variability in the Greenland Ice Core Projct (GRIP) ice core in the last 100,000 years, *Journal of Geophysical Research*, 104 (D24), 31043-31052.

Hammer, C. U., H. B. Clausen, W. Dansgaard, A. Neftel, P. Kristinsdottir, and E. Johnson, 1985, Continuous impurity analysis along the Dye 3 deep core, in C.C.J. Langway, H. Oeschger, and W. Dansgaard (Eds.) *Greenland Ice Core: Geophysics, Geochemistry, and the Environmentl*, Geophysical Monograph 33, American Geophysical Union, Washington, 90-94.

Hansson, M. E., 1994, The Renland ice core. A Northern Hemisphere record of aerosol composition over 120,000 years, *Tellus*, 46B, 390-418.

Hinkley, T., F. Pertsiger, and L. Zavjalova, 1997, The modern atmospheric background dust load: recognition in Central Asian snowpack, and compositional contraints, *Geophysical Research Letters*, 24 (13), 1607-1610.

Johnsen, S. J., H. B. Clausen, W. Dansgaard, N. S. Gundestrup, C. U. Hammer, U. Andersen, K. K. Andersen, C. S. Hvidberg, D. Dahl-Jensen, J. P. Steffensen, H. Shoji, A. E. Sveinbjörnsdòttir, J. W. C. White, J. Jouzel, and D. Fisher, 1997, The $d^{18}O$ record along the Greenland Ice Core Project deep ice core and the problem of possible Eemian climatic instability, *Journal of Geophysical Research*, 102 (C12), 26397-26410.

Maggi, V., 1997, Mineralogy of atmospheric microparticles deposited along the Greenland Ice Core Project ice core, *Journal of Geophysical Research*, 102 (C12), 26725-26734.

Meese, D. A., A. J. Gow, R. B. Alley, G. A. Zielinski, P. M. Grootes, M. Ram, K. C. Taylor, P. A. Mayewski, and J. F. Bolzan, 1997, The Greenland Ice Sheet Project 2 depth-age scale: Methods and results, *Journal of Geophysical Research*, 102 (C12), 26411-26423.

Petit, J. R., J. Jouzel, D. Raynaud, N. I. Barkov, J.-M. Barnola, I. Basile, M. Bender, J. Chappellaz, M. Davis, G. Delaygue, M. Delmotte, V. M. Kotlyakov, M. Legrand, V. Y. Lipenkov, C. Lorius, L. Pépin, C.

Ritz, E. Saltzmann, and M. Stievenard, 1999, Climatic and atmospheric history of the past 420,000 years from the Vostok ice core, Antarctica, *Nature*, 399, 429-436.

Pye, K., 1987, *Aeolian dust and dust deposits*, Academic Press, London.

Rahn, K. A., and R. D. Borys, 1977, The Asian source of Arctic haze bands, *Nature*, 268, 713-715.

Ram, M., and G. Koenig, 1997, Continuous dust concentration profile of pre-Holocene ice from the Greenland Ice Sheet Projct 2 ice core: Dust stadials, interstadials, and the Eemian, *Journal of Geophysical Research*, 102 (C12), 26641-26648.

Röthlisberger, R., M. Bigler, M. Hutterli, S. Sommer, and B. Stauffer, 2000, A technique for contiunuous high resolution analysis of trace substances in firn and ice cores, *Environmental Science & Technology*, 34, 338-342.

Saey, P., 1998, *Concentration and size distribution of microparticles in alpine and polar ice cores (in German)*, M.Sc. thesis, Institut für Umweltphysik, University of Heidelberg, Heidelberg.

Steffensen, J. P., 1997, The size distribution of microparticles from selected segments of the Greenland Ice Core Project ice core representing different climatic periods, *Journal of Geophysical Research*, 102 (C12), 26,755-726,763.

Taylor, K. C., R. B. Alley, G. W. Lamorey, and P. Mayewski, 1997, Electrical measurements on the Greenland Ice Sheet Project 2 Core, *Journal of Geophysical Research*, 102 (C12), 26511-26517.

Tegen, I., and I. Fung, 1994, Modeling of mineral dust in the atmosphere: Sources, transport, and optical thickness, *Journal of Geophysical Research*, 99 (D11), 22897-22914.

Wolff, G. T., 1984, On the nature of nitrate in coarse continental aerosols, *Atmospheric Environment*, 18 (5), 977-981.

Wurzler, S., T. G. Reisin, and Z. Levin, 2000, Modification of mineral dust particles by cloud processing and subsequent effects on drop size distributions, *Journal of Geophysical Research*, 105 (D4), 4501-4512.

**FIGURES AND TABLE S**

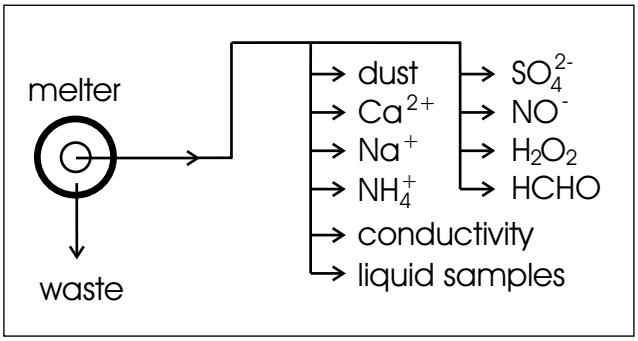


*Figure 1. Flowchart of the analytical setup (highly simplified).*

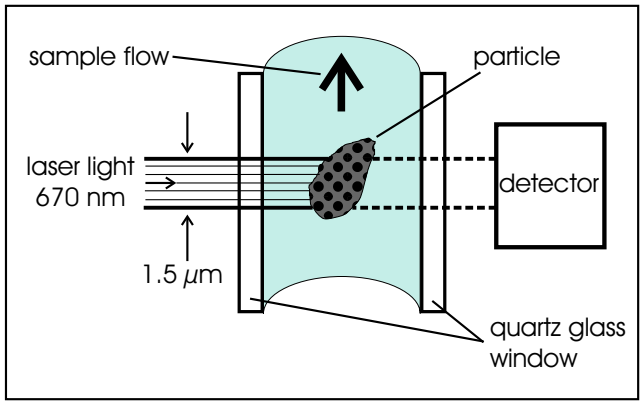


*Figure 2. Detection cell of the laser sensor (schematic). The cross section of the cell is 230 µm × 250µm; the laser beam is 250 µm × 1.5 µm wide.*

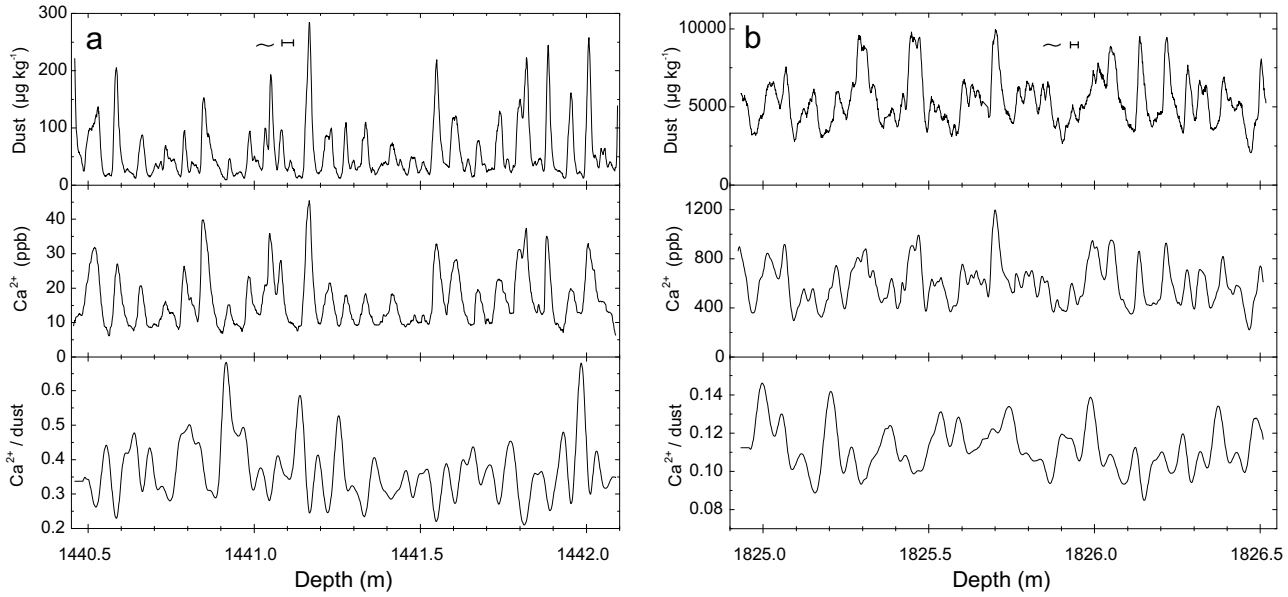


*Figure 3. Examples of the insoluble dust and the $Ca^{2+}$ measurements: (a) is in Holocene, (b) is during LGM. Also shown is the $Ca^{2+}$/dust ratio, which is smoothed (see text). A preliminary estimate of annual layer thicknesses $\lambda$ is included. Note the different scales in all panels for (a) and (b).*

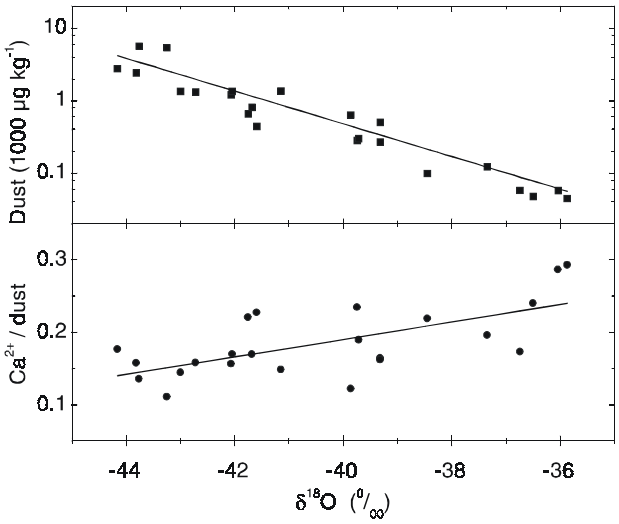


*Figure 4. $Ca^{2+}$/dust ratio and mean dust concentration for all 23 sections plotted against $\delta^{18}O$. Each data point represents a 1.65 m long intervall.*

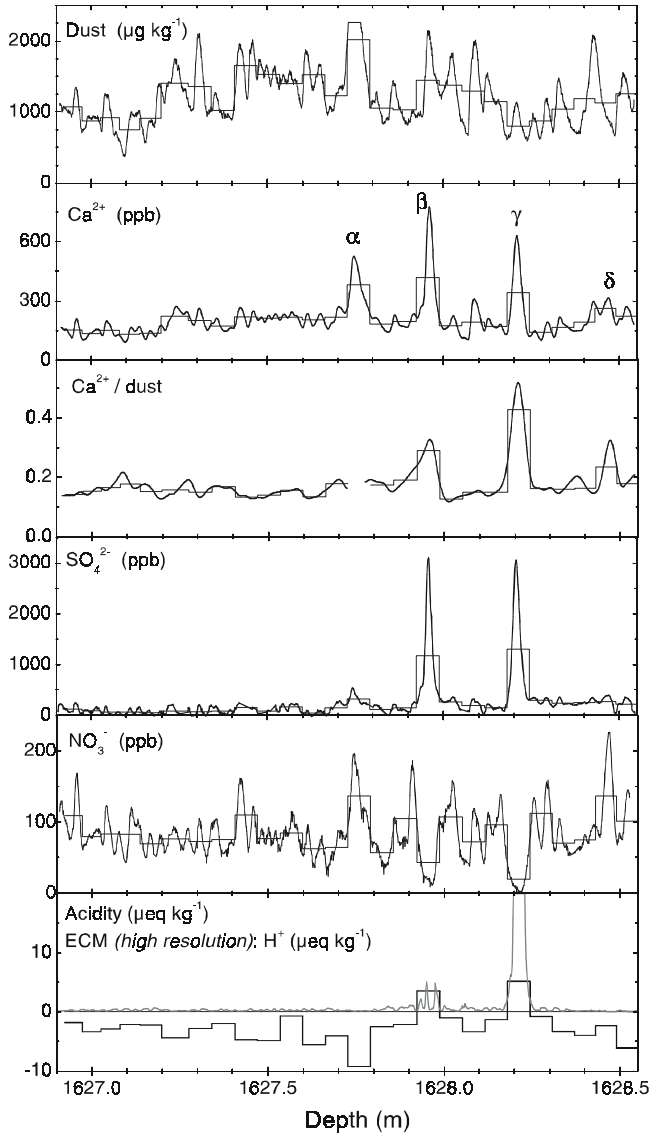


*Figure 5. Examples of anomalous events in the microparticle and $Ca^{2+}$ profiles. The sample is from the cold stadial between IS 1 and 2. The data for dust, $Ca^{2+}$, $SO_4^{2-}$, and $NO_3^-$ were obtained by CFA; the $Ca^{2+}$/dust ratio was smoothed (see text); acidity was measured at approx. 6 cm depth resolution; in the same panel the ECM data is shown in high resolution (preliminary calibration). The fine histogram style lines represent the high resolution data reduced to the resolution of the acidity measurement. Labeled $Ca^{2+}$ peaks refer to events discussed in text.*

| mid-depth (m) | climatic period | $\delta^{18}O$ ($^0/_{00}$) | mean dust (µg $kg^{-1}$) | mean $Ca^{2+}$/ mean dust | unusual $Ca^{2+}$/dust | ECM peak | $SO_4^{2-}$ peak |
|---|---|---|---|---|---|---|---|
| 1424.8 | hol | -35.87 | 44 | 0.29 | - | na | - |
| 1441.3 | hol | -36.04 | 57 | 0.29 | - | na | - |
| 1459.4 | hol | -36.74 | 58 | 0.17 | + | na | + |
| 1479.2 | hol | -38.45 | 99 | 0.22 | - | na | + |
| 1486.9 | hol | -36.60 | 48 | 0.24 | - | na | - |
| 1627.7 | c-1/2 | -42.07 | 1200 | 0.16 | + | + | + |
| 1642.6 | c-1/2 | -42.05 | 1347 | 0.17 | + | + | + |
| 1688.8 | c-1/2 | -42.73 | 1318 | 0.16 | + | + | + |
| 1716.8 | c-1/2 | -41.15 | 1353 | 0.15 | + | + | + |
| 1805.9 | LGM | -43.76 | 5589 | 0.14 | - | - | + |
| 1825.7 | LGM | -43.25 | 5373 | 0.11 | - | - | - |
| 1855.4 | LGM | -43.00 | 1337 | 0.14 | + | + | + |
| 1895.0 | c-4/5 | -44.16 | 2755 | 0.18 | - | -* | + |
| 1931.3 | c-4/5 | -43.82 | 2418 | 0.16 | + | + | + |
| 2252.5 | IS13 | -41.59 | 440 | 0.23 | + | + | + |
| 2254.2 | IS13 | -39.75 | 280 | 0.23 | + | + | + |
| 2390.0 | IS16 | -39.72 | 298 | 0.19 | + | + | + |
| 2399.9 | c-16/17 | -41.68 | 810 | 0.17 | - | -* | + |
| 2708.5 | c-21/22 | -41.76 | 650 | 0.22 | + | - | + |
| 2901.5 | c-pre23 | -39.86 | 634 | 0.12 | - | - | - |
| 2904.8 | c-pre23 | -39.32 | 502 | 0.16 | + | - | + |
| 2918.0 | w-23/5e1 | -37.34 | 122 | 0.20 | - | - | - |
| 2921.3 | c-post5e1 | -39.32 | 268 | 0.16 | + | - | + |

*Table. 1. Overview of the NGRIP core sections used for this study. All sections are 1.65 m long. The climatic period is preliminary; it was determined by matching the NGRIP dust profile to the GRIP $\delta^{18}O$ profile (Johnson and others, 1997). The NGRIP $\delta^{18}O$ values given are from personal communication from NGRIP members (2000). hol: Holocene; IS n: GRIP interstadial n; c m/n: cold stadial between SI m and SI n; LGM: last glacial maximum; pre23c: cold stage before IS23; w23/5e1: intermittent warm stage between IS23 and 5e1; post5e1: cold stage after 5e1. na: data not available; '+': existing; '-': not existing; '-*': no ECM peak observed but a visible ash layer.*

| | |
|---|---|
| Mean crust (igneous rocks) | 0.041 |
| Mean sediment | 0.066 |
| Marine carbonates | 0.203 |
| Mean limestone | 0.340 |
| Soils | 0.015 (0.0007 – 0.50) |

*Table. 2. Mean weight fractions of Ca in different types of crust material (adapted from Bowen, 1978).*

# Chapter 5

# Continuous record of microparticle concentration and size distribution in the central Greenland NGRIP ice core during the last glacial period

Urs Ruth, Dietmar Wagenbach, and Jørgen P. Steffensen

Submitted to *Journal of Geophysical Research*

# Continuous record of microparticle concentration and size distribution in the central Greenland NGRIP ice core during the last glacial period

Urs Ruth[1,2], Dietmar Wagenbach[1], and Jørgen P. Steffensen[3]

[1]Institut für Umweltphysik, University of Heidelberg, Germany
[2]Alfred Wegener Institut für Polar- und Meeresforschung, Bremerhaven, Germany
[3]Department of Geophysics, University of Copenhagen, Denmark

**Abstract** The application of a novel laser particle detector in conjunction with controlled longitudinal sample melting has provided a more than 1500 m long continuous record of microparticle concentration and size distribution of the NGRIP ice core. The resulting profile has a depth resolution of 1.65 m and covers almost the complete last glacial period. The microparticle concentration increases by a factor of 100 in the Last Glacial Maximum (LGM) compared to the Preboreal. At rapid climatic transitions sharp variations of the concentration occur synchronously with changes of the $\delta^{18}$O temperature proxy. The lognormal mode $\mu$ of the volume distribution also shows clear systematic variations with smaller particles during warmer climates. We find $\mu \approx 1.7$ $\mu$m diameter during LGM and $\mu \approx 1.3$ $\mu$m during the Preboreal. During warm periods $\mu$ was more variable as reflected by increased point-to-point variability and also by increased values of the standard deviation of the distribution for the multi-year samples considered here. On timescales below several 100 years $\mu$ and the particle concentration exhibit a certain degree of independence noticeable especially during warm periods. Using highly simplifying considerations of the atmospheric dust cycle we find that (i) the observed changes of $\mu$ in the ice largely reflect changed airborne particle sizes above the ice sheet and (ii) that changes of $\mu$ are indicative for changes of atmospheric long range transport times. From the observed size changes we deduce roughly 25% shorter transit times during LGM compared to the Preboreal. The associated concentration increase from this change is roughly estimated to less than one order of magnitude.

# Introduction

Ice cores provide a wealth of paleoclimatic information including records of windblown mineral aerosol (hereinafter also called dust). Among all deposited components this atmospheric constituent has a special quality because not only its concentration but also the size distribution of its insoluble fraction is preserved. As East Asian deserts have been identified as the most probable source area for dust transported to Greenland [*Biscaye et al.*, 1997; *Kahl et al.*, 1997; *Svensson et al.*, 2000] long range atmospheric transport plays a central role in the dust cycle. Therefore, archives of the dust aerosol may hold specific information about atmospheric transport in particular.

Mineral dust concentrations in ice cores exhibit a large dynamic variation throughout a climatic cycle. Dust concentrations vary by a factor of ≈100 between the Holocene and the Last Glacial Maximum (LGM) in central Greenlandic ice [*Steffensen*, 1997]. From continuous microparticle and $Ca^{2+}$ measurements in the Renland ice core [*Hansson*, 1994] and on the basis of continuous $Ca^{2+}$ records from the GRIP ice core [*Fuhrer et al.*, 1999] it was demonstrated that at rapid climatic transitions the dust concentration varied synchronously with the $\delta^{18}O$ temperature proxy. While early explanations for the pronounced increase in dust concentration suggested the importance of exposed continental shelves due to a lower sea level during the last glacial [*Cragin et al.*, 1977; *Hammer et al.*, 1985], more recent work negates this idea [*Steffensen*, 1997] and rather points to changed atmospheric conditions [*Petit et al.*, 1981; *Petit et al.*, 1990] and intensified sources [*Fuhrer et al.*, 1999]. Further specification of this general inference remains difficult as the observed dust concentrations are a combined result of a number of entangled mechanisms ranging from dust mobilization in the source areas over uplift and long range transport to deposition onto the ice sheet.

*Fuhrer et al.* [1999] have addressed some of the involved processes, but the fact that changes of source aridity, surface wind speed, uplift, transport, and deposition may all have been variable on similar timescales and also synchronized [*Porter and Zhisheng*, 1995; *Wang et al.*, 2001] makes it very difficult to separate individual processes. As yet, only rough estimates can be expected from modelling approaches because dust models - although having improved considerably - are still barely reproducing the concentration change observed in polar archives and cannot confidently resolve the individual processes involved [*Andersen et al.*, 1998; *Mahowald et al.*, 1999; *Tegen and Rind*, 2000]. Also, models are so far unable to describe mixing mechanisms in the lower boundary layer at the ice sheet which are important for the deposition process.

Size distribution measurements on the insoluble fraction of dust in polar ice cores have shown that the majority of the particle mass can be described by a lognormal

distribution with a modal diameter around 1.5 to 2.0 $\mu$m [*Royer et al.*, 1983]. This mode is found to be fairly robust in remote regions world wide. But small systematic shifts have been observed on various time scales in ice cores from Greenland as well as from Antarctica, e.g. [*Steffensen*, 1997; *Delmonte et al.*, 2002]. As particle size distributions may be indicative for atmospheric circulation it may be possible to use this information to gain further insights into the past dust cycle. But size distribution measurements are scarce. So far they have been performed only in a discontinuous spot check manner using microscopy or the well established Coulter counting technique. For Greenland, *Steffensen* [1997] finds a tendency towards larger lognormal modes for colder climates, which are associated with higher dust concentrations.

The interpretation of the observed particle sizes is not straight forward. It is known that depletion processes during long range transport are generally size fractionating [*Junge*, 1977], that size altering in-cloud processing may occur [*Wurzler et al.*, 2000], and that the deposition process to the ice sheet bares the potential of changing the size distribution [*Unnerstad and Hansson*, 2001]. But a quantification of these processes is difficult, and our current understanding about how different climatic situations may have influenced the particle size distribution is limited. Also, the forward modelling of particle size distributions is not very accurate. Dust modules for general circulation models (GCM) work with one or only few size classes (e.g. four classes covering the range from 1 to 100 $\mu$m [*Tegen and Fung*, 1994]) and cannot resolve fine shifts of the lognormal mode.

So far, no continuous profile covering the last glacial period has been provided from ice cores for microparticle size distribution parameters. In particular, it is unclear how the size distribution behaved at fast climatic transitions. Also, possible inferences from changed size distributions for atmospheric circulation changes are not well understood.

Here we present a comprehensive data set from the North Greenland Ice Core Project (NGRIP) deep ice core, drilled at (75.1N, 42.3W) in central Greenland about 300 km north of the summit region. The record is approximately from 1400 m to 2930 m depth and covers continuously the period from $\approx$9.5 kyr before present (bp) to $\approx$100 kyr bp, i.e. it includes the Pleistocene to Holocene transition and almost the complete ultimate glacial period. The core was analyzed continuously for insoluble microparticle concentration and size distribution deploying a novel laser based sensor. This sensor is not as delicate and does not require as extensive sample preparation as a Coulter Counter, which makes it possible to acquire a continuous profile over this long depth interval. To find an interpretation of the observed size changes, we present a simple model picture that that describes the modification of a particle size distribution during long range transport and deposition.

# Methods

**Measurements** The measurement procedure and the laser based particle detector have already been described by [*Ruth et al.*, 2002] and therefore are only briefly outlined here. However, the aspect of the size calibration will be covered in greater detail. The measurements took place in a warm laboratory during the NGRIP-2000 field campaign. Continuous sections of core were melted in a controlled fashion along the core direction. The melt water was subjected to established continuous flow analysis (CFA) systems (e.g. [*Röthlisberger et al.*, 2000]; M. Bigler, *Dissertation in preparation*, University of Berne) and to particle analysis, which all work on a flow-through basis. For decontamination purposes the abutting faces of the core sections were carefully cleaned using a stainless steel microtome blade. In addition, the melter had two concentric sections, and only the uncontaminated meltwater from the inner section was used for the analyses as described by *Röthlisberger et al.* [2000]. Peristaltic pumps and teflon tubings were used to feed the water into the detection units. Debubblers were used to eliminate air bubbles.

In our measuring procedure the size distribution data was accumulated over 1.65 m intervals, while the particle concentration may also be recorded at an effective depth resolution of 1.0 cm [*Ruth et al.*, 2002]. Count rates were transformed to concentrations by means of regular flow rate measurements. To avoid coincidence distortion of the particle counting the sample water of glacial ice was diluted with prefiltered (0.2 $\mu$m) carrier water. Dilution was performed below 1494.9 m depth, i.e. for ice from the Younger Dryas period and older. The total sample volume consumed for a 1.65 m long section was approximately 6 ml.

**Size calibration of the particle sensor** The particle detection is based on laser light attenuation by single particles. The sample water is pumped through an illuminated detection cell, where each particle is detected as a negative peak of transmitted light. The peaks are counted and sorted by height into channels, that can be adjusted to appropriate size intervals. 12 channels were used in this application.

The interrelation of peak height and particle size is complex as both geometric shadowing and scattering processes are involved. Shadowing depends on geometric particle cross section, and therefore on a combination of particle volume, shape and orientation. Scattering in addition depends on optical particle properties and features nonlinearities between particle size and scattered light intensity. Only in the upper end of the size spectrum geometric shadowing dominates enough to allow a calibration with latex spheres of known diameter. In the remaining main part of the spectrum

scattering becomes increasingly important, and a size calibration with latex spheres is inaccurate because mineral aerosol particles have different scattering properties than latex spheres of identical volume, predominantly due to their non-spherical shape [*Saey*, 1998].

Therefore, a size calibration was achieved indirectly through a comparison with measurements using a Coulter Counter, which measures the particle volume directly and independently of shape. At selected horizons, NGRIP ice core samples were also measured with a Coulter Counter, and subsequently the laser sensor size axis was adjusted until the laser sensor data and the Coulter Counter data showed optimal correspondence. Samples from five different climatic periods (Preboreal Holocene, Younger Dryas (YD), Allerød, LGM, and pre-LGM cold glacial (CG)) were used for the calibration, thus the full concentration range was covered.

During the calibration process it was discovered that the dilution setup had had a modifying influence on the size distribution. Therefore, the measurements of Preboreal Holocene ice (without dilution setup) and glacial ice (with dilution setup) were calibrated separately. Figure 1 shows the volume distribution spectra used for the two calibrations. The Preboreal sample was used to calibrate the measurements above 1494.9 m depth, that were done without sample dilution (A). For the calibration of the measurements below this depth the other four samples were used (B). After the adjustment of the laser sensor size axis, the data sets of the two counters show good accordance. Differences between the laser sensor and the Coulter Counter data may result from the fact that the Coulter Counter data covers only 0.55 m out of the 1.65 m long section measured with the laser sensor so that the underlying size distributions possibly indeed slightly differed in the respective samples. For calibration (B) the differences in the underlying sample populations counterbalance each other as several horizons could be used for one calibration.

**Data parametrization** A lognormal function was used to parametrize the volume distribution data:

$$\frac{dV}{d\ln d} = \frac{V_0}{\sqrt{2\pi}\ln\sigma} e^{-\frac{1}{2}\left(\frac{\ln d - \ln \mu}{\ln \sigma}\right)^2},$$

where $V_0$ is the amplitude, $\mu$ the mode and $\sigma$ the standard deviation of the distribution (herein also called 'lognormal mode' and 'lognormal standard deviation' for simplicity). Because the width of the size channels was quite large the fit procedure regarded the distribution within each channel. Furthermore, the fitting procedure was such that not the absolute but the relative quadratic error was minimized in order to put equal weight on all channels. The first nine channels were considered for fitting, i.e. particles

between 1.0 $\mu$m and 7.5 $\mu$m diameter.

Other parameters are sometimes taken to characterize a particle size distribution: The volume $V_c$ of coarse particles ($d > d_c$) is used as well as the relative coarseness as $V_c/V_{tot}$; $d_c$ was chosen to 7.5 $\mu$m in our study. The parameters 'mean volume diameter' (MVD) and 'mean number diameter' (MND) as e.g. used by [*Zielinski*, 1997] denote the mean diameter with respect to volume or number. As they highly depend on the measuring range and thus are intercomparable only for identically treated data sets we do not discuss them here. Furthermore, the MVD was found to be ambiguous in our data: At high dust concentrations it tended to be in phase with changes of the lognormal mode $\mu$ and in antiphase with the relative coarseness (i.e. it depended on the size of small particles); yet at low concentrations it tended to be in antiphase with the mode and in phase with relative coarseness (i.e. it depended on the abundance of large particles).

Because a considerable portion of the microparticle mass is contributed by the small particles below the detection limit of approximately 1.0 $\mu$m, insoluble microparticle mass concentrations reported in this paper are derived as follows: For $d > \mu$ the total measured particle volume $V_m^{d>\mu}$ is taken by summation of all relevant channels or fractions thereof; below the mode the volume is taken from the fitted lognormal distribution, i.e. $V_{tot} = V_m^{d>\mu} + 0.5 \cdot V_0$. Subsequently, the total mass concentration is inferred by assuming a material density of 2.6 g cm$^{-3}$ [*Sugimae*, 1984].

**Measurement errors** Occasionally, sections were affected from system malfunction. These could be identified from laboratory log entries and unrealistically strong excursions of the MND and were excluded from further processing. Few sections showed a very high concentration of large particles possibly resulting from contamination and were also excluded. The measurement blank for small particles was below 15% of the count rate for most low concentration samples and was negligible in high concentration samples; for coarse particles the measurement blank relative to the particle count rate was higher and more variable. Since for coarse particles also counting statistics deteriorate caution must be taken when interpreting the volume of the coarse fraction. The error of the total number concentration for all particles is predominantly due to flow rate uncertainties and is estimated to typically 5% - 10%. The uncertainty of total volume or mass concentration as due to flow rate and size calibration uncertainties is estimated to be about 15% - 20%.

The determination of the particle size is hindered through the influence of the flow set up on the size distribution, which may not be constant and therefore not at all times be fully compensated for by the calibration. Further, the calibration is affected

from the fact that the Coulter Counter data covers only part of the sample population measured with the laser sensor, which may explain the difference of about 0.1 $\mu$m between the fit parameter $\mu$ when derived from the Coulter Counter or the laser sensor data (see Figure 1). The difference in $\mu$ that result from using calibration A or B for any given sample was typically around 0.04 $\mu$m. The analytical uncertainty of the fit is variable and lies in the range from 0.01 $\mu$m to 0.1 $\mu$m diameter. We therefore estimate the possible error for $\mu$ to be generally around 0.1 $\mu$m diameter; it may be larger for the Holocene samples, where only one calibration horizon exists and also the uncertainty of the fit is large. Double measurements on ice from the YD-Holocene transition, one time performed without and the other time with the dilution setup, yielded a discrepancy in $\mu$ of up to 0.1 $\mu$m, which supports the above estimates.

The laser sensor was easy to handle and proved suitable for deployment under field conditions. It was possible to calibrate the laser sensor for proper sizing of windblown mineral dust particles. In future usage the flow system between melter and sensor should be as short as possible and kept unchanged throughout the measurements. Calibrations should be based on multiple horizons from different climatic periods, where applicable.

# Results

**Size distributions** Four individual volume size distributions are shown in Figure 2 for illustration. They are representative for different climatic periods, namely LGM (a), Stadial (S) S9 (b), Interstadial (IS) IS10 (c), and Preboreal Holocene (d). The samples span a concentration range of more than two orders of magnitude for particles smaller than 7.5 $\mu$m. For coarse particles larger than 7.5 $\mu$m the concentration range of the four samples is less than one order of magnitude and is not strictly correlated to the concentration of small particles.

The respective lognormal fits are also shown in Figure 2, and the position and uncertainty of the lognormal mode $\mu$ are indicated. The fits describe the measured distributions very well for high concentration samples. For low concentration samples the description is still satisfactory, however deviations of the data from the ideal model distribution are larger. It may also be noticed that for higher concentration samples the position of the mode tends to increase whereas the width of the distribution tends to decrease.

**Profiles** Particle concentration and size distribution parameters of all samples are plotted as depth profiles in Figure 3. Shown are the insoluble particle number concen-

tration $C_N$, mass concentration $C_M$, lognormal mode $\mu$ of the volume distribution, and lognormal standard deviation $\sigma$. The concentration profiles clearly exhibit all climatic events known from the Greenlandic GRIP and GISP2 deep ice core records [*Johnsen et al.*, 1997; *Grootes and Stuiver*, 1997], some of which have been labeled in the figure. In particular, the stadial-interstadial fluctuations (or Dansgaard-Oeschger (D/O)-events) are clearly resolved. Periods of low particle concentrations correspond to warm phases while cold phases correspond to high particle concentrations. Concentrations are lowest during Preboreal Holocene ($C_N \approx 1 \cdot 10^4$ ml$^{-1}$ or $C_M \approx 70$ $\mu$g kg$^{-1}$) and highest during LGM ($C_N \approx 1 \cdot 10^6$ ml$^{-1}$ or $C_M \approx 8000$ $\mu$g kg$^{-1}$). This compares well to the reported microparticle mass concentrations from the GRIP core of 50 $\mu$g kg$^{-1}$ and 8000 $\mu$g kg$^{-1}$ for Preboreal and peak-LGM respectively [*Steffensen*, 1997]. Discrepancies to the GRIP data may be due to differences in the methods of measurement and data evaluation and need not be of geographical origin. The relative changes of the mass concentrations across D/O-transitions range from a factor of 5 to 18 and are typically around 8.

The overall appearance of the insoluble microparticle concentration profile as expected resembles much the continuous $Ca^{2+}$ concentration profile from the GRIP core [*Fuhrer et al.*, 1999]. This means that the soluble and insoluble parts of the mineral aerosol varied largely alike. However, systematic changes of the $Ca^{2+}$/microparticle ratio by a factor $\leq 2$ may be expected [*Steffensen*, 1997; *Ruth et al.*, 2002].

The close correspondence of the microparticle profile to the GRIP $Ca^{2+}$ or $\delta^{18}O$ profiles permits to establish a provisional timescale for our NGRIP microparticle data by matching respective climatic events and subsequently transferring the GRIP SS09 timescale [*Johnsen et al.*, 1997] to the NGRIP core. Thereby we infer that the time coverage of each 1.65 m section ranges between 35 and 200 years. We also find that the concentration changes at D/O-transitions may have happened within 100 years or less.

Also the mode $\mu$ shows considerable systematic variability throughout the record, and most major climatic events as identified from the concentration profiles are also visible in the size distribution. These are in particular the YD and B/A periods, and the more prominent D/O-events; but also smaller D/O-events or the LGM as a whole are identifiable in the profile. Typical values for $\mu$ in the Preboreal are around 1.3 $\mu$mdiameter; and peak values exceed 1.7 $\mu$m during LGM. Typical values within the Pleistocene are around 1.6 $\mu$m during cold periods and may decrease to values around 1.4 $\mu$m or less during interstadial warm periods. A marked increase of the mode can be noticed between 2600 m and 2500 m depth, which corresponds to the transition from Marine Isotope Stage (MIS) 5 to MIS 4. Below this depth (i.e. during MIS 5) $\mu$

was generally about 0.2 $\mu$m smaller than above. During corresponding periods we find roughly 0.2 $\mu$m smaller modes than *Steffensen* [1997] does for selected periods in the GRIP ice core.

The switching of the mode between states may happen as fast as the concentration changes, but it is not always as evident. Further, $\mu$ tends to be more variable (point-to-point variation) when crustal concentrations are low. This higher variability persists even when the data is averaged to equally long time periods; so it is not a consequence from formal counting statistics nor from the fact that low concentration samples systematically cover shorter time spans.

The lognormal standard deviation also shows systematic variations. It ranges from about 1.55 during LGM to more than 2 during the warm periods of MIS 5. It tends to be high when $\mu$ shows a large point-to-point variability. This indicates that at these times the mode was more variable also *within* each 1.65 m section.

**Systematic changes of the mode** In Figure 3 it is observed that the mode tends to increase for large particle concentrations. A systematic plot of these two parameters is shown in Figure 4a, where the data shown is averaged to 200 years resolution to reduce the point-to-point scatter for periods with higher layer thickness. A clear positive correlation is exhibited. It also can be noted that the spread of the mode is by about a factor of 3 smaller for high than for low particle concentrations. Larger modes and smaller spread for high concentration samples are also observed if the data is averaged over climatic periods (Figure 4b).

**Detailed profile section** A closer look at rapid transitions may bring further insights into the dust regime. Figure 5 shows the zoomed profile from IS 9 through IS 12 with size distribution parameters, particle concentration, and $\delta^{18}$O (isotope data: personal communication from NGRIP-members, unpublished data). Cold periods very clearly show high dust concentrations and vice versa. Further, almost all high concentration periods are concurrent with large modes; however, not all periods with low concentrations are accompanied by smaller modes, and during low concentration periods the mode is more variable. This shows an independence of $\mu$ and $V$ which is especially pronounced during warm periods.

The fact that the mode is more variable during warm periods may cause confusion when determining the exact point of a transition. One such occasion at the beginning of IS 11 is marked in Figure 5 with an arrow. Here, the size distribution shifts synchronously with the concentration into the "warm"-state as can be seen from the profile of $\sigma$. However, its increased variability allows the mode to stay large for two more sam-

ples (corresponding to roughly 200 years). Only the increased values for $\sigma$ show that the individual dust events contributing to the multi-year samples were already more variable with respect to particle size, as is typical for warm periods. Therefore, $\sigma$ is a more reliable parameter than $\mu$ when the exact point of a D/O-transition needs to be determined from size distribution parameters on the basis of multi-year samples.

Another observation is that there may indeed be a difference in the particular time when a transition occurs in the concentration and in the size distribution of microparticles (circles in Figure 5). No systematic leads or lags seem to occur, but shifts range up to $\pm$200 years. This again shows some independence of the processes influencing the particle concentration or size distribution. Such processes may have included variations of source strength and the amount of non-sizefractionating depletion processes during transport (see below). The independence is observed especially during warm periods, and it vanishes if the data is averaged for several centuries.

## A simple model picture

The atmospheric dust cycle starts with the production of small sized wind-deflatable material in the source areas by weathering processes [*Pye*, 1987]. The amount of entrained dust depends on the occurrence and strength of surface winds, the size of the source areas and the mobility of the dust therein [*Gillette et al.*, 1980]. The geographical overlap of source region and long range transport zones may be another important factor [*Chylek et al.*, 2001]. The transport of dust depends on long range transport patterns, which in turn are influenced by e.g. global heat distribution or the ice cover of land and ocean [*Krinner and Genthon*, 1998]. Transport efficiency depends on sink processes leading to particle loss en route. Finally, the deposition of microparticles onto the ice sheet depends on wet and dry deposition processes [*Davidson et al.*, 1996].

In the following we will elucidate the potential of some of these processes to change the size distribution of an ensemble of particles. We will investigate to what extent the observed size distribution changes of microparticles may be due to changed deposition conditions during different climates, and how atmospheric circulation needs to have been different to account for the remaining size change. Hereby, our very simple approach clearly is far from capturing reality in all its complexity; but at least the direction of effects should be confidently resolved, and rough estimates of the magnitude of effects may be gained.

For comparison of two climatic states in the following sections we use the upper index '*cold*' to denote a cold state and the upper index '*warm*' to denote a warm state.

## Size fractionation during deposition

Particles are transfered from the air to the snow by dry and wet deposition. Wet deposition includes all precipitation related events and is described by an effective wet deposition velocity $v_w$. The continuously occurring dry deposition processes include all sinks not directly related to precipitation, i.e. mainly sedimentation, impaction, and snow drift scavenging, and are summarized as an effective total dry deposition velocity $v_d$. We consider only multi-year means (disregarding e.g. changed seasonality of precipitation [*Werner et al.*, 2000]) and assume that the precipitation rate equals the accumulation rate; then the deposition flux is proportional to $(v_w + v_d)c_{air} = (\varepsilon A + v_d)c_{air}$ with

$\varepsilon$: scavenging ratio, i.e. particle concentration in new snow divided by $c_{air}$,

$A$: accumulation rate, and

$c_{air}$: airborne particle concentration.

In a first order approximation size fractionation by dry deposition may be described as $v_d = kd^n$ ($d$: particle diameter, $k$ and $n$: constants), although for large particles $v_d$ may be rate limited through insufficient vertical exchange. Wet deposition may be regarded as so efficient that at least for high enough precipitation rates its size fractionating potential [*Junge*, 1977] is quenched; thus we assume $\varepsilon$ independent from particle size. In this picture the size distribution is shifted towards larger particles by dry deposition but not by wet deposition, and consequently the resulting size distribution in the ice depends on the ratio of dry and wet deposition fluxes. Therefore, a change in the accumulation rate will change the archived size distribution (see also [*Unnerstad and Hansson*, 2001]).

The unimodal, lognormal size distribution $\langle \mu_{air}, \sigma \rangle$ with mode $\mu_{air}$ and standard deviation $\sigma$ transforms during deposition as $\langle \mu_{air}, \sigma \rangle \cdot (v_w + v_d)$. The mode $\mu_{ice}$ of the size distribution in the ice is found at the maximum of this product and is given by (using the notation $\sigma_g = \ln \sigma$)

$$\ln\left(\frac{\mu_{ice}}{\mu_{air}}\right) = n\sigma_g^2 \frac{v_d}{v_w + v_d} = n\sigma_g^2 \frac{k\mu_{ice}^n}{A\varepsilon + k\mu_{ice}^n}.$$

Obviously, the maximum shift occurs if only dry deposition is active; in that extreme case $\frac{\mu_{ice}}{\mu_{air}} = \exp\left(n\sigma_g^2\right)$; and with $n = 2$ (sedimentation) and $\sigma = 1.7$ a factor of $\approx 1.7$ is obtained.

Because the accumulation rate differed during different past climates the size shifts due to deposition were also different. To investigate to which extent the observed systematic changes of $\mu_{ice}$ may arise from this depositional effect we calculate the size shift for two different accumulation rates. We choose $\mu_{air} = 1.4$ $\mu$m and assume

constant values for $n$ ($n = 2$), $\sigma$ ($\sigma = 1.7$), $k$ ($k = 8.3 \cdot 10^7$ m$^{-1}$s$^{-1}$ from [*Fuchs*, 1964]), and $\varepsilon$. The values vor $\varepsilon$ are not well known, but $0.2{\cdot}10^6 \leq \varepsilon \leq 2.0{\cdot}10^6$ seems probable as *Davidson et al.* [1996] find $\varepsilon = (0.65 \pm 0.31) \cdot 10^6$ for $Ca^{2+}$ at Summit. For $A^{warm} = 0.2$ ma$^{-1}$ and $A^{cold} = 0.5A^{warm}$, which reflects LGM vs. Preboreal accumulation changes [*Johnsen et al.*, 1997], we obtain a difference $\Delta = (\mu_{ice}^{cold} - \mu_{air}^{cold}) - (\mu_{ice}^{warm} - \mu_{air}^{warm})$ of $\Delta = 0.08$ $\mu$m for $\varepsilon = 0.2 \cdot 10^6$ and $\Delta = 0.01$ $\mu$m for $\varepsilon = 2.0 \cdot 10^6$, which typically is about 1/4 of the absolute shifts $\mu_{ice} - \mu_{air}$ between airborne and deposited particles in our calculations. Similar results are achieved if more realistic calculations of $v_d$ are used [*Sehmel*, 1980].

These calculated differences compare to our observed changes of $\mu_{ice}$ of approx. 0.4 $\mu$m for LGM vs. Holocene climatic changes. Thus, the differences in particle deposition during warm and cold climates can only account for roughly 3% to 20% of the observed change of $\mu$. We therefore conclude that the observed differences of $\mu$ during different climatic periods predominantly reflect changed airborne size distributions over Greenland. (See Figure 7 for an illustrative sketch.)

## Size fractionation during emission, uplift and long range transport

**Emission** According to *Gillette et al.* [1974] the wind speed has little influence on the size distribution in the range from 2-10 $\mu$m. And also *D'Almeida and Schütz* [1983] find that dust storms do not change the size distribution of airborne mineral dust particles below 10 $\mu$m diameter. Only above 10 $\mu$m the abundance of large particles increases during high surface winds. Because we consider only particles smaller than 10 $\mu$m we assume the size distribution of airborne particles a few meters above the ground as independent from the source strength. The mode of this distribution be $\mu_{source}$.

**Uplift and long range transport** The change of particle concentration during transport can be described by the term $f \cdot e^{-t/\tau}$, with
$t$: transit time between free troposphere at source and deposition onto the ice sheet,
$\tau$: residence time governed by depletion processes en route, and
$f$: correction factor in our one-dimensional approach to account for external mixing with particle free air (dilution).
Size fractionating depletion processes may be accounted for by allowing the residence time to be size dependent, i.e. $\tau = \tau(d)$. For long range transport we assume $\tau(d) = \frac{H}{\tilde{v}_w + \tilde{v}_d}$, where $H$ denotes the mixing height, $\tilde{v}_w$ describes the depletion process due to wet depletion en route and $\tilde{v}_d$ due to dry depletion en route. Note that for the depletion

processes during transport considered here $\tilde{v}_w$ and $\tilde{v}_d$ may be very different from the deposition velocities $v_w$ and $v_d$ at the ice sheet considered earlier. Dry deposition again is assumed to be size fractionating according to $\tilde{v}_d = kd^n$, and also here $\tilde{v}_w$ is assumed to be so efficient that its size fractionating character is overridden. Any size fractionating portions of $\tilde{v}_w$ that possibly remain may be treated as increased dry depletion in this picture.

Following the motion of an air parcel, an unimodal, lognormal size distribution $\langle \mu_0, \sigma \rangle$ transforms as $\langle \mu_0, \sigma \rangle \cdot f \cdot e^{-t\frac{\tilde{v}_w + \tilde{v}_d}{H}}$. The resulting distribution is not necessarily exactly lognormal; however, the new mode $\mu$, which again is found at the maximum of this product, is characterized by:

$$\ln\left(\frac{\mu}{\mu_0}\right) = -n \cdot \sigma_g^2 \cdot \frac{t}{\tau} \frac{\tilde{v}_d}{\tilde{v}_w + \tilde{v}_d} \tag{1}$$

which means that $\mu$ decreases with time. Simultaneously the distribution gets narrower, i.e. $\sigma_g$ also decreases. Consequently, the change of $\mu$ is more rapid at the beginning when $\sigma_g$ is large.

We now compare the size change during long range transport at a cold and warm climatic state. To meet problems from possibly different uplift rates during cold and warm climates we define long range transport to start once a reference size distribution with the mode $\mu_{ref}$ is reached in the free troposphere. Thus, by definition, in our model picture $\mu_{ref}^{cold} = \mu_{ref}^{warm}$. This may also be the case in reality, however, our current knowledge about this is poor. If the uplift rates were different during cold and warm climatic states then in one state the air parcel will already have travelled farther until $\mu_{ref}$ is reached, thus reducing somewhat the distance to be covered by long range transport. However, since the horizontal displacement during uplift is small compared to the distance to be covered by long range transport and since the mode changes relatively quickly at the beginning a possible difference in uplift will have only a small adverse effect on our model results.

In this picture the ratio $\frac{\mu_{air}^{cold}}{\mu_{air}^{warm}}$ of the airborne modes at the ice sheet can be deduced from equation 1 as

$$\ln\left(\frac{\mu_{air}^{cold}}{\mu_{air}^{warm}}\right) = -\ln\left(\frac{\mu_{air}^{warm}}{\mu_{ref}^{warm}}\right)\left[1 - \frac{c_1 c_2 c_3}{c_4}\frac{t^{cold}}{t^{warm}}\right] \tag{2}$$

where $c_1 = (\sigma_g^{cold}/\sigma_g^{warm})^2$, $c_2 = n^{cold}/n^{warm}$, $c_3 = \tilde{v}_d^{cold}/\tilde{v}_d^{warm}$, and $c_4 = H^{cold}/H^{warm}$. With the assumption of identical initial widths of distributions ($c_1 = 1$), dry deposition mechanisms ($c_2 = 1$), dry deposition strengths ($c_3 = 1$), and mixing heights ($c_4 = 1$) equation 2 directly links $\mu_{air}^{cold}/\mu_{air}^{warm}$ with $t^{cold}/t^{warm}$. Figure 6 shows the thus derived

ratios of $t^{cold}/t^{warm}$ as a function of $\mu^{cold}/\mu^{warm}$ due to changes in transport. Since we have only limited knowledge about $\mu_{ref}$, three different values have been applied for $\mu_{air}^{warm}/\mu_{ref}^{warm}$: All are based on $\mu_{air}^{warm} = 1.3\ \mu$m, which is on average our measured mode during Preboreal; $\mu_{ref}^{warm}$ has been taken as 2.5 $\mu$m, 3.2 $\mu$m and 4.0 $\mu$m respectively. 2.5 $\mu$m surely imposes a lower limit on $\mu_{ref}^{warm}$ as this value is found in high Alpine ice cores during Saharan dust events [*Wagenbach and Geis*, 1989]; on the other hand 4.0 $\mu$m diameter may be deduced as an upper limit from [*D'Almeida and Schütz*, 1983]. The intermediate value of 3.2 $\mu$m may therefore give a good estimate for $\mu_{ref}$. In Figure 6 typical ratios of $\mu_{air}^{cold}/\mu_{air}^{warm}$ have been marked for LGM vs. Preboreal and Stadial vs. Interstadial climate changes whereby it is assumed that differences in long range transport account for our observed changes of $\mu$ after a 10 % correction for different deposition scenarios was made. With these assumptions the implied ratio of transit times can be read from Figure 6. A ratio $t^{cold}/t^{warm} \approx 0.75$ is suggested from our model picture for the LGM vs. Preboreal and $t^{cold}/t^{warm} \approx 0.9$ for the Stadial vs. Interstadial comparison. The difference between a cold and a warm state is illustratively sketched in Figure 7.

## Implications from size changes for concentration changes

The evidence we found for the ratio of transit times $t^{cold}/t^{warm}$ imposes limits on the concentration change associated with changed long range transport. The concentration change resulting from different long range transport during cold and warm periods may be written as $\left(\frac{C^{cold}}{C^{warm}}\right) = \frac{f^{cold}}{f^{warm}} \cdot \exp\left(\frac{t^{warm}}{\tau^{warm}}\left(1 - \frac{\tau^{warm}}{\tau^{cold}}\frac{t^{cold}}{t^{warm}}\right)\right)$. To calculate $C^{cold}/C^{warm}$ as a function of $t^{cold}/t^{warm}$ a number of estimates are necessary. For the dilution with particle free air $f \sim 1/s$ is taken where $s$ is the transversal width of the transported dust plume. Supposing $s = \sqrt{D/t}$ and no change of eddy diffusion constants $D$ renders $f^{cold}/f^{warm} = (t^{cold}/t^{warm})^{-1/2}$. The scaling factor $t^{warm}/\tau^{warm}$ can be estimated from equation 1 by taking $\frac{\mu}{\mu_0} = \frac{\mu_{air}^{warm}}{\mu_{ref}^{warm}} \approx \frac{1.3\mu\text{m}}{3.2\mu\text{m}}$, $n = 2$, $\sigma_g = \ln 1.7$, and by assuming $\tilde{v}_d \approx \tilde{v}_w$ during warm climates (i.e. in our picture: equal portions of size fractionating and non-fractionating loss processes); this renders $\frac{t^{warm}}{\tau^{warm}} = 3.2$. Further, the ratio of residence times $\tau^{warm}/\tau^{cold}$ may be estimated by supposing equal mixing heights $H^{cold} = H^{warm}$ and dry depletion velocities $\tilde{v}_d^{cold} = \tilde{v}_d^{warm}$ and by assuming $\tilde{v}_w^{cold} = 0.5\tilde{v}_w^{warm}$ for LGM vs. Preboreal to account for reduced wet depletion en route during LGM; the latter appears a reasonable upper estimate from extrapolating the observed reduction of the accumulation rate to the entire transport path as well as from model calculations of the hydrological cycle [*Andersen and Ditlevsen*, 1998]; this yields $\tau^{warm}/\tau^{cold} = 0.75$.

In Figure 8 the resulting $C^{cold}/C^{warm}$ is shown as a function of $t^{cold}/t^{warm}$ for

two scenarios of $\tau^{warm}/\tau^{cold}$: First, $\tau^{warm}/\tau^{cold} = 1$ is taken for curve (A), which shows $C^{cold}/C^{warm}$ resulting from changed transit times only. For curve (B) also the residence times were varied, which is more realistic; $\tau^{warm}/\tau^{cold} = 1$ is presumed for no change of circulation ($t^{cold}/t^{warm} = 1$) and $\tau^{warm}/\tau^{cold} = 0.75$ for LGM vs. Preboreal changes ($t^{cold}/t^{warm} = 0.75$) with a linear interpolation in between. This gives values for $C^{cold}/C^{warm}$ of $\approx 5$ for LGM vs. Preboreal and $\approx 2$ for a typical D/O transition.

## Summary of model results

Our simple 1-D model picture considers size fractionation during particle deposition and long range transport. We conclude that due to size fractionation during dry deposition the size distribution is shifted towards larger particles in the ice with respect to the air. This shift was larger during cold climates when wet deposition was lower. However, the difference in shift between cold and warm climates may account only for around 3% to 20% of the particle size changes we observe in the ice. Therefore, changes of $\mu$ during different climatic periods predominantly reflect changed airborne size distributions over Greenland.

We find that the size distribution may be influenced strongly by size fractionating depletion processes during long range transport, which lead to a shift towards smaller particles at the deposition site compared to the source. Therefore, shorter transit times during colder climates would lead to larger airborne particles at the ice sheet and could explain the observed mode changes between cold and warm climates. Our model picture only allows for a rough quantitative evaluation of this effect: Demanding that the observed mode change (after a 10% correction due to the deposition effect was made) is solely due to changed long range transport during cold and warm climates implies a change of transit times of $t^{cold}/t^{warm} \approx 0.75$ for LGM vs. Preboreal and $t^{cold}/t^{warm} \approx 0.9$ for D/O changes.

These changes of transit times are associated with changes of airborne concentration at the ice sheet relative to the source. These again can be estimated roughly, which yields a factor $\approx 5$ concentration increase for LGM vs. Preboreal and a factor $\approx 2$ for Stadial vs. Interstadial. Given the observed concentration increase in our data by a factor of 100 from Preboreal to LGM it is evident even from our rough estimate that other processes must have contributed more effectively to the concentration increase than did changes of atmospheric circulation. These other processes may have included source strength intensification through an increased frequency of dust storms, higher surface wind speeds or increased source aridity, as these do not cause a change of the size distribution in our model picture.

From ice cores and from other paleoclimatic archives it has been inferred that atmospheric circulation during the last glacial period substantially differed from present day's, e.g. [*Janecek and Rea*, 1985; *Rea*, 1994; *Kapsner et al.*, 1995; *Lamy et al.*, 1999; *Lagroix and Banerjee*, 2002]; in particular, increased westerly flow has been proposed for both the northern and the southern hemispheres. Higher wind speeds during the LGM are also proposed from modelling exercises. *Andersen and Ditlevsen* [1998] as well as *Tegen and Rind* [2000] calculated the increase of airborne dust concentration due to higher wind speed and a reduced hydrological cycle during the LGM compared to present day and suggest factors of around 2 to 4. The similarity of these values to our estimates supports the hypothesis that a change in transit times not only bares the potential of changing the particle size distribution in polar ice cores but in fact was the controlling mechanism.

## Comparison with other ice core records

Much attention has been given to the question "whether particles were larger during Holocene or LGM". However, this unspecific formulation allows for several confusions. Firstly, the answer depends on the size parameter that is considered because various size parameters behaved differently. In our data set we find instances where, for example, the lognormal mode increases, absolute coarseness stays unchanged, relative coarseness decreases, and the mean volume diameter remains unchanged. Therefore, the size parameter which is considered must always be specified. Secondly, the stated question may be confused with the one "whether particles were larger in conjunction with high or with low particle concentrations"; the necessity for this differentiation has become apparent at least for Antarctica from recent work (see below).

Regarding the dependance of the lognormal mode on the particle concentration, the observations in the Greenlandic Dye3 [*Steffensen*, 1995] and GRIP [*Steffensen*, 1997] ice cores during the last glacial resemble each other closely with respect to both rate of increase as well as absolute level (see Figure 9). In the NGRIP core we find a similar rate of increase, but a lower absolute level, which may be due to methodical or unknown geographical differences. For Antarctica, in early size distribution measurements, *Petit et al.* [1981] and *De Angelis et al.* [1984] did not perform lognormal fits, but an optical inspection of their data suggested increasing modes with increasing concentration, which is sketched in Figure 9. Both find this trend for glacial as well as for Holocene samples. However, new Antarctic data by *Delmonte et al.* [2002] contains increasing modes with increasing concentration only for glacial ice older than the Antarctic Cold

Reversal. Yet unexplained, the opposite behavior is clearly exhibited for younger ice, which may be an important clue for the understanding of past southern hemisphere climate. This opposite behavior leads to the phenomenon that although particle modes increase with concentration in pleistocene ice still they are larger during Holocene than during LGM. This probably had not been observed in the earlier Antarctic work [*Petit et al.*, 1981; *De Angelis et al.*, 1984] due to limited number and non-representative selection of samples. For Greenland there is not enough Holocene data to confirm or exclude such a subdivided behavior. The larger absolute values of $\mu$ in Antarctica compared to Greenland may result from higher contribution of dry deposition due to a lower accumulation rate at the Antarctic sites.

Regarding the relative coarseness, a greater relative abundance of large particles concurrent with high concentrations had been reported for Antarctica [*Petit et al.*, 1981] but a smaller one for Greenland [*Steffensen*, 1997]. However, like *Steffensen* [1997] also *Delmonte et al.* [2002] find less large particles during times of high concentrations. Since this new data due to methodical differences has a higher resolution than that of *Petit et al.* [1981], the disagreement seems to be resolved. Also we find relatively less large particles at high concentrations, so that it seems evident that relative coarseness changed similarly in Greenland and Antarctica. Although findings for Greenland and Antarctica are in accordance at least during the glacial epoch the atmospheric systems transporting dust to the polar ice sheets may have behaved very differently in the northern and southern hemispheres; whereas in Antarctica the abundance of large particles clearly must be driven by atmospheric transport, in Greenland also other causes such as varying contributions of proximal sources or of biological particles may be important.

# Conclusions

This study shows that a laser particle detector can be used for very efficient counting and sizing of windblown mineral microparticles in ice cores. A more than 1500 m long continuous profile is provided covering in 1.65 m resolution almost the complete last glacial period. We find particle concentrations higher by a factor of 100 during LGM than during the Preboreal and concentration changes by typically a factor of 8 at the sharp transitions of D/O-events. The mode $\mu$ of the lognormal size distribution varies systematically with the tendency towards smaller particles during warmer climates. The variability of the mode is higher during warmer climates, and values of the standard deviation $\sigma$ are also increased; the latter results from increased variability of the size

distributions of the events that contribute particles to each multi-year sample.

We base our interpretation of the particle size distribution on a highly simplified, but quantitative model picture. From this we interpret the lognormal mode as indicating atmospheric transit times during long range transport from the source to the ice sheet. Larger modes indicate shorter transit times, which may result from higher mean advection velocities and/or shorter transport routes. Both may be related to the position of the Polar Front. From our data we conclude roughly 25% shorter transit times during LGM than during the Preboreal. As we find that circulation changes alone clearly cannot account for the observed concentration increase by a factor of 100 other processes such as source intensification must have contributed synchronously. This means that climatic situations lead to increased source strength as well as to shorter transit times during cold periods. The clear correlation of processes in the source areas with large scale atmospheric circulation patterns suggests strong mediating mechanisms.

During warm periods a clear tendency towards longer transit times is exhibited. However, transit times were much more variable and occasionally also have been short. It therefore appears that atmospheric regimes providing slower transport were more variable and on the contrary that atmospheric circulation was more confined during cold climates. This may reveal the variability of the Polar Front with respect to the source areas: During cold periods the Polar Front may have always been located far enough south to include the source areas. Whereas during warmer periods the Polar Front may have been located generally further north but was subject to occasional southward excursions.

The variability of transit times during warm periods is – on time scales of up to several 100 years – not connected to variable source strength. This certain degree of independence between dust production processes and long range transport times is observed despite their generally strong linkage. The independence is also evident from occasional timing differences of dust concentration and size distribution parameters at rapid climatic transitions. This underlines that source processes by themselves do not influence the size distribution of particles carried to Greenland. It further suggests that both source processes and long range transport are two independent results from environmental forcings.

Clearly, the interpretation of particle size distributions in ice cores is still limited through our insufficient understanding of size fractionating processes. Sophisticated model calculations for long range transport and particle deposition are needed to check our findings and to draw more differentiated conclusions from the size distribution data. Size distribution measurements at high depth resolution may aid the understanding of rapid climate transitions during the last glacial period. Furthermore, an investigation

of size distributions in Greenland during the Holocene are desirable for a comparison to the newest Antarctic results. As insights on variability, timing and the systematics of changes are benefits from continuous measurements, these should always be preferred over spot-check type investigations.

**Acknowledgements**
The North-GRIP project is directed and organized by the Department of Geophysics at the Niels Bohr Institute for Astronomy, Physics and Geophysics, University of Copenhagen. It is being supported by funding agencies in Denmark(SNF), Belgium (NFSR), France (IFRTP and INSU/CNRS), Germany (AWI), Iceland (RannIs), Japan (MECS), Sweden (SPRS), Switzerland (SNF) and the United States of America (NSF). We wish to thank all the funding bodies and field participants. Matthias Bigler and Regine Röthlisberger are acknowledged for their exceptional dedication in running the CFA-lab in the field. Hubertus Fischer is thanked for his helpful comments to the manuscript.

# References

Andersen, K. K., A. Armengaud, and C. Genthon, Atmospheric dust under glacial and interglacial conditions, *Geophysical Research Letters, 25*(13), 2281–2284, 1998.

Andersen, K. K., and P. D. Ditlevsen, Glacial - interglacial variations of meridional transport and washout of dust: A one-dimensional model, *Journal of Geophysical Research, 103*(D8), 8955–8962, 1998.

Biscaye, P. E., F. E. Grousset, M. Revel, S. Van der Gaast, G. A. Zielinski, A. Vaars, and G. Kukla, Asian provencance of glacial dust (stage 2) in the greenland ice sheet project 2 ice core, summit, greenland, *Journal of Geophysical Research, 102*(C12), 26765–26781, 1997.

Chylek, P., G. Lesins, and U. Lohmann, Enhancement of dust source area during past glacial periods due to changes of the hadley circulation, *Journal of Geophysical Research, 106*(D16), 18,477–18,485, 2001.

Cragin, J. H., M. M. Herron, C. C. J. Langway, and G. Klouda, Interhemisheric comparison of changes in the composition of atmospheric precipitation during the late cenozoic era, in *Polar Oceans*, edited by M. J. Dunbar, pp. pp.617–631, Arct. Inst. of North America, Calgary, AB, Canada, 1977.

D'Almeida, Guillaume, A., and L. Schütz, Number, mass and volume distributions of mineral aerosol and soils of the sahara, *Journal of Climate and Applied Meteorology, 22*, 233–243, 1983.

Davidson, C. I., M. H. Bergin, and H. D. Kuhns, The deposition of particles and gases to ice sheets, in *Chemical Exchange Between the Atmosphere and Polar Snow*, edited by E. W. Wolff and R. C. Beales, pp. 275–306, Springer Verlag, Berlin Heidelberg, 1996.

De Angelis, M., M. Legrand, J. R. Petit, N. I. Barkov, Y. S. Korotkevitch, and V. M. Kotlyakov, Soluble and insoluble impurities along the 950 m deep vostok ice core (antarctica) - climatic implications, *Journal of Atmospheric Chemistry, 1*, 215–239, 1984.

Delmonte, B., J. R. Petit, and V. Maggi, Glacial to Holocene implications of the new 27,000-year dust record from the EPICA Dome C (East Antarctica) ice core., *Climate Dynamics,*, in press, 2002.

Fuchs, N. A., *The machanics of aerosols*, Pergamon Press, Oxford, London, Edinburgh, New York, Paris, Frankfurt, 1964.

Fuhrer, K., E. W. Wolff, and S. J. Johnsen, Timescales for dust variability in the Greenland Ice Core Projct (GRIP) ice core in the last 100,000 years, *Journal of Geophysical Research, 104*(D24), 31043–31052, 1999.

Gillette, D. A., J. Adams, A. Endo, and D. Smith, Threshold velocities for input of soil particles into the air by desert soils, *Journal of Geophysical Research, 85*(C10), 5621–5630, 1980.

Gillette, D. A., I. H. J. Blifford, and D. W. Fryrear, The influence of wind velocity on the size distributions of aerosols generated by the wind erosion of soils, *Journal of Geophysical Research, 79*(27), 4068–4075, 1974.

Grootes, P. M., and M. Stuiver, Oxygen 18/16 variability in Greenland snow and ice with 10-3 - to 10-5 -year time resolution, *Journal of Geophysical Research, 102*(C12), 26,455–26,470, 1997.

Hammer, C. U., H. B. Clausen, W. Dansgaard, A. Neftel, P. Kristinsdottir, and E. Johnson, Continuous impurity analysis along the dye 3 deep core, in *Greenland Ice Core: Geophysics, Geochemistry, and the Environment*, edited by C. C. J. Langway, H. Oeschger, and W. Dansgaard (Eds.), Volume 33 of *Geophysical Monograph 33*, pp. 90–94, American Geophysical Union, Washington, 1985.

Hansson, M. E., The Renland ice core. A Nothern hemisphere record of aerosol composition over 120'000 years, *Tellus, 46B*, 390–418, 1994.

Janecek, T. R., and D. K. Rea, Quaternary fluctuations in the northern hemisphere trade winds and westerlies, *Quaternary Reasearch, 24*, 150–163, 1985.

Johnsen, S. J., H. B. Clausen, W. Dansgaard, N. S. Gundestrup, C. U. Hammer, U. Andersen, K. K. Andersen, C. S. Hvidberg, D. Dahl-Jensen, J. P. Steffensen, H. Shoji, A. E. Sveinbjrnsdttir, J. W. C. White, J. Jouzel, and D. Fisher, The $\delta^{18}$O record along the Greenland Ice Core Project deep ice core and the problem of possible eemian climatic instability, *Journal of Geophysical Research, 102*(C12), 26397–26410, 1997.

Junge, C. E., Processes responsible for the trace content in precipitation, in *Isotopes and Impurities in Ice and Snow*, IAHS-AISH publication no. 118, Grenoble, 1977.

Kahl, J. D. W., D. A. Martinez, H. Kuhns, C. I. Davidson, J.-L. Jaffrezo, and J. M. Harris, Air mass trajectories to summit, greenland: A 44-year climatology and some episodic events, *Journal of Geophysical Research, 102*(C12), 26,861–26,875, 1997.

Kapsner, W. R., R. B. Alley, C. A. Shuman, S. Anandakrishnan, and P. M. Grootes, Dominant influence of atmospheric circulation on snow accumulation in greenland over the past 18,000 years, *Nature, 373*, 52–54, 1995.

Krinner, G., and C. Genthon, GCM simulations of the Last Glacial Maximum surface climate of Greenland and Antarctica, *Climate Dynamics, 14*, 741–758, 1998.

Lagroix, F., and S. K. Banerjee, Paleowind directions from the magnetic fabric of loess profiles in central alaska, *Earth and Planetary Science Letters, 195*, 99–112, 2002.

Lamy, F., D. Hebbeln, and G. Wefer, High-resolution marine records of climatic change in mid-latitude chile during the last 28,000 years based on terrigenous sediment parameters, *Quaternary Research, 51*, 83–93, 1999.

Mahowald, N., K. Kohfeld, M. Hansson, Y. Balkanski, S. P. Harrison, I. C. Prentice, M. Schulz, and H. Rodhe, Dust sources and deposition during the last glacial maximum and current climate: A comparison of model results with paleodata from ice cores and marine sediments, *Journal of Geophysical Research, 104*(D13), 15895–15916, 1999.

Petit, J.-R., M. Briat, and A. Royer, Ice age aerosol content from east antarctic ice core samples and past wind strenght, *Nature, 293*, 391–394, 1981.

Petit, J. R., L. Mounier, J. Jouzel, Y. S. Korotkevich, V. I. Kotlyakov, and C. Lorius, Palaeoclimatological and chronological implications of the vostok core dust record, *Nature, 343*, 56–58, 1990.

Porter, S. C., and A. Zhisheng, Correlation between climate events in the north atlantic and china during the last glaciation, *Nature, 375*, 305–308, 1995.

Pye, K., *Aeolian dust and dust deposits*, Academic Press, London, 1987.

Rea, D. K., The paleoclimatic record provided by eolian deposition in the deep sea: The geologic history of wind, *Reviews of Geophysics, 32*(2), 159–195, 1994.

Röthlisberger, R., M. Bigler, A. Hutterli, S. Sommer, B. Stauffer, H. G. Junghans, and D. Wagenbach, Technique for continious high-resolution analysis of trace substances in firn and ice cores, *Environmental Science Technology, 34*, 338–342, 2000.

Royer, A., M. De Angelis, and J. R. Petit, A 30000 year record of physical and optical properties of microparticles from an east antarctic ice core and implications for paleoclimate reconstruction models, *Climate Change, 4*, 381–412, 1983.

Ruth, U., D. Wagenbach, M. Bigler, J. P. Steffensen, and R. Röthlisberger, High resolution dust profiles at NGRIP: Case studies of the calcium-dust relationship, *Annals of Glaciology, 35*, in press, 2002.

Saey, P., 1998, *Concentration and size distribution of microparticles in Alpine and polar ice cores (in German)*, M.sc. thesis, University of Heidelberg.

Sehmel, G. A., Particle and gas dry deposition: A review, *Atmospheric Enviroment, 14*, 983–1011, 1980.

Steffensen, J. P., 1995, *Microparticles and chemical impurities in ice cores from Dye 3, South Greenland and their interpretation in palaeoclimatic reconstructions*, Ph.d. thesis, University of Copenhagen.

Steffensen, J. P., The size distribution of microparticles from selected segments of the greenland ice core project ice core representing different climatic periods, *Journal of Geophysical Research, 102*(C12), 26,755–26,763, 1997.

Sugimae, A., Elemental constituents of atmospheric particulates and particle density, *Nature, 307*, 145–147, 1984.

Svensson, A., P. E. Biscaye, and F. E. Grousset, Characterization of late glacial continental dust in the greenland ice core projct ice core, *Journal of Geophysical Research, 105*(D24), 4637–4656, 2000.

Tegen, I., and I. Fung, Modeling of mineral dust in the atmosphere: Sources, transport, and optical thickness, *Journal of Geophysical Research, 99*(D11), 22897–22914, 1994.

Tegen, I., and D. Rind, Influence of the latitudinal temperature gradient on soil dust concentration and deposition in greenland, *Journal of Geophysical Research, 105*(D6), 7199–7212, 2000.

Unnerstad, L., and M. Hansson, Simulated airborne particle size distributions over greenland during last glacial maximum, *Geophysical Research Letters, 28*(2), 287–290, 2001.

Wagenbach, D., and K. Geis, The mineral dust record in a high altitude Alpine glacier (Colle Gnifetti, Swiss Alps), in *Paleoclimatology and Paleometeorology: Modern and Past Patterns of Global Atmospheric Transprot*, edited by M. Leinen and Sarnthein, pp. 543–564, Kluwer, 1989.

Wang, Y. J., H. Cheng, R. L. Edwards, Z. S. An, J. Y. Wu, C.-C. Shen, and J. A. DOrale, A high-resolution absolute-dated late pleistocene monsoon record from hulu cave, china, *Science, 294*(2345-2348), 2345–2348, 2001.

Werner, M., U. Mikolajewicz, M. Heimann, and G. Hoffmann, Borehole versus isotope temperatures on greenland: Seasonality does matter, *Geophysical Research Letters, 27*(5), 723–726, 2000.

Wurzler, S., T. G. Reisin, and Z. Levin, Modification of mineral dust particles by cloud processing and subsequent effects on drop size distributions, *Journal of Geophysical Research, 105*(D4), 4501–4512, 2000.

Zielinski, G. A., Paleoenvironmental implications of the insolubable microparticle record in the GISP2 ( Greenland) ice core during the rapidly changing climate of the Pleistocene-Holocene transition, *Geological Society of America Bulletin, 109*(5), 547–559, 1997.

# Figures

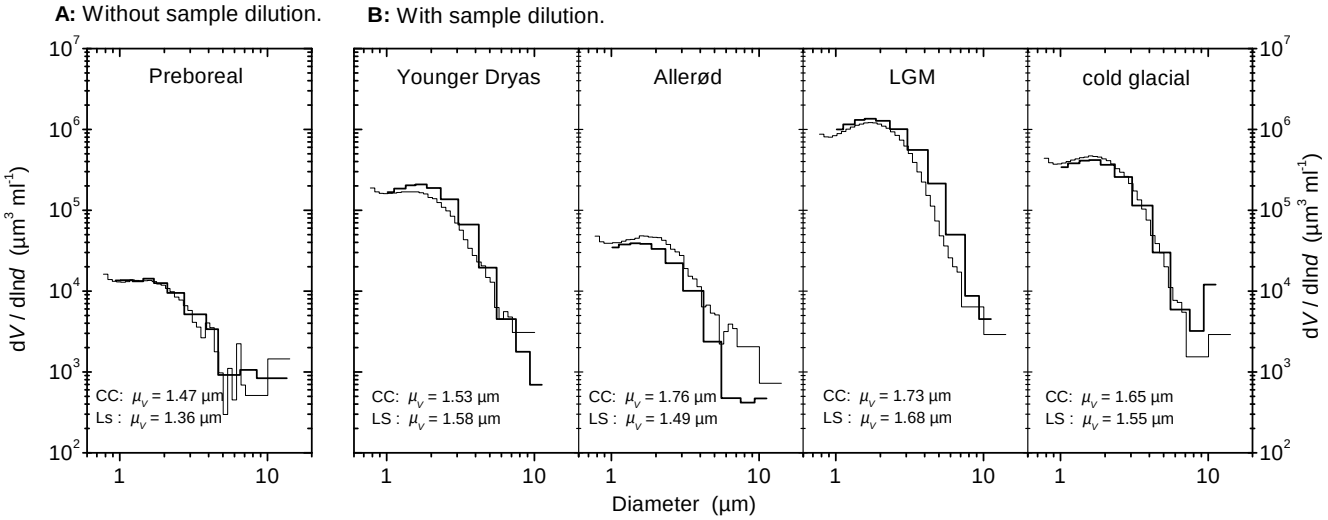


Figure 1: Size distributions by volume used for calibration. Coulter Counter (CC) data in thin lines, laser sensor (LS) data in bold lines. The laser sensor data is shown after the adjustment of its size axis. The rise at the left end of the Coulter Counter curves is due to baseline noise as the lower size limit is reached. Listed is also the lognormal mode $\mu$ of the distributions as derived from CC and LS data. Measurements without sample dilution were calibrated using the Preboreal horizon (A); measurements with sample dilution were calibrated using the other four horizons (B).

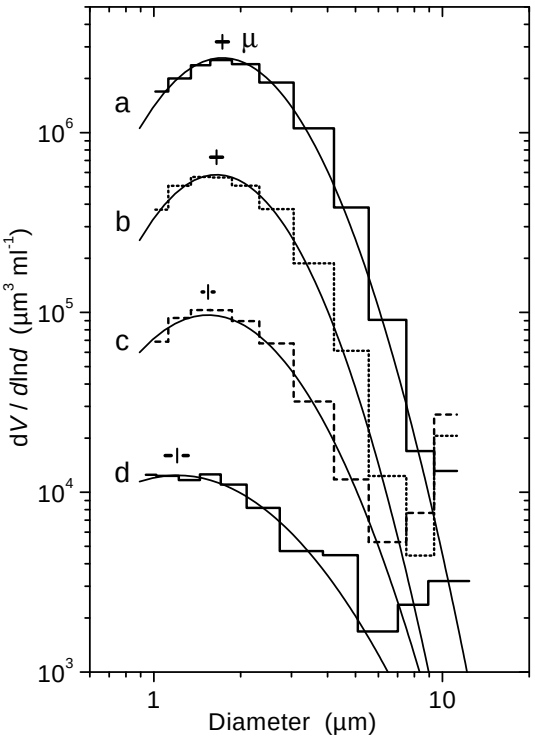


Figure 2: Individual size distributions by volume from different climatic periods along with lognormal fits. a: 1831.50 - 1833.15 m (LGM); b: 2075.70 - 2077.35 m (S9); c: 2121.90 - 2123.55 m (IS10); d: 1460.25 - 1461.90 m(Preboreal). Indicated is the position of the mode $\mu$ and the uncertainty of the fit.

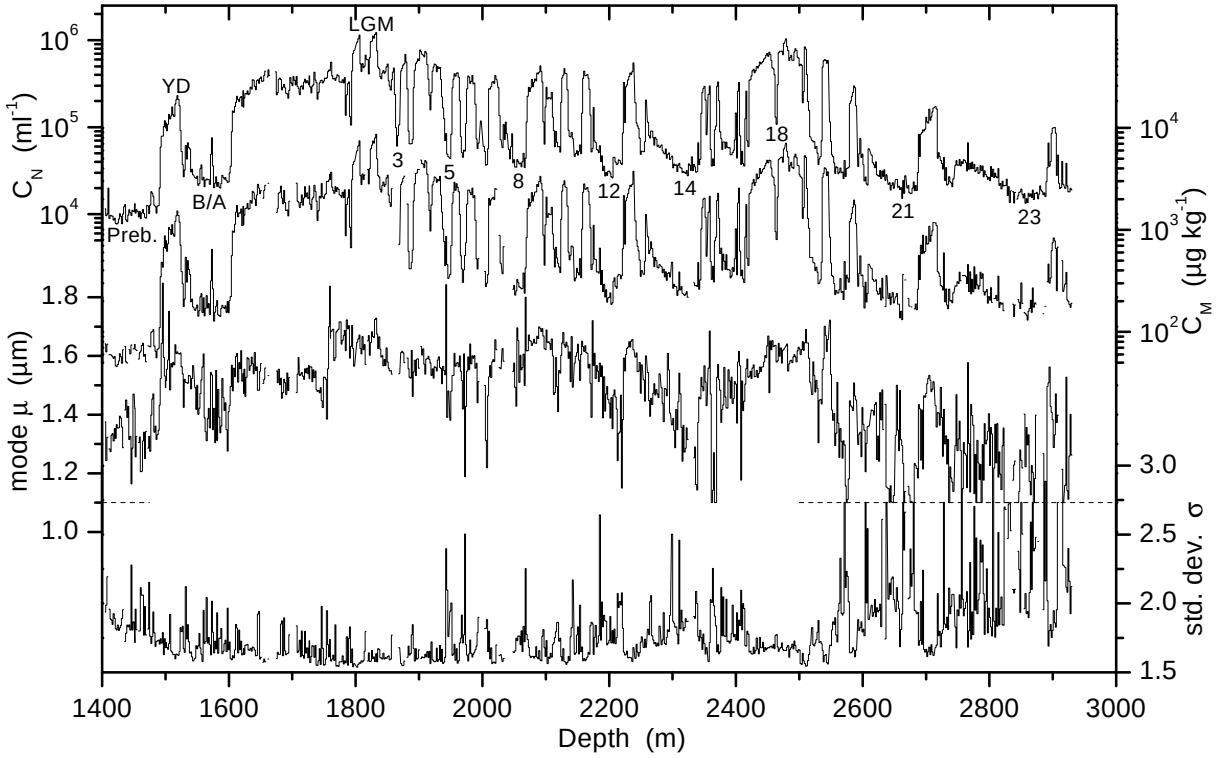


Figure 3: Profiles of microparticle concentration and lognormal size distribution parameters $\mu$ (diameter) and $\sigma$. Number concentration is based on counts of particles larger 1.0 $\mu$m. Gaps arise either from missing data or from data that did not allow for a proper lognormal fit. Selected climatic periods are labeled: Preb = Preboreal Holocene, YD = Younger Dryas, B/A = Bølling/Allerød, LGM = Last Glacial Maximum; numbers refer to Dansgaard/Oeschger-events. The data of the bottom two panels was truncated at the dashed line indicated.

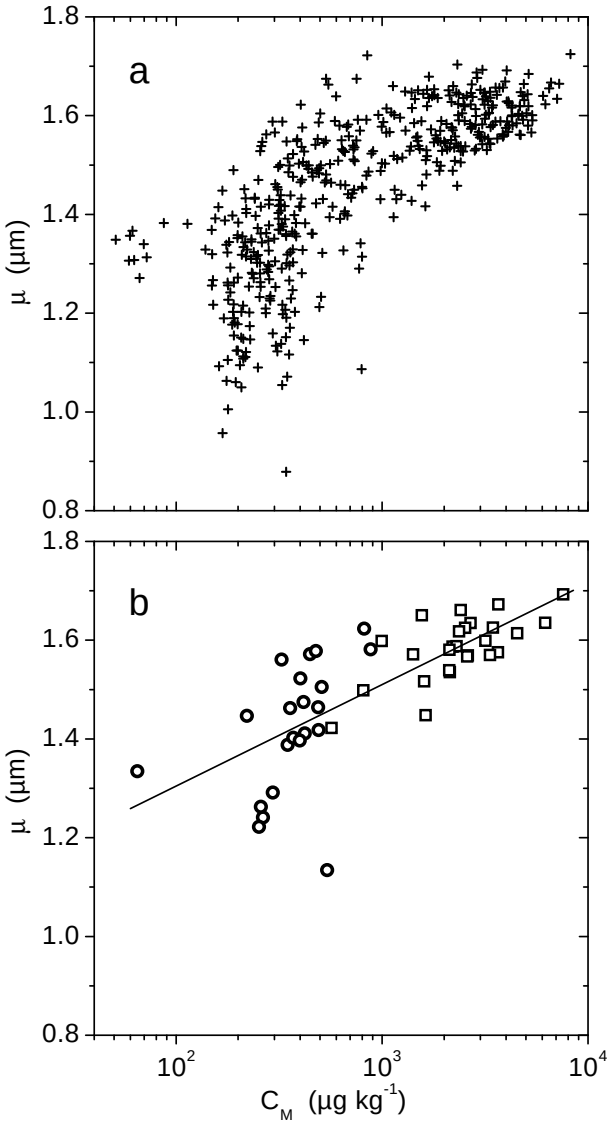


Figure 4: Correlation of the mode $\mu$ and the mass concentration $C_M$. a: All data has been averaged such that each data point represents 200 years. b: All data has been averaged over climatic periods; circles denote warm periods, squares denote cold periods. A logarithmic trend line is also shown.

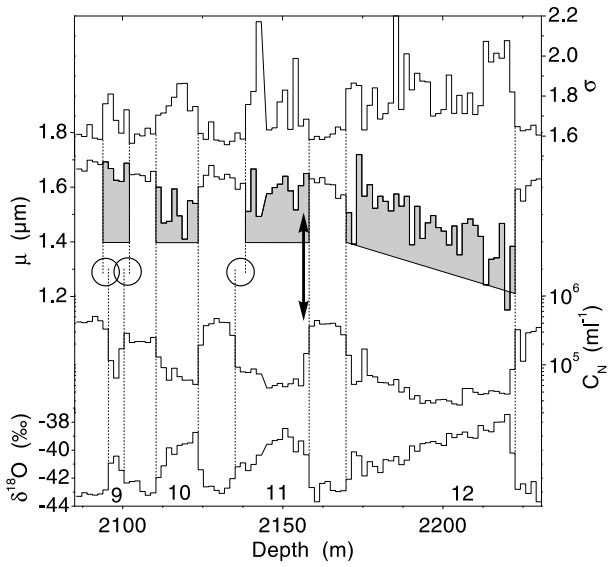


Figure 5: Detail from profiles showing various rapid D/O-transitions. Shown are size distribution parameters $\sigma$ and $\mu$ number concentration $C_N$, and $\delta^{18}$O (data is personal communication from NGRIP-members). Shaded areas emphasize interstadials in the profile of the mode. Circles mark instances where the timing of a transition may be inferred differently from $\mu$ and $\sigma$ or respectively from $V_N$ and $\delta^{18}$O. The arrow points to a transition where $\mu$ seemingly shows other timing than $\sigma$. Numbers in the bottom panel indicate interstadials.

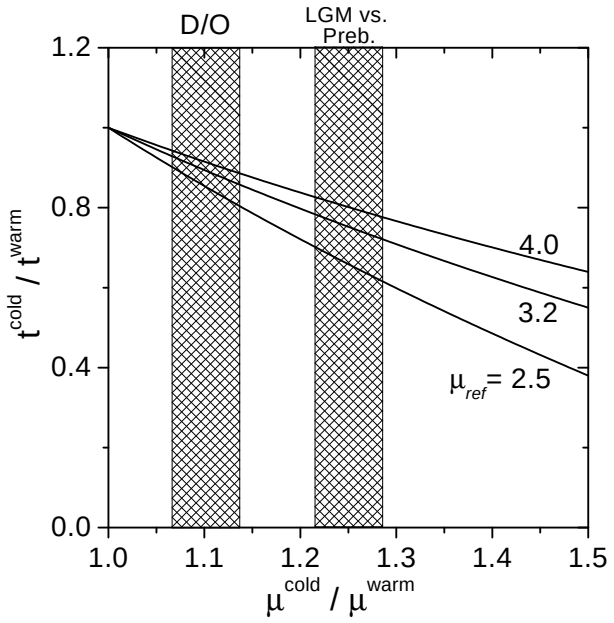


Figure 6: Implications for the change in transit times $t^{cold}/t^{warm}$ from observed size changes $\mu^{cold}/\mu^{warm}$. Curves consider different scenarios for $\mu_{ref}$. Shaded areas mark LGM vs. Preboreal and Stadial vs. Interstadial (D/O) changes, respectively.

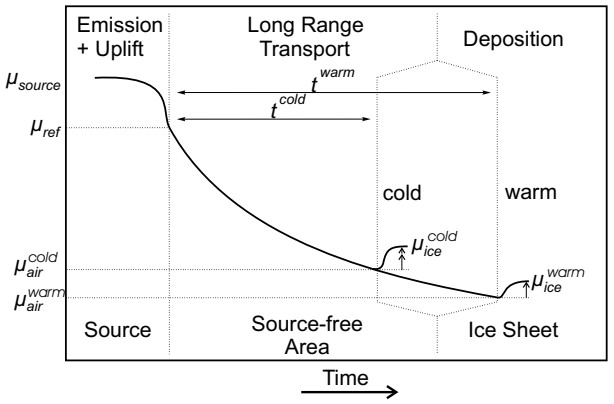


Figure 7: Schematic illustration to the model picture. The airborne particle size distribution with mode $\mu_{source}$ at the source is changed rapidly during uplift until $\mu_{ref}$ is reached. Here, per definition, long range transport across source-free areas starts. During long range transport the mode decreases slowly owing to size fractionating depletion processes. Because the transit time $t$ during cold climates is shorter than during warm climates the mode $\mu_{air}$ of airborne particles at the ice sheet is larger during cold climates. During deposition the mode is shifted slightly towards larger particles leading to $\mu_{ice}$. Upper indices '*cold*' and '*warm*' denote cold and warm climatic states, respectively.

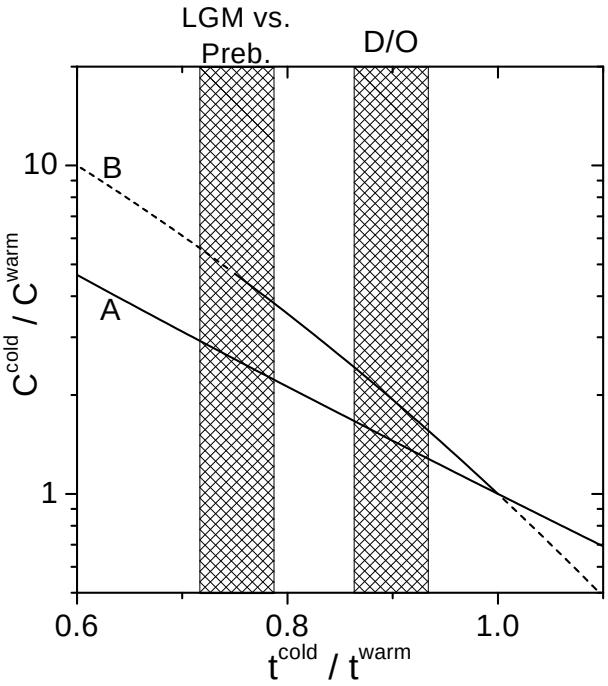


Figure 8: $C^{cold}/C^{warm}$ as a function of $t^{cold}/t^{warm}$ for two scenarios of $\tau^{warm}/\tau^{warm}$. (A): no change of residence times; (B): reduction of wet removal during LGM as described in the text; extrapolations are dashed. Shaded areas mark probable values for $t^{cold}/t^{warm}$ for LGM vs. Preboreal and D/O transitions as inferred from Figure 6.

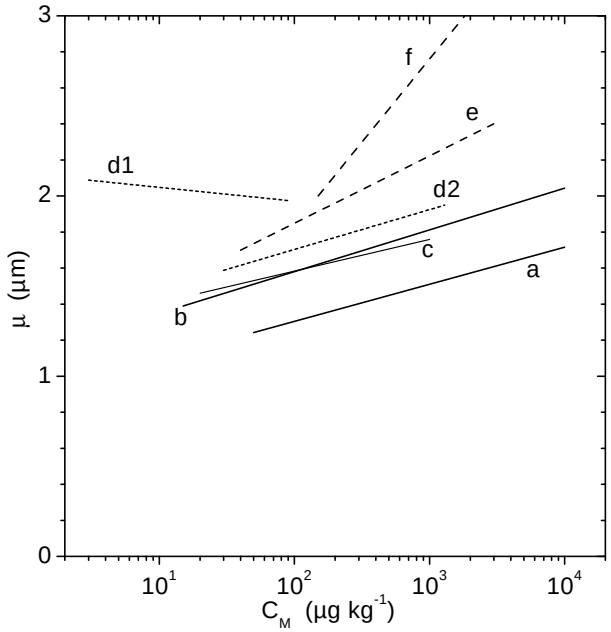


Figure 9: Correlation of $C_M$ and $\mu$ in different ice cores from Greenland (solid lines) and from Antarctica (broken lines). a: NGRIP, this work; b: GRIP [*Steffensen*, 1997]; c: Dye3 [*Steffensen*, 1995]; d1: EPICA Dome-C, Holocene data until mid-transition including Antarctic Cold Reversal (ACR) [*Delmonte et al.*, 2002]; d2: EPICA Dome-C, glacial data starting mid-transition excluding ACR) [*Delmonte et al.*, 2002]; e: Dome-C (Holocene and glacial samples) [*Petit et al.*, 1981]; f: Vostock (Holocene and glacial samples) [*De Angelis et al.*, 1984]. For (e) and (f) mass concentrations were inferred from the number concentrations reported using a conversion deduced from [*Delmonte et al.*, 2002].

# Chapter 6

# Nitrate in Greenland and Antarctic ice cores: a detailed description of post-depositional processes

Regine Röthlisberger, Manuel A. Hutterli, Cric W. Wolff, Robert Mulvaney, Hubertus Fischer, Matthias Bigler, Kumiko Goto-Azuma, Margareta E. Hansson, Urs Ruth, Marie-Louise Siggaard-Andersen, and Jørgen P. Steffensen

*Annals of Glaciology*, Volume 35 (2002), in press

# Nitrate in Greenland and Antarctic ice cores: a detailed description of post-depositional processes

Regine Röthlisberger[1,2], Manuel A. Hutterli[3], Eric W. Wolff[2], Robert Mulvaney[2], Hubertus Fischer[4], Matthias Bigler[1], Kumiko Goto-Azuma[5], Margareta E. Hansson[6], Urs Ruth[4,7], Marie-Louise Siggaard-Andersen[8], Jørgen P. Steffensen[8]

*Submitted to the International Glaciological Society for the International Symposium on Ice Cores and Climate, Kangerlussuaq, Greenland*

*Manuscript No. 35A053*

*Submitted June 2001, revised September 2001*

[1]Climate and Environmental Physics, Bern, Switzerland
[2]British Antarctic Survey, Cambridge, England
[3]Dept. of Hydrology and Water Resources, Tucson, USA
[4]Alfred Wegener Institute, Bremerhaven, Germany
[5]National Institute of Polar Research, Tokyo, Japan
[6]Dept. of Physical Geography and Quaternary Geology, Stockholm, Sweden
[7]Institut für Umweltphysik, Heidelberg, Germany
[8]Dept. of Geophysics, Copenhagen, Denmark

# Abstract

A compilation of nitrate ($NO_3^-$) data from Greenland has shown that recent $NO_3^-$ concentrations show a temperature-dependence similar to the one seen in Antarctica. Except for sites with very low accumulation rates, lower temperatures tend to lead to higher $NO_3^-$ concentrations preserved in the ice. Accumulation rate, which is closely linked to temperature, might influence the concentrations preserved in snow as well, but its effect cannot be separated from the temperature imprint. Processes involved in $NO_3^-$ deposition are discussed and shown to be temperature- and/or accumulation rate-dependent. Apart from scavenging of nitric acid ($HNO_3$) during formation of precipitation, uptake of $HNO_3$ onto the ice crystal's surface during and after precipitation seems to contribute further to the $NO_3^-$ concentrations found in surface snow. Post-depositional loss of $NO_3^-$ from the top snow layers is caused by release of $HNO_3$ and by photolysis of $NO_3^-$. It is suggested that photolysis accounts for considerable losses at sites with very low accumulation rates. Depending on the site characteristic, and given that the temperature- and accumulation rate-dependence is quantified, it should be possible to infer changes in atmospheric $HNO_3$ concentrations.


# Introduction

The nitrate ($NO_3^-$) record in polar ice cores is expected to contain information about past atmospheric concentrations of nitrogen oxides ($NO_x$ = NO + $NO_2$) due to the close link of $NO_3^-$ and $NO_x$. The increase in atmospheric $NO_x$ concentrations in the northern hemisphere caused by rising fossil fuel combustion since approximately 1940, for example, is reflected in higher $NO_3^-$ concentrations in Greenland snow [*Neftel and others*, 1985]. However, past studies have shown that factors other than atmospheric $NO_x$ concentrations influence $NO_3^-$ records as well [*Wolff*, 1995]. In Greenland as well as in Antarctica, reversible deposition of $NO_3^-$ and net losses in the top snow layers have been observed. It has been suggested that either re-evaporation of nitric acid ($HNO_3$) [*Mulvaney and others*, 1998; *Dibb and others*, 1998; *Röthlisberger and others*, 2000b] or photolysis of $NO_3^-$ in the top few centimeters of the snowpack [*Honrath and others*, 2000; *Jones and others*, 2000] cause such post-depositional alterations.

In earlier studies, relationships between $NO_3^-$ and accumulation rate have been proposed [*Herron*, 1982; *Legrand and Kirchner*, 1990; *Yang and others*, 1995], with generally higher accumulation rates associated with lower $NO_3^-$ concentrations and higher $NO_3^-$ depositional fluxes. In a more recent study based on a macroscopic deposition model, *Fischer and others* [1998] found a second-order polynomial dependence

of average firn concentration and inverse snow accumulation.

Based on a compilation of $NO_3^-$ data from more than 50 Antarctic sites covering various temperature and accumulation regimes, it has recently been suggested that temperature is also a key parameter in defining $NO_3^-$ concentrations in Antarctic snow and ice, with lower temperatures leading to higher $NO_3^-$ concentrations preserved in the snow [*Röthlisberger and others*, 2000b]. Elevation has also been linked to $NO_3^-$ concentrations, both for Greenland and Antarctica [*Yang and others*, 1996; *Mulvaney and Wolff*, 1994], but no statistically significant relationship has been found in a more recent study [*Kreutz and Mayewski*, 1999]. The inherent connection between temperature, accumulation rate and elevation makes it difficult to distinguish between the separate effects and thus no firm conclusions about their relative importance have so far been reached.

Here, we give a detailed description of the processes involved in $NO_3^-$ re-emission and a discussion of how temperature and accumulation rate affect those processes. In analogy to the compilation of $NO_3^-$ data from Antarctic sites, $NO_3^-$ data from many Greenland sites have been gathered in order to illustrate the effect of temperature. Also, we outline how calcium ($Ca^{2+}$) can inhibit $NO_3^-$ re-emission.

Another aspect that has been discussed lately dealt with the effect of snow layers containing large amounts of sulfuric acid ($H_2SO_4$) of volcanic origin on $NO_3^-$ concentrations. Most studies focused on a few well known volcanic eruptions during the Holocene which showed post-depositional displacement of $NO_3^-$ away from the $H_2SO_4$ peak. This behaviour has been found in single events in Greenland and Antarctica [*Clausen and others*, 1997; *Legrand and Kirchner*, 1990; *Röthlisberger and others*, 2000b]. However, the mechanisms leading to this effect are only vaguely understood and hypotheses have not been tested on a large number of cases, because of a lack of sufficient high-resolution data.

In this paper, new high-resolution data from the NGRIP (North Greenland Ice Core Project) ice core are used to investigate the effect of volcanic $H_2SO_4$ on $NO_3^-$ in more detail. Volcanic events from the early Holocene, the Last Glacial Maximum (LGM) and some earlier glacial periods are compared and a hypothesis of the mechanism is given.

# Data

Many of the $NO_3^-$ data used in this paper are compiled from earlier studies (see Table 1 for references). Furthermore, data from selected sections of the NGRIP ice core

(75.1°N, 42.05°W, 2978 m above sea level) are presented. These sections were analyzed during the NGRIP 2000 field season with a continuous flow analysis (CFA) system, as described in *Röthlisberger and others* [2000a]. Among other compounds, nitrate ($NO_3^-$), sulphate ($SO_4^{2-}$), and calcium ($Ca^{2+}$) have been measured at a resolution of approximately 1 cm.

## $NO_3^-$ – temperature – accumulation rate

In Fig. 1 average $NO_3^-$ concentrations for different Greenland locations are indicated. In order to account for the anthropogenic increase in $NO_3^-$ concentrations in Greenland, the data have been split into two separate sets, one indicating concentrations from before 1940, which are unaffected by the anthropogenic emissions, and one from after 1970. The data and the appropriate references are listed in Table 1. For both pre-1940 and post-1970, a decreasing trend in $NO_3^-$ concentration with increasing temperature is found (Fig. 2). A similar trend has been found in Antarctica [*Röthlisberger and others*, 2000b], where also generally higher concentrations are found at sites with lower temperatures, except for very low accumulation sites such as for example Dome C. At Dome C, the concentrations in the top few centimeters can be very high (up to 1000 ppb), but at greater depths, only 15 ppb are preserved, despite the low temperatures (annual mean temperature $\approx -54^\circ$ C).

If $NO_3^-$ concentrations are plotted against accumulation rate, higher $NO_3^-$ concentrations are found at sites with lower accumulation rates (Fig. 3), but again, $NO_3^-$ concentrations at very low accumulation sites do not agree with the general trend. Considering the close relationship between temperature and accumulation rate (Fig. 4), it seems difficult to separate the effect of temperature and accumulation rate on $NO_3^-$ concentrations. Only a detailed consideration of the underlying microphysical processes allows for assigning a temperature or accumulation rate dependence.

In the following discussion, we analyse the temperature and accumulation rate dependence of processes involved in $NO_3^-$ deposition and re-emission, aiming for a better understanding of:

- the cause of the relationship between $NO_3^-$ concentrations and mean annual temperature and accumulation rate at a site
- the generally higher $NO_3^-$ levels in summer snow than in winter snow
- the net loss of $NO_3^-$ from snow after deposition

$NO_3^-$ can either be predominantly incorporated in the bulk or adsorbed to the surface of a snow crystal, depending on the deposition pathway. In a cloud with a liquid water content of more than 0.01 $g\,m^{-3}$ and pH > 1, $HNO_3$ would be completely dissolved in water droplets due to its high solubility, leaving virtually no $HNO_3$ in the gas-phase [*Seinfeld and Pandis*, 1998]. Thus, in the case of liquid or mixed clouds, essentially all $HNO_3$ is removed from the gas-phase independent of the cloud temperature. While there is no specific information about the conditions at cloud level, typical liquid water contents of 0.1 $g\,m^{-3}$ and initial $HNO_3$ concentrations of 20 pptv in the air would lead to $NO_3^-$ concentrations of approximately 350 ppbw in fresh snow. On the other hand, the co-condensation of $HNO_3$ and water ($H_2O$) molecules on ice crystals [*Thibert and Dominé*, 1998] would lead to a bulk concentration of 20 ppbw only. In the absence of liquid water, i.e. in ice clouds, the high $NO_3^-$ concentrations found in surface snow could not be explained. However, *Abbatt* [1997] observed a temperature-dependence of adsorption of $HNO_3$ on ice surfaces with higher uptake at lower temperatures. For typical summer temperatures at South Pole (246 K, data obtained from http://www.cmdl.noaa.gov), the uptake capacity on fresh snow crystals exceeds the amount of $HNO_3$ available in the cloud, implying that at very cold temperatures where ice clouds predominate, essentially all $HNO_3$ in a cloud is bound to the surface of the snow crystal. While co-condensation, riming, and adsorption of $HNO_3$ determine the distribution of $NO_3^-$ within the ice crystal, its concentration is defined by the initial atmospheric concentration of $HNO_3$ and the amount of condensed water in the cloud. An imprint of temperature is expected for surface uptake and co-condensation, but not for the $HNO_3$ taken up in liquid cloud droplets. Based on the results of *Abbatt* [1997], the snow crystals are expected to efficiently scavenge atmospheric $HNO_3$ on their way to the surface, potentially further increasing the $NO_3^-$ concentration of the fresh snow.

Once on the ground, the formation of surface hoar frost (co-condensation), rime (deposition of supercooled fog droplets) as well as dry deposition (adsorption of $HNO_3$ onto the crystal's surface) leads to additional $NO_3^-$ deposition to surface snow. For a given atmospheric $HNO_3$ concentration, the hoar frost $NO_3^-$ concentration is determined by the water vapour concentration [*Thibert and Dominé*, 1998], which is mainly a function of temperature T. Assuming that the relative humidity at the site is similar throughout the year, the $NO_3^-$ concentration should depend linearly on 1/T in a first order approach. However, if assuming that the $HNO_3$ concentrations in the atmosphere as in Table 2 are representative for the site, the estimated concentrations resulting from co-condensation are lower than observed surface snow concentrations, thus leading to dilution of the surface snow (Table 2). Rime deposition on the other hand, which is likely to remove all $HNO_3$ from the air, shows similar concentrations to fresh snow, pro-

vided that the atmospheric $HNO_3$ concentration is similar to the one at cloud level. A net dry deposition of $HNO_3$ (adsorption of $HNO_3$ onto snow crystals) has the potential to increase the $NO_3^-$ concentration in snow. However, it will only contribute where the surface is undersaturated, i.e. at very cold sites and during winter. The contribution in winter is small, due to low atmospheric $HNO_3$ concentrations. During the summer, the contribution of dry deposition to the $NO_3^-$ concentrations in snow at South Pole might be considerable. However, according to *Hauglustaine and others* [1994], the dry deposition velocity of 0.5 $cm\,s^{-1}$ for $HNO_3$ on snow has to be considered as an upper limit. At sites with higher accumulation rates, a specific surface snow layer is buried more rapidly, leaving less time to adsorb additional $HNO_3$ from the atmosphere, given that no saturation has been reached. Therefore, a tendency for higher concentrations at lower accumulation rates is expected.

Besides the diluting effect of co-deposition, processes capable of reducing the $NO_3^-$ concentration in snow are desorption of $HNO_3$ from the snow crystal [*Mulvaney and others*, 1998; *Dibb and others*, 1998; *Röthlisberger and others*, 2000b] and photolysis [*Honrath and others*, 2000; *Jones and others*, 2000]. In both cases, the $NO_3^-$ ion has to be at the surface of a snow crystal, since photolysis of $NO_3^-$ in the bulk is not effective [*Dubowski and others*, 2001]. If a $NO_3^-$ ion recombines with a $H^+$ ion to form $HNO_3$, it then may desorb into the firn air and eventually diffuse into the air above the snow. Diffusion of $NO_3^-$ in ice has been investigated by *Thibert and Dominé* [1998], who found that diffusion of $NO_3^-$ in ice is slower at colder temperatures with the diffusion coefficient D given by $D = 1.37 \times 10^{-2610/T} cm^2 s^{-1}$ with $T$ being the temperature in K. During the summer, the typical time a $NO_3^-$ molecule needs to reach the ice surface (diffusion length of 40$\mu$m, corresponding to an average crystal radius [*Harder and others*, 1996]) is of the order of a couple of hours (e.g. Neumayer) to a few days (e.g. South Pole).

The solubility of $NO_3^-$ in ice has been determined for various temperatures [*Thibert and Dominé*, 1998]. For summer conditions, not only the surface snow but also deeper layers are supersaturated with respect to the solubility of $NO_3^-$ in ice (Table 2). In the case of South Pole, the surface remains undersaturated, suggesting that $NO_3^-$ that is expelled from the bulk is simply transferred to the surface without affecting the $NO_3^-$ concentration. At warmer sites (e.g. Neumayer or Summit), the ice surface also might become supersaturated during the summer, leading to release of $HNO_3$ from the snow into the interstitial air. From a thermodynamic point of view, warmer temperatures during the summer should facilitate the release of $HNO_3$ from the ice surface. But according to the uptake experiment of *Abbatt* [1997], only up to 25% of the $HNO_3$ that has been taken up are released again afterwards. However, the emphasis of his study

was laid on the uptake rather than the release of $HNO_3$ and a temperature-dependence of the release has not been discussed. Once released from the snow crystal's surface, the $HNO_3$ molecule might make its way out of the snowpack, leading to a net loss of $NO_3^-$ in the snow. The molecular diffusion of $HNO_3$ in the interstitial air is temperature dependent as well, but probably this is not the limiting factor controlling the transfer out of the snowpack. It is conceivable that temperature-dependent, repeated adsorption and subsequent desorption of a $HNO_3$ molecule on ice crystals will determine the removal from the snowpack.

Photolysis of $NO_3^-$ in the top snow layers results in the production of nitrogen dioxide ($NO_2$) and hydroxyl radical (OH). $NO_2$ is not expected to interact with the surrounding snow but to be mixed into the boundary layer rather quickly, leading to a $NO_3^-$ depletion in surface snow. The influence is presumably largest at low accumulation sites, where surface snow is exposed to sunlight for a long time. Furthermore, photolysis should become more efficient at lower latitudes due to more incoming UV radiation. At Dome C, the top few centimeters of snow seem to reach saturated surface coverage (concentrations in the range of several 100 ppbw) [*Röthlisberger and others*, 2000b]. Deeper layer are then dramatically undersaturated considering surface coverage and solubility in the bulk. No quantitative estimate of how much $NO_3^-$ can be lost by photolysis has been made so far. It therefore remains unclear whether photolysis alone can account for the $NO_3^-$ profile seen in the snow at Dome C. The estimate of the maximum surface uptake relies very much on the surface area in snow and might change due to recrystallization, which has not yet been taken into account.

Although elevation may affect the atmospheric $HNO_3$ concentration, there is no obvious mechanism by which it can have a direct physical influence on post-depositional processes. A minor influence is expected on the photolysis rate due to changes in the irradiance with altitude and on the gas-phase diffusion due to lower pressure, but both effects might only slightly modulate the changes in $NO_3^-$ concentrations.

## Interactions of $NO_3^-$ with dust

Recent studies have reported that $NO_3^-$ and $Ca^{2+}$ concentrations are correlated in ice from the last glacial period from Vostok and Dome C [*Legrand and others*, 1999; *Röthlisberger and others*, 2000b]. During the last glacial period, the $Ca^{2+}$ deposited on the east Antarctic plateau is mainly of terrestrial origin and can thus be used as a proxy for dust. It has been suggested that the reaction of $HNO_3$ and $CaCO_3$ to form $Ca(NO_3)_2$ prevents $NO_3^-$ from being released from the snow into the gas-phase.

In principle, the reaction could take place in the atmosphere or in the snow. For it to happen in the atmosphere, high dust concentrations would need to be in the same season as the maximum nitrate concentrations. A recent paper that studied the reaction of $CaCO_3$ with $HNO_3$ derived a formula for the lifetime for removal of $HNO_3$ by dust [*Hanisch and Crowley*, 2001]. Based on this, and using very rough estimates for the surface area of dust (assuming spherical particles of 1 $\mu$m diameter, a typical density of 2 g cm$^{-3}$, and atmospheric dust concentrations of 10 ng m$^{-3}$), we can estimate an $HNO_3$ lifetime versus removal by dust in the present day Antarctic atmosphere of around 50 days. This is unlikely to be important relative to other removal processes. However, this could be reduced to 2 days under the dustier conditions of the LGM, and in Greenland under LGM conditions one could estimate a lifetime for this removal of only a few hours. It seems possible therefore that under LGM conditions, much of the atmospheric $HNO_3$ could be converted to aerosol calcium nitrate in the atmosphere. In addition, the reaction to form $Ca(NO_3)_2$ might take place in the snow, in which case $HNO_3$ has to make its way to the snow layer where the $Ca^{2+}$ has been deposited and, if $Ca^{2+}$ is inside the snow grain rather than on its surface, diffuse through it.

## Influence of volcanic $H_2SO_4$ on $NO_3^-$

As shown lately in an Antarctic high-resolution record from Dome C [*Röthlisberger and others*, 2000b], $H_2SO_4$ of volcanic origin can cause $NO_3^-$ to move in the ice. Several examples of very low $NO_3^-$ concentrations coinciding with $H_2SO_4$ peaks and increased $NO_3^-$ concentrations above and below this layer have been found in the Dome C as well as the NGRIP record (Fig. 5a). At Dome C, the effect is first seen at 12 m depth, where the deposits of the Tambora eruption (1815 A.D.) are located. This indicates that the processes involved take place or at least start in the firn.

Our hypothesis of the mechanism for $NO_3^-$ displacement in the firn relies on similar processes as described above, as it includes diffusion of $HNO_3$ in the firn air. The high concentration of $H_2SO_4$ in a volcanic layer causes the equilibrium of $H^+ + NO_3^- \rightleftharpoons HNO_3$ to shift towards the right hand side, as a large amount of $H^+$ from the $H_2SO_4$ is present. Therefore, a locally elevated concentration of $HNO_3$ in the firn air is caused, which prompts gas-phase diffusion of the $HNO_3$ away from the volcanic layer towards either side. In adjacent layer with no excessive $H_2SO_4$, $HNO_3$ favours dissociation into $H^+$ and $NO_3^-$, thus maintaining the gradient in the firn air by removing $HNO_3$ from the gas-phase. It is possible that the movement of $NO_3^-$ progresses via a different mechanism in the ice after pore close-off, possibly by diffusion of ions in the veins.

Fig. 5b shows an event where no $NO_3^-$ displacement occurred. In this section, large amounts of alkaline material are present in the ice, as seen by the high $Ca^{2+}$ and negligible $H^+$ concentrations. In the context of the above hypothesis, the high concentrations of alkaline material (presumably $CaCO_3$) neutralize the $H_2SO_4$ and prevent the formation of $HNO_3$. The assumption that in this case $H_2SO_4$ undergoes some reactions is supported by the significantly narrower $SO_4^{2-}$ peak compared to the ones seen in acid ice (P. Barnes, pers. communication).

Our hypothesis is challenged by the example shown in Fig. 5c. Although a lot of excess $H_2SO_4$ is present and far too little $Ca^{2+}$ to compensate, no marked $NO_3^-$ displacement is seen. It is possible that the $Ca^{2+}$ was unable to neutralize the $H_2SO_4$, but that it managed to bind $NO_3^-$ thus preventing it from being transferred into the gas-phase. The occurrence of ice layers limiting $HNO_3$ diffusion in the interstitial air is rather unlikely in NGRIP.

# Conclusions

The spatial distribution of nitrate concentrations in Greenland is shown to be strongly related to site temperature, just as it is for Antarctica. Because temperature and snow accumulation rate are so closely linked, we cannot determine which of these factors is the one exerting physical control on the concentrations seen. In either case, the relationship changes at the very lowest accumulation rates, where it is clear that post-depositional losses are the dominant control on the sub-surface concentration.

By examining the individual processes that could contribute to the nitrate concentration in snow, we find that many of them are indeed temperature-dependent, with higher concentrations predicted at lower temperatures, as observed. Some processes could also depend on the accumulation rate, if a longer exposure time at the surface allows additional uptake. Of the processes identified, either uptake by liquid droplets in cloud, if present, or uptake onto the ice surface in the cloud or after deposition can lead to concentrations in fresh snow that are as high or higher than those observed. However, the role of surface uptake at higher temperatures, as encountered in coastal Antarctica and in Greenland in summer, needs to be quantified. Co-condensation of nitric acid and water, and dissolution of nitric acid within the ice lattice appear to give concentrations that are too low compared to those observed. This suggests tentatively that surface uptake and retention might be rather important in determining the concentrations we see. This process has a temperature dependence (approximately threefold greater uptake at $-55°C$ compared to $-25°C$ [*Abbatt*, 1997]) similar to that

seen in Fig. 2. However, according to *Abbatt* [1997], the uptake is not dependent on the nitric acid concentration in air. The higher nitrate concentrations in post-1970 Greenland snow compared to pre-1940 snow suggests that the snow concentration is somehow related to atmospheric concentrations, and we suggest that this is simply a question of limited supply to the ice surface, because nitric acid is scavenged so efficiently. In that case, a temperature- and accumulation rate-corrected Holocene nitrate ice core record of a site with adequate snow accumulation rate should reflect the flux of nitrate to the surface, which should in turn be related to atmospheric $NO_x$ input.

For sites with very low accumulation rate, losses, possibly due to photolysis, control the concentration seen in the Holocene in such a dominant way that it is unlikely that information about atmospheric nitrate or $NO_x$ can be extracted. Once the ice becomes less acidic (in the last glacial period), the concentration of nitrate seems to be strongly controlled by the calcium or dust content of the atmosphere, and the deposition processes might be significantly altered. The ratio of nitrate to dust might give clues to the past nitrate content of the atmosphere, although in this case it is probable that the nitrate uptake is determined by the content of the atmosphere over the whole transport route of dust from its source to the deposition site, and is not closely related to the local nitrate concentration at the ice core site.

A number of laboratory and field experiments would help to test the above hypotheses. Laboratory uptake experiments, similar to those carried out at 248 K and below [*Abbatt*, 1997], are needed at higher temperatures, appropriate to summer temperatures at coastal Antarctic or Greenland sites. Laboratory experiments would also allow an assessment of whether photolysis can account for the magnitude of nitrate losses at low accumulation sites. Field measurements of the nitric acid content of the atmosphere are lacking for most sites, and particularly for winter. Experiments that follow the evolution of concentration from fresh snow to depth in individual layers are also required.

In summary, the factors that control nitrate concentration in ice cores are complex, and interpretation is likely to involve different factors for different locations and time periods. However, if the factors controlling deposition and loss can be better understood, it may still be possible, in some cases, to reconstruct information about the important $NO_x$ cycle in the past.

**Acknowledgements** This work was supported by a fellowship of the Swiss National Science Foundation. We thank Henrik B. Clausen and Lars B. Larsen for providing unpublished nitrate data. Thanks to NGRIP participants and supporters as well as its funding agencies.

# References

Abbatt, J. P. D., Interaction of $HNO_3$ with water-ice surfaces at temperatures of the free troposphere, *Geophys. Res. Let., 24*(12), 1479–1482, 1997.

Bigler, M., 2000, Entwicklung und Anwendung einer neuen Methode zur kontinuierlichen, hochaufgelösten Messung der Sulfatkonzentration an alpinen und polaren Eisbohrkernen, Master's thesis, University of Bern, Bern, Switzerland.

Clausen, H. B., C. U. Hammer, C. S. Hvidberg, D. Dahl-Jensen, J. P. Steffensen, J. Kipfstuhl, and M. Legrand, A comparison of the volcanic records over the past 4000 years from the Greenland Ice Core Project and Dye 3 Greenland ice cores, *J. Geophys. Res., 102*(C12), 26707–26723, 1997.

Clausen, H. B., and C. C. Langway, The ionic deposits in polar ice cores, in *The Environmental Record in Glaciers and Ice Sheets*, edited by H. Oeschger and C. C. Langway, pp. 225–247, Wiley, New York, 1989.

Dibb, J. E., R. W. Talbot, and M. H. Bergin, Soluble acidic species in air and snow at Summit, Greenland, *Geophys. Res. Let., 21*(15), 1627–1630, 1994.

Dibb, J. E., R. W. Talbot, J. W. Munger, D. J. Jacob, and S. M. Fan, Air-snow exchange of $HNO_3$ and $NO_y$ at Summit, Greenland, *J. Geophys. Res., 103*(D3), 3475–3486, 1998.

Dubowski, V., A. J. Colussi, and M. R. Hoffmann, Nitrogen Dioxide Release in the 302 nm Band Photolysis of Spray-Frozen Aqueous Nitrate Solutions. Atmospheric Implications, *J. Phys. Chem. A, 105*(20), 4928–4932, 2001.

Fischer, H., and D. Wagenbach, Large-scale spatial trends in recent firn chemistry along an east-west transect through central Greenland, *Atm. Env., 30*(19), 3227–3238, 1996.

Fischer, H., D. Wagenbach, and J. Kipfstuhl, Sulfate and nitrate firn concentrations on the Greenland ice sheet 1. Large-scale geographical deposition changes, *J. Geophys. Res., 103*(D17), 21927–21934, 1998.

Hanisch, F., and J. N. Crowley, Heterogeneous Reactivity of Gaseous Nitric Acid on $Al_2O_3$, $CaCO_3$, and Atmospheric Dust Samples: A Knudsen Cell Study, *J. Phys. Chem. A, 105*(13), 3096–3106, 2001.

Hansson, M. E., The Renland ice core. A Northern hemisphere record of aerosol composition over 120'000 years, *Tellus, 46 B*, 390–418, 1994.

Harder, S. L., S. G. Warren, R. J. Charlson, and D. S. Covert, Filtering of air through snow as a mechanism for aerosol deposition to the Antarctic ice sheet, *J. Geophys. Res., 101*(D13), 18729–18743, 1996.

Hauglustaine, D. A., C. Granier, G. P. Brasseur, and G. Mégie, The importance of atmospheric chemistry in the calculation of radiative forcing on the climate system, *J. Geophys. Res., 99*(D1), 1173–1184, 1994.

Hausbrand, R., 1998, Direktmessung der Azidität in einem Eisbohrkern aus Nordwestgrönland, Master's thesis, University of Heidelberg, Heidelberg, Germany.

Herron, M. H., Impurity sources of $F^-$, $Cl^-$, $NO_3^-$, and $SO_4^{2-}$ in Greenland and Antractic precipitation, *J. Geophys. Res., 87*(C4), 3052–3060, 1982.

Honrath, R. E., S. Guo, M. C. Peterson, M. P. Dziobak, J. E. Dibb, and M. A. Arsenault, Photochemical production of gas phase $NO_x$ from ice crystal $NO_3^-$, *J. Geophys. Res., 105*(D19), 24183–24190, 2000.

Jones, A. E., R. Weller, A. Minikin, E. W. Wolff, W. T. Sturges, H. P. McIntyre, S. R. Leonard, O. Schrems, and S. Bauguitte, Oxidized nitrogen chemistry and speciation in the Antarctic troposphere, *J. Geophys. Res., 104*(D17), 21355–21366, 1999.

Jones, A. E., R. Weller, E. W. Wolff, and H. W. Jacobi, Speciation and Rate of Photochemical NO and $NO_2$ Production in Antarctic Snow, *Geophys. Res. Let., 27*(3), 345–348, 2000.

Kreutz, K. J., and P. A. Mayewski, Spatial variability of Antarctic surface snow glaciochemistry: implications for palaeoatmospheric circulation reconstructions, *Antarctic Science, 11*(1), 105–118, 1999.

Legrand, M., and S. Kirchner, Origins and variations of nitrate in South Polar precipitation, *J. Geophys. Res., 95*(D4), 3493–3507, 1990.

Legrand, M., E. Wolff, and D. Wagenbach, Antarctic aerosol and snow fall chemistry: Implications for deep Antarctic ice core chemistry, *Annals of Glaciology, 29*, 66–72, 1999.

Mayewski, P. A., W. B. Lyons, M. J. Spencer, M. S. Twickler, C. F. Buck, and S. Whitlow, An ice-core record of atmospheric response to anthropogenic sulphate and nitrate, *Nature, 346*, 554–556, 1990.

Mulvaney, R., D. Wagenbach, and E. W. Wolff, Postdepositional change in snowpack nitrate from observation of year-round near-surface snow in coastal Antarctica, *J. Geophys. Res., 103*(D9), 11021–11031, 1998.

Mulvaney, R., and E. W. Wolff, Spatial variability of the major chemistry of the Antarctic ice sheet, *Annals of Glaciology, 20*, 440–447, 1994.

Narita, H., Specific surface of deposited snow ii, *Low Temp. Sci. A29*, 69–81, 1971.

Neftel, A., J. Beer, H. Oeschger, F. Zürcher, and R. C. Finkel, Sulphate and nitrate concentrations in snow from South Greenland 1895-1978, *Nature, 314*, 611–613, 1985.

Röthlisberger, R., M. Bigler, M. Hutterli, S. Sommer, B. Stauffer, H. G. Junghans, and D. Wagenbach, Technique for continuous high-resolution analysis of trace substances in firn and ice cores, *Environ. Sci. Techn., 34*, 338–342, 2000a.

Röthlisberger, R., M. A. Hutterli, S. Sommer, E. W. Wolff, and R. Mulvaney, Factors controlling nitrate in ice cores: Evidence from the Dome C deep ice core, *J. Geophys. Res., 105*(D16), 20565–20572, 2000b.

Seinfeld, J. H., and S. N. Pandis, *Atmospheric Chemistry and Physics*, Wiley, New York, 1998.

Steffensen, J. P., Analysis of the seasonal variation in dust, Cl, $NO_3$, and $SO_4$ in two Central Greenland firn cores, *Annals of Glaciology, 10*, 171–177, 1988.

Steffensen, J. P., H. B. Clausen, and J. M. Christensen, On the spatial variability of impurity content and stable isotopic composition in recent summit snow, in *Chemical Exchange Between the Atmosphere and Polar Snow*, edited by E. W. Wolff and R. C. Bales, Volume I 43 of *NATO ASI*, pp. 607–615, Springer Verlag, Berlin Heidelberg, 1996.

Thibert, E., and F. Dominé, Thermodynamics and Kinetics of the Solid Solution of $HNO_3$ in Ice, *J. Phys. Chem. B, 102*, 4432–4439, 1998.

Wolff, E. W., Nitrate in polar ice, in *Ice Core Studies of Global Biogeochemical Cycles*, edited by R. J. Delmas, Volume I 30 of *NATO ASI*, pp. 195 – 224, Springer, Berlin, 1995.

Yang, Q., P. A. Mayewski, E. Linder, S. Whitlow, and M. Twickler, Chemical species spatial distribution and relationship to elevation and snow accumulation rate over the Greenland Ice Sheet, *J. Geophys. Res., 101*(D13), 18629–18637, 1996.

Yang, Q., P. A. Mayewski, S. Whitlow, M. Twickler, M. Morrison, R. Talbot, J. Dibb, and E. Linder, Global perspective of nitrate flux in ice cores, *J. Geophys. Res., 100*(D3), 5113–5121, 1995.

| Site and Ref. | Lat. °N | Long. °W | Altitude m | Temp. °C | Acc. g cm$^{-2}$ a$^{-1}$ | $NO_3^-$ pre-1940 ppb | # years | $NO_3^-$ post-1970 ppb | # years |
|---|---|---|---|---|---|---|---|---|---|
| 1988-8[1] | 64.6 | 43.7 | 2550 | -19.9 | 57 | | | 94 | 2 |
| 1988-7[1] | 64.8 | 44.1 | 2745 | -22.0 | 38 | | | 90 | 3 |
| Dye 3 18C[2], 20D[3] | 65.0 | 44.9 | 2617 | -22.3 | 41 | 53,55 | 174[a],30[c] | 100,122, 132 | 15,5, 15 |
| Dye 3 [2,4] | 65.2 | 43.8 | 2491 | -20.0 | 49 | 44,52, 52 | 10[b],11[b], 220[h] | 86,114 137 | 6,7, 2 |
| 1988-4[1] | 66.6 | 45.5 | 2130 | -18.6 | 30 | | | 117 | 2 |
| 1988-5[1] | 67.0 | 44.5 | 2250 | -20.3 | 33 | | | 115 | 4 |
| 1988-6[1] | 67.2 | 43.8 | 2450 | -21.6 | 36 | | | 108 | 6 |
| EGIG T05[5] | 69.9 | 47.3 | 1910 | -18.0 | 46 | | | 118 | 5 |
| EGIG T09[5] | 70.0 | 46.3 | 2170 | -20.0 | 41 | | | 134 | 9 |
| EGIG T13[5] | 70.2 | 45.0 | 2380 | -22.6 | 46 | | | 107 | 8 |
| Milcent[2] | 70.3 | 44.6 | 2410 | -22.0 | 49 | 61 | 7[g] | | |
| EGIG T17[5] | 70.4 | 44.1 | 2530 | -23.8 | 44 | | | 117 | 9 |
| EGIG T21[5] | 70.6 | 43.0 | 2700 | -24.8 | 44 | | | 112 | 9 |
| Site A[2,6] | 70.6 | 35.8 | 3092 | -29.4 | 29 | 45,64, 70 | 3[d],2[c], 19[b] | | |
| Site D[6] | 70.6 | 39.6 | 3018 | -28.3 | 34 | 73 | 19[b] | | |
| EGIG T27[5] | 70.8 | 41.6 | 2870 | -26.6 | 39 | | | 113 | 9 |
| EGIG T31[5] | 70.9 | 40.6 | 2970 | -27.5 | 34 | | | 133 | 10 |
| EGIG T41[5] | 71.1 | 37.9 | 3150 | -29.5 | 25 | | | 144 | 12 |
| Crete[2] | 71.1 | 37.3 | 3172 | -30.0 | 28 | 60,80 | 60[e],2[g] | | |
| EGIG T43[5] | 71.1 | 37.3 | 3172 | -30.1 | 23 | | | 144,146 | 8,14 |
| EGIG T47[5] | 71.2 | 36.0 | 3099 | -29.9 | 22 | | | 143 | 8 |
| Renland[7,8] | 71.3 | 26.7 | 2340 | -18.0 | 42 | 64,88 | 5[g],9[c] | | 2 |
| EGIG T53[5] | 71.4 | 32.5 | 2864 | -28.0 | 23 | | | 134 | 9 |
| 1987-2[1] | 71.6 | 38.1 | 3157 | -30.4 | 25 | | | 128 | 5 |
| EGIG NST08[5] | 71.9 | 37.8 | 3220 | -31.0 | 23 | | | 153 | 5 |
| 1987-3[1] | 71.9 | 39.8 | 3145 | -30.3 | 30 | | | 123 | 2 |
| 1987-5[1] | 72.0 | 37.5 | 3187 | -31.5 | 22 | | | 130 | 6 |
| EGIG T61[5] | 72.2 | 32.3 | 2812 | -28.8 | 19 | | | 144 | 8 |
| 1987-1[1] | 72.3 | 37.9 | 3170 | -31.3 | 22 | | | 124 | 10 |
| 1987-4[1] | 72.4 | 40.2 | 3146 | -31.5 | 27 | | | 130 | 5 |
| GISP2 ATM[1] | 72.4 | 38.8 | 3200 | -32.0 | 24 | | | 120,130, 135,138 | 3,5, 9,3 |
| EGIG T66[5] | 72.5 | 30.8 | 2678 | -25.7 | 17 | | | 159 | 6 |
| GISP2[1,9,10] | 72.6 | 38.5 | 3200 | -31.0 | 22 | 61,70 | 410[a],650[a] | 108,125, 126,135, 136,149 149,167 | 30,7, 3,6, 6,2, 2,4 |
| GRIP[5,11,12] | 72.6 | 37.6 | 3232 | -31.6 | 20 | 68 | 30[c] | 130,138, 142 | 5,9, 21 |
| 1987-7[1] | 72.6 | 35.9 | 3190 | -33.1 | 18 | | | 157 | 8 |
| 1990-2[1] | 72.8 | 36.5 | 3200 | -33.8 | 17 | | | 136 | 1 |
| 1987-6[1] | 73.0 | 37.7 | 3224 | -33.8 | 17 | | | 148 | 8 |
| NGT01[13] | 73.0 | 37.7 | 3223 | -34.3 | 16 | | | 143 | 13 |
| NGT03 B16[13] | 73.9 | 37.6 | 3040 | -34.6 | 12 | 85 | 40[a] | 132 | 23 |
| North Central[2] | 74.6 | 39.6 | 2930 | -32.0 | 13 | 83,112 | 9[f],21[b] | 164 | 5 |
| NGT05[13] | 74.9 | 37.6 | 2873 | -35.3 | 11 | | | 189 | 12 |
| NGRIP[8,14] | 75.1 | 42.1 | 2978 | -30.9 | 17 | 81 | 156[a] | 149,161 | 5,11 |
| NGT12[13] | 75.7 | 36.4 | 2671 | -34.2 | 10 | | | 161 | 14 |
| NGT14 B18[13] | 76.6 | 36.4 | 2508 | -35.0 | 10 | 73 | 40[a] | 128 | 23 |
| C. Century[2] | 77.2 | 61.1 | 1880 | -24.4 | 35 | 46,65, 71 | 10[g],13[d], 100[h] | 120 | 2 |
| 1988-1[1] | 77.2 | 60.7 | 1650 | -24.6 | 29 | | | 101 | 7 |
| 1988-2,3[1] | 77.2 | 59.2 | 1700 | -23.7 | 31 | | | 96,107 | 4,2 |
| C. Century II[2] | 77.2 | 60.8 | 1910 | -24.7 | 35 | 52 | 13[b] | | |
| NGT37 B26[15] | 77.3 | 49.2 | 2598 | -30.0 | 18 | 69 | 440[a] | 110 | 24 |
| NGT18[13] | 77.5 | 36.4 | 2319 | -32.6 | 11 | | | 158 | 14 |
| NGT23 B20[16] | 78.8 | 36.5 | 2147 | -31.5 | 10 | 83 | 1130[a] | 155 | 24 |
| NGT27 B21[13] | 80.0 | 41.1 | 2185 | -29.6 | 11 | 80 | 40[a] | 126 | 24 |
| Hans Tausen[8] | 80.5 | 37.5 | 1271 | -21.0 | 10 | 74 | 30[c] | 91 | 3 |

References

[1] [*Yang and others*, 1996], data obtained from http://nsidc.org
[2] [*Clausen and Langway*, 1989]
[3] [*Mayewski and others*, 1990]
[4] [*Neftel and others*, 1985]
[5] [*Fischer and Wagenbach*, 1996]
[6] [*Steffensen*, 1988]
[7] [*Hansson*, 1994]
[8] H. B. Clausen, pers. communication
[9] [*Yang and others*, 1995]
[10] University of Arizona, unpublished data
[11] [*Clausen and others*, 1997]
[12] [*Steffensen and others*, 1996]
[13] [*Fischer and others*, 1998]
[14] L. B. Larsen, pers. communication
[15] [*Hausbrand*, 1998]
[16] [*Bigler*, 2000]

Time period

[a] continuous record up to 1940
[b] 20th century, before 1940
[c] 19th century
[d] 18th century
[e] 11 to 18th century
[f] 15th century
[g] 13th century
[h] Holocene

Table 1: Temperature, accumulation rate and $NO_3^-$ concentration for Greenland locations used in this study. # years stands for the number of years covered by the data.

| | Summit | | Neumayer | | South Pole | |
|---|---|---|---|---|---|---|
| | Summer | Winter | Summer | Winter | Summer | Winter |
| Pressure (Pa) | 67000 | | 99000 | | 68000 | |
| Acc. rate ($g\,cm^{-2}\,a^{-1}$) | 20 | | 34 | | 8.5 | |
| Temperature (K) | 259 | 230 | 269 | 247 | 246 | 208 |
| Relative Humidity | 0.75 | 0.75 | 0.8 | 0.8 | 0.75 | 0.6 |
| $HNO_3$ atm. (pptv) | 20 | 1 | 6 | 1 | 20 | 1 |
| $NO_3^-$ snow (ppbw) | 120 | | 50 | | 100 | |
| Co-Condensation (ppbw) | 7 | 9 | 1 | 2 | 26 | 160 |
| Solubility in ice (ppbw) | 19 | 29 | 8 | 12 | 40 | 150 |
| Surface uptake (ppbw) | | 1900 | | 780 | 840 | 3300 |
| Dry deposition (ppbw) | 30 | 2 | 8 | 1 | 77 | 5 |

Table 2: Estimates of $NO_3^-$ concentrations in snow due to different deposition mechanisms. The meteorological data are from automatic weather stations, the atmospheric $HNO_3$ summer concentrations are from *Dibb and others* [1994] and *Jones and others* [1999]. For South Pole, atmospheric concentrations of the same order of magnitude as in Summit have been assumed. The $HNO_3$ winter concentration has only been measured at Neumayer and has been found to be approximately 1 pptv (R. Weller, personal communication). In the absence of measurements for the other sites, we assume the winter concentrations at Summit and South Pole to be the same as in Neumayer. The calculations for co-condensation and solubility in ice are based on *Thibert and Dominé* [1998]. Surface uptake was estimated using a linear regression through the values for temperature-dependent uptake found by *Abbatt* [1997] and assuming a typical surface area of 4000 $m^2\,m^{-3}$ [*Narita*, 1971]. Temperatures higher than 248 K have not been included in the study of surface uptake, therefore the estimates for surface uptake in Summit and Neumayer during summer are missing. Dry deposition was calculated assuming a dry deposition velocity of 0.5 $cm\,s^{-1}$ [*Hauglustaine and others*, 1994].

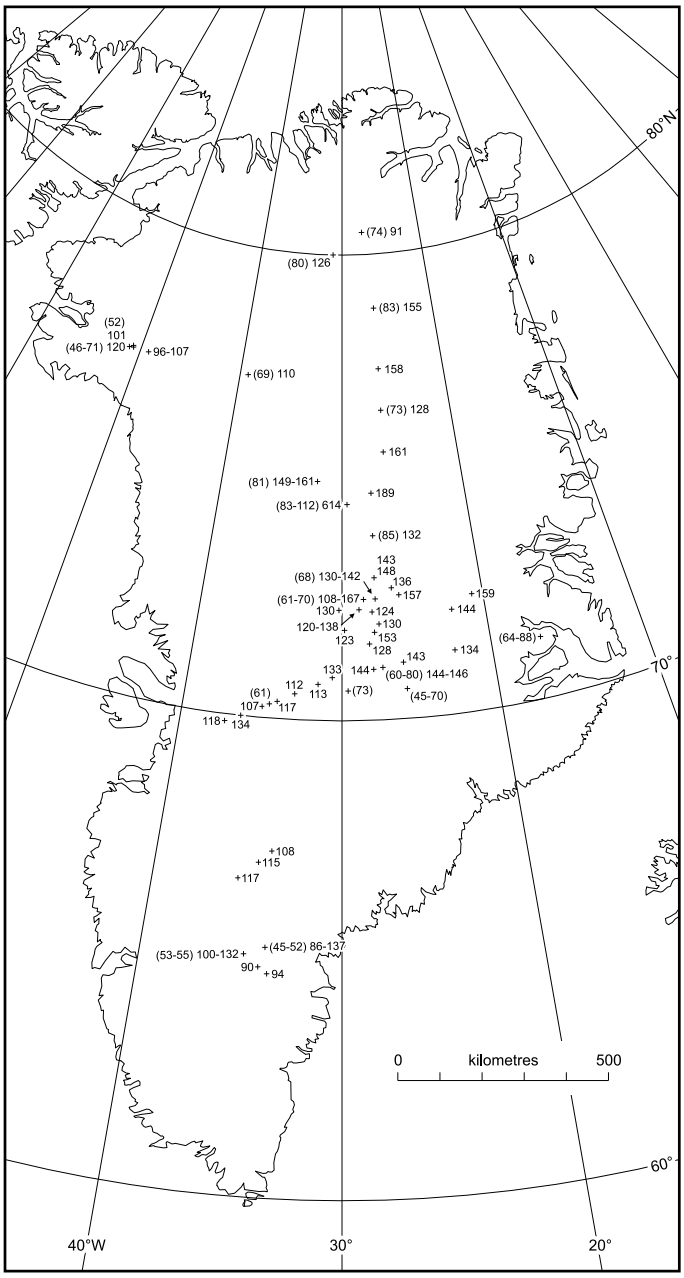


Figure 1: Spatial distribution of $NO_3^-$ across Greenland. Concentrations in snow deposited before 1940 are shown in parentheses, the other values correspond to concentrations in snow deposited after 1970. All concentrations are in ppb.

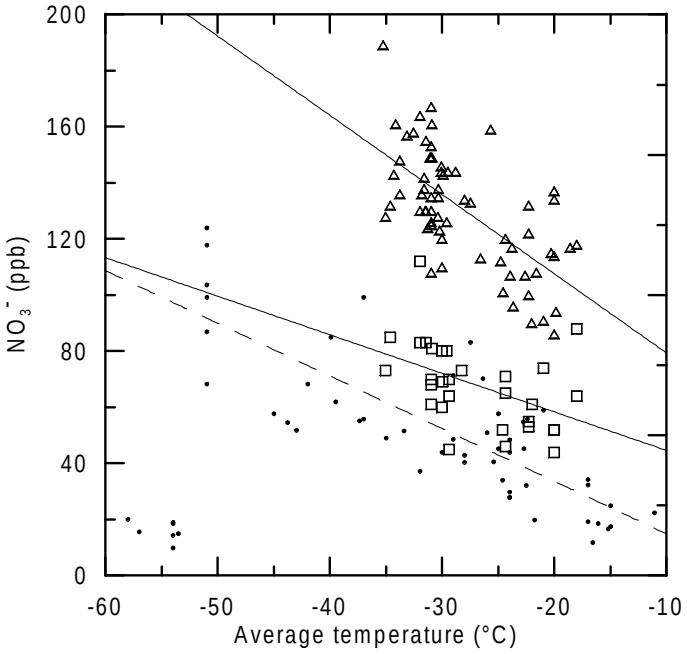


Figure 2: $NO_3^-$ concentrations versus average temperatures in Greenland and Antarctica with linear trends (triangles (post-1970), squares (pre-1940) and the solid lines: Greenland; dots and dashed line: Antarctica). The data points at temperatures below -52° C correspond to sites with very low accumulation rates and are not used for the calculation of the linear fit shown.

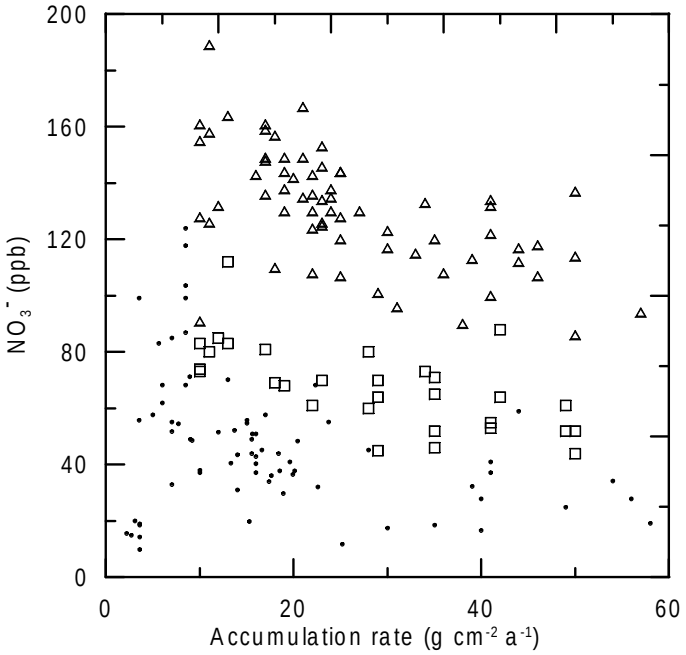


Figure 3: $NO_3^-$ concentrations versus accumulation rate in Greenland and Antarctica (triangles: post-1970, squares: pre-1940, dots: Antarctica).

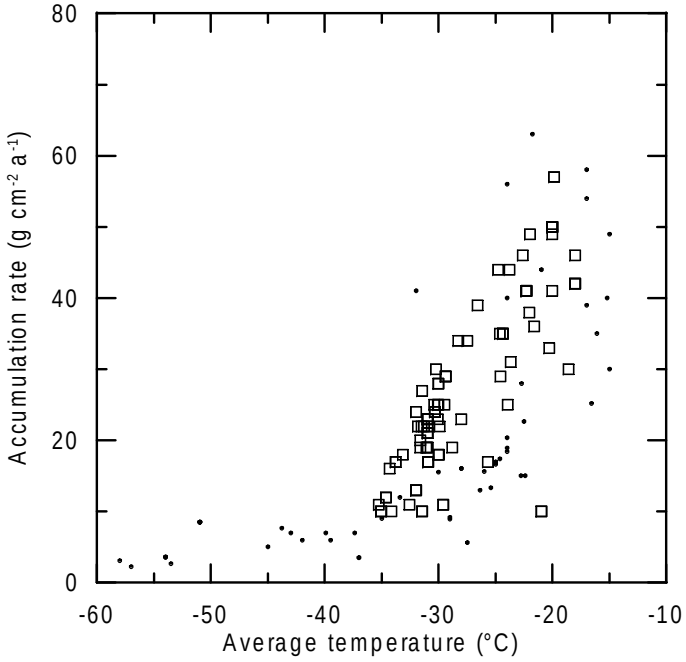


Figure 4: Accumulation rate versus average temperatures in Greenland and Antarctica (squares: Greenland, dots: Antarctica).

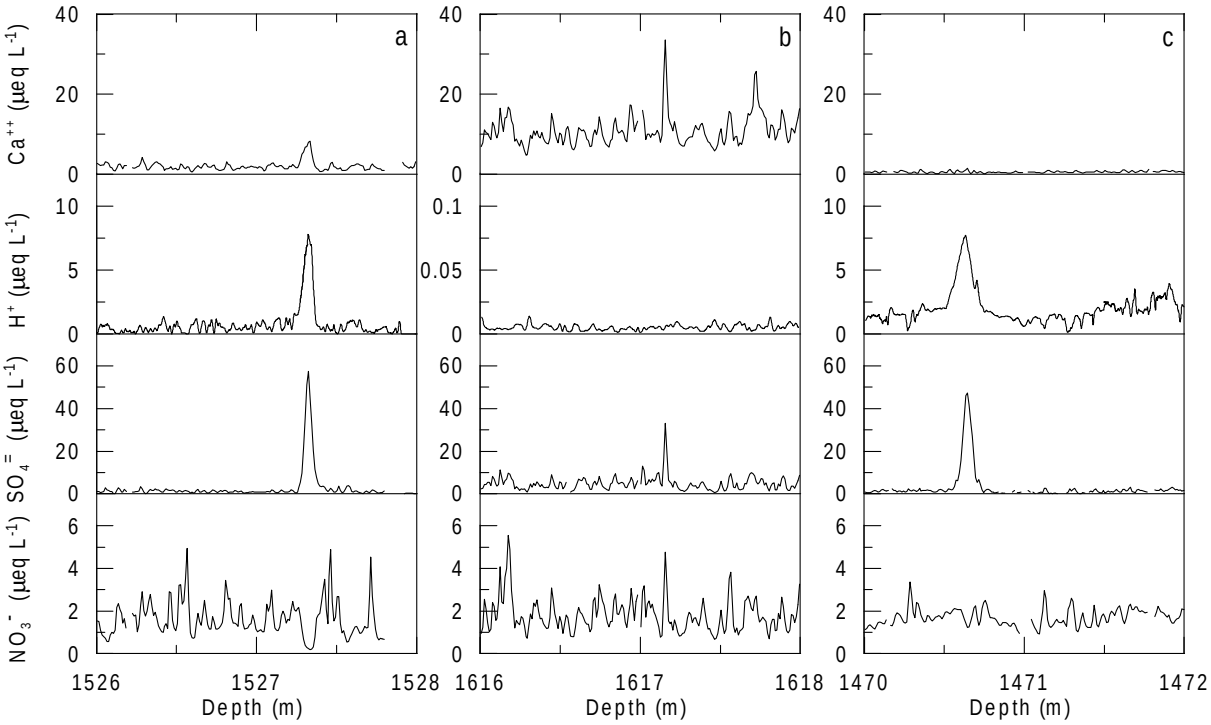


Figure 5: Examples of the influence of volcanic $H_2SO_4$ on $NO_3^-$ in the NGRIP ice core. $H^+$ concentrations have been inferred from electrical conductivity measurements on the solid ice. Due to very low $H^+$ concentrations, the scale of the y-axis had to be adjusted for the section shown in (b). Of 28 events selected with $SO_4^{2-}$ concentrations exceeding 20 $\mu$eq $L^{-1}$, 14 showed a pattern similar to (a), 12 similar to (b), and 2 similar to (c). The data is shown against depth, as the absolute age is not critical to the illustration of the effect and an absolute timescale is not yet available.

# Chapter 7

# Summary and Outlook

The presented work shows that a novel type of particle detector which is based on laser light attenuation by individual microparticles may be used successfully for routine counting and sizing of microparticles in ice core analyses. The robust device yields particle concentration and size distribution and was deployed under field conditions without major operational problems. In combination with continuous sample melting it allows for continuous and high resolution measurements in a CFA-like manner. Using such a setup the NGRIP core was analyzed from 1400 m to 2930 m depth continuously for microparticle concentration and size distribution. This depth interval covers almost the complete last glacial period including the Pleistocene-to-Holocene transition. Two types of data sets were obtained: (i) size distribution, number- and volume-concentration at 1.65 m depth resolution, and (ii) number-concentration at an effective resolution of approximately 1.0 cm. The flow setup between melter and particle detector was found to influence the measured size distribution; this influence should be thoroughly investigated in future work.

Simultaneous measurements of the $Ca^{2+}$ ion concentration and the insoluble microparticle concentration revealed in case studies systematic variations of the $(Ca^{2+})$ / (microparticle) ratio. Strong enhancements of the $(Ca^{2+})$ / (microparticle) ratio were observed during volcanic events; they are due to an increased dissolution of $CaCO_3$ by volcanic $H_2SO_4$ which probably takes place already in the aerosol. On long timescales ($>$ 1000 years) as well as on seasonal to multi-annual timescales the $(Ca^{2+})$ / (microparticle) ratio was found low for high crustal concentrations and vice versa. This points to variable source properties or fractionation during transport. However, to back up these results a detailed investigation of the dissolution process of $CaCO_3$ upon sample melting at low and high concentrations is desirable to exclude any influence of sample acidity on the amount of dissolved $Ca^{2+}$. Also, a dedicated comparison of the CFA-

and IC-measuring methods of $Ca^{2+}$ would be worthwhile.

Further investigation of the $(Ca^{2+})$ / (microparticle) ratio along the NGRIP profile covering the last glacial period should be very interesting and possibly reveal short term and long term variations. Inspection of this ratio at the rapid climatic transitions of D/O-events may allow to differentiate between potential causes for the observed changes: varying source properties should react slowly to changed environmental conditions whereas a change of source area or varying fractionation processes during transport should react promptly.

The microparticle concentration exhibits very strong fluctuations throughout the last glacial and a dynamic range of two orders of magnitude, which confirms earlier Greenlandic studies. The size distribution is found to show systematic variations with the tendency towards larger lognormal modes during cold climates. Such changes of the particle size are also observed at rapid transitions of D/O-events. Further, it is found that the size distribution does not strictly depend on particle concentration; it rather seems that changes of particle concentration and changes of the size distribution are two concurrent but largely independent consequences of changed environmental conditions.

A highly simplified but quantitative model picture was developed for the interpretation of the particle size distribution. It yields that 10% to 20% of the observed size change may be due to changed deposition conditions onto the ice sheet. This means that the observed changes largely reflect changes of the airborne particle size distribution which result from different transit times during long range transport. From the observed size changes it is deduced that transit times were shorter by roughly 25% during LGM compared to the Preboreal. The associated concentration increase from this change is estimated to less than one order of magnitude. This implies that sources were intensified by more than one order of magnitude during the LGM.

In the model picture it was assumed that the size fractionating nature of wet deposition is quenched by its high efficiency during transport as well as during deposition onto the ice sheet. This, however, may not always be the case, and for a refinement of the model picture further investigations of the size fractionation during transport and deposition of particles are highly desirable. Also, possibly changed environmental conditions at the ice sheet during different climates (e.g. a changed seasonality of precipitation or increased snow drift during LGM) may have produced different size shifts during deposition.

The modal particle size shows a remarkable correlation with the marine $\delta^{18}O$ record. This may reflect a modulation of the atmospheric circulation in the northern hemisphere (NH) by the NH continental ice coverage. In this case, a larger ice cover would have lead to faster long range transport of mineral dust between East Asian deserts

and Greenland. A comparison of this hypothesis with the results from GCM-modelling efforts would be interesting and would possibly provide evidence on past atmospheric circulation patterns.

# Appendix A

# Size calibration of the laser sensor – details and listings

Several calibrations of the laser sensor were made during this work as it was found that different versions of the flow setup required individual calibration to compensate for modifications of the size distribution. Also, it was found that the type of operation – continuous long term vs. short time operation — or the addition of NaCl to the sample may influence the calibration.

The specifications of each calibration are given in Table A.1. The respective characteristic curves of the calibrations are given in Table A.2. Calibration *A* is the old calibration by [*Saey*, 1998]. Calibrations *B* and *C* result from comparing Coulter Counter data to laser sensor data from original field measurements. They were used for the work in chapter 5. Calibrations *D, D1* and *D2* are shown for completeness. They result from simultaneous measurements with the Coulter Counter and the Laser Sensor on identical samples, however, they are distinguished by several aspects from routine measurements. First, the laser sensor was switched on (main power) only for approximately 1.5 minutes for each measurement of a discrete sample, which resulted in reduced background noise; second, the flow setup was extremely short; and third, the samples NaCl-enriched to 2% (this is necessary for the Coulter Counter measurements), which may have modified the scattering properties resulting in an altered characteristic curve. Systematic investigations are needed to clarify the effects of these differences before calibrations *D, D1* and *D2* may be used. If it turns out that the salinity has an effect on the characteristic curve then the directed addition of a saline solution to the sample prior to measurement may decrease the lower detection limit to approx. 0.85 $\mu$m diameter. During the measurements of samples used for *D1* and *D2*, a clear difference in the characteristic curve was observed between samples from warm and cold

climatic periods. This may possibly be an indication for differently shaped particles during warm and cold climatic states.

| Calibration | A | B | C | D | D1 | D2 |
|---|---|---|---|---|---|---|
| comment | [*Saey*, 1998] old calibration | NGRIP w/o dilution | NGRIP with dilution | home lab all | home lab warm climate | home lab cold climate |
| sample | pure sample | | | sample modified to 2% NaCl-Solution | | |
| mode of operation | continuous long term operation | | | short term operation | | |
| approx. length of flow lines | short | long, 350 cm | very long, 450 cm | short, 80 cm | short, 80 cm | short, 80 cm |
| Laser sensor data base | — | one 165 cm section from Preb | one 165 cm section each from A, YD, CG, LGM | 8 samples each from Preb, A, YD, CG, LGM | 8 samples from Preb | 8 samples each from YD and LGM |
| Coulter Counter data base | — | one 55 cm long extract from the above | one 55 cm long extract from each of the above | as above (identical) | as above (identical) | as above (identical) |

Table A.1: Specifications for the calibrations given in Table A.2. Abreviations: *Preb*: Preboreal, *A*: Allerød, *YD*: Younger Dryas, *LGM*: Last Glacial Maximum, *CG*: cold glacial period. For calibrations D, D1, and D2 8 adjacent samples were used covering a 55 cm long section.

| Calibration | A | B | C | D | D1 | D2 |
|---|---|---|---|---|---|---|
| peak height [mV] | corresponding particle diameter [$\mu$m] | | | | | |
| 126 | – | – | – | 0.85 | 0.80 | 0.88 |
| 147 | – | – | – | 0.87 | 0.83 | 0.89 |
| 168 | – | – | – | 0.94 | 0.91 | 0.96 |
| 189 | – | – | – | 1.09 | 1.07 | 1.10 |
| 210 | 1.0 | 0.94 | 1.01 | 1.26 | 1.22 | 1.26 |
| 260 | 1.3 | 1.02 | 1.12 | 1.49 | 1.47 | 1.49 |
| 345 | 1.6 | 1.22 | 1.34 | 1.67 | 1.68 | 1.65 |
| 569 | 2.0 | 1.44 | 1.57 | 1.98 | 1.99 | 1.95 |
| 910 | 2.5 | 1.71 | 1.87 | 2.42 | 2.43 | 2.40 |
| 1420 | 3.2 | 2.10 | 2.32 | 3.09 | 3.09 | 3.09 |
| 2180 | 4.0 | 2.73 | 3.05 | 4.13 | 3.80 | 4.13 |
| 3241 | 5.1 | 3.86 | 4.21 | 5.44 | 4.85 | 5.47 |
| 4500 | 6.4 | 4.63 | 5.56 | 7.28 | 6.90 | 7.41 |
| 6180 | 8.1 | 6.53 | 7.50 | 8.40 | 8.20 | 9.00 |
| 8802 | 10.2 | 8.50 | 9.37 | 9.90 | 9.90 | 10.9 |
| 9999 | 11.0 | 13.5 | 11.2 | 11.0 | 11.0 | 11.6 |

Table A.2: Calibrations of the laser sensor. Specifications for each calibration are given in Table A.1.

# Appendix B

# Die Schmelzapparatur

In diesem und in den beiden folgenden Kapiteln ist über die Partikelmessung hinausgehende Messmethodik beschrieben, die im Rahmen dieser Arbeit angewandt und teilweise entwickelt wurde. Größtenteils beziehen sich die Beschreibungen auf Anwendungen, die in Arbeiten im 'Heimlabor' und auf Feldkampagnen durchgeführt wurden. Hier wurde ein Messplatz aufgebaut, der dem während der NGRIP 2000 Feldsaison verwendeten ähnlich ist. Er ermöglicht das kontrollierte Schmelzen eines Eisbohrkerns im Labor. Am kontinuierlich anfallenden Schmelzwasserstrom können direkt Analysen mit hoher Tiefenauflösung durchgeführt werden. Zu den im 'Heimlabor' durchgeführten Analysen gehörte neben der Partikelmessung, die im Hauptteil dieser Arbeit beschrieben ist, auch die Messung von Leitfähigkeit und Azidität. Mit dem entstandenen Aufbau wurden umfangreiche Messungen am B25-Bohrkern von Berkner Island (Antarktis) und an mehreren flachen Firnkernen von Severnaya Semlya (Russische Arktis) erflogreich durchgeführt. Die wissenschaftlichen Ergebnisse dieser Arbeiten werden nicht im Rahmen der vorliegenden Arbeit beschrieben. Allerdings werden im folgenden ausgewählte methodische Aspekte dokumentiert. Die dargestellten Arbeiten sind am Institut für Umweltphysik, Heidelberg, (IUP) im Rahmen eines Kooperationsvertrages zwischen dem IUP und dem Alfred-Wegener-Institut, Bremerhaven, entstanden.

## B.1 Vorteile des kontrollierten Längsschmelzens

Die traditionelle Methode der Aufbereitung für kontaminationsgefährdete Spurenstoffmessungen an Polareisproben ist sehr zeitintensiv und fehleranfällig. Für sogenannte chemische Analysen, womit üblicherweise die Konzentrationsbestimmung der gut wasserlöslichen Hauptionen ($SO_4^{2-}$, $NO_3^-$, $Cl^-$, $MSA^-$, $F^-$ und $Br^-$ sowie $Ca^{2+}$, $Na^+$,

$NH_4^+$, $Mg^{2+}$ und $K^+$) mittels Ionenchromatographie (IC) gemeint ist, ist außer dem Zuschneiden der einzelnen Probenstücke – der sogenannten Aliquotierung – noch eine umfangreiche Dekontaminationsprozedur notwendig. Hierbei wird von jedem Aliquot der äußere Bereich von allen Seiten abgetragen (z.B. mittels Mikrotom oder elektrischem Hobel), um dasjenige Probenmaterial zu entfernen, das kontaminiert sein könnte [*Fischer*, 1997]. Dies erfordert sehr sorgfältiges und langwieriges Arbeiten im Kühllabor.

Beim Arbeiten mit der Schmelzapparatur dagegen wird ein Längsaliquot eines Bohrkerns entlang der Tiefenachse aufgeschmolzen. Dies geschieht mittels eines Schmelzkopfes, durch den die anfallende Probe abgepumpt wird. Der so entstehende kontinuierliche Flüssigkeitsstrom kann verschiedenen Analyseeinheiten oder auch einer Probenabfüllung zugeführt werden. Die Dekontamination des Probenmaterials erfolgt dabei am Schmelzkopf, der dafür in mehrere Zonen eingeteilt ist (s. unten).

Der Einsatz einer Schmelzapparatur erlaubt nicht nur das kontaminationsfreie Abfüllen von diskreten Proben; es können am Probenwasserstrom auch Messungen mit sehr hoher Tiefenauflösung durchgeführt werden. Dabei werden Analyseeinheiten verwendet, die im kontinuierlichen Durchfluss arbeiten (continuous flow analysis, CFA). Hierfür kommen direkte Messungen der elektrolytischen Leitfähigkeit und des Mikropartikelgehalts in Frage, vor allem aber auch in kontinuierlichem Durchfluss betriebenen chemische Reaktionen mit anschließender Spektroskopie zur Bestimmung ausgewählter Ionenkonzentrationen [*Röthlisberger et al.*, 2000]. Bei gleichzeitiger Verwendung einer automatischen Probenabfüllung für anschließende konventionelle (diskrete) Messungen hat man diese CFA-Analysemöglichkeiten *zusätzlich* und nicht alternativ zu den herkömmlichen, etablierten Messverfahren wie z.B. der Ionenchromatographie.

Ein weiterer Vorteil beim Arbeiten mit der Schmelzapparatur ist die hohe Arbeitseffizienz. Bei Kernmaterial, das keine Brüche aufweist, verkürzt sich die Arbeitszeit im Kaltlabor auf wenige Minuten pro Meter Eis. Beim Schmelzen beschränken sich die Arbeiten des Benutzers auf das Vorbereiten der Anlage und das aufmerksame Überwachen des Schmelzprozesses. Ein zentraler Messrechner nimmt die Messdaten auf und steuert gleichzeitig den Probenwechsler.

## B.2 Anforderungen an die Schmelzanlage

Die Schmelzanlage muss eine zuverlässige Dekontamination der Probe gewährleisten und einen konstanten, blasenfreien Probenflüssigkeitsstrom bereitstellen. Dafür ist eine exakte Kernführung notwendig, die auch ein Verrutschen der Kernstücke an Brüchen

verhindert; außerdem muss ein Festfrieren oder Klemmen des Kerns an der Kernführung ausgeschlossen werden. Um später eine Tiefenzuordnung der Messdaten vornehmen zu können, muss die Kernposition bestimmt werden. Ferner wird verlangt, dass alle gewonnenen Daten elektronisch fließend gesichert werden.

Am Institut für Umweltphysik (IUP) der Universität Heidelberg wird seit Anfang der 90er-Jahre an der Entwicklung einer Schmelzapparatur gearbeitet (z.B. [*Kolb*, 1995; *Saey*, 1998]). Im Rahmen dieser Arbeit und bei [*Armbruster*, 2000] ist es erstmals zu einer Anwendung im Routinebetrieb gekommen.

## B.3 Beschreibung der Apparatur

Im Unterschied zu bereits existierenden Schmelzanlagen (z.B. [*Sommer*, 2000]), die über keine aktive Kühlung verfügen, besitzt das am IUP entwickelte Modell eine eigene Kühlung. Dies ermöglicht den Betrieb auch in normalen Laborräumen bei Raumtemperatur, während die anderen Modelle nur bei negativen Temperaturen in gekühlten Räumen oder während Feldkampagnen eingesetzt werden können. Außerdem ist am IUP ein Schmelzkopf speziell zur Verarbeitung von Firnproben entwickelt worden [*Röthlisberger et al.*, 2000].

Die Schmelzanlage besteht im wesentlichen aus folgenden Teilen:

- Kühlsystem mit Probenaufnahme und Schmelzkopf
- Schlauchsystem mit Pumpen
- Nachweissysteme
- Probenabfüllung
- Datenaufnahme und Prozesssteuerung

Im folgenden wird auf diese Punkte einzeln eingegangen:

### B.3.1 Kühlsystem mit Probenaufnahme und Schmelzkopf

Das Kühlsystem ist eine kompakte, zylinderförmige Einheit, die das Eiskernstück aufnimmt und auf -20$^o$C kühlt (siehe Abbildung B.1). Es besteht aus einem Kupferrohr, auf dessen Außenseite eine Rohrwendel aufgebracht ist, die von einem Kühlmittel durchströmt wird. Im Innern des Kupferrohrs befindet sich ein Gleitrohr aus Plexiglas, das das Eiskernstück aufnimmt und mittig auf dem Schmelzkopf positioniert. Da

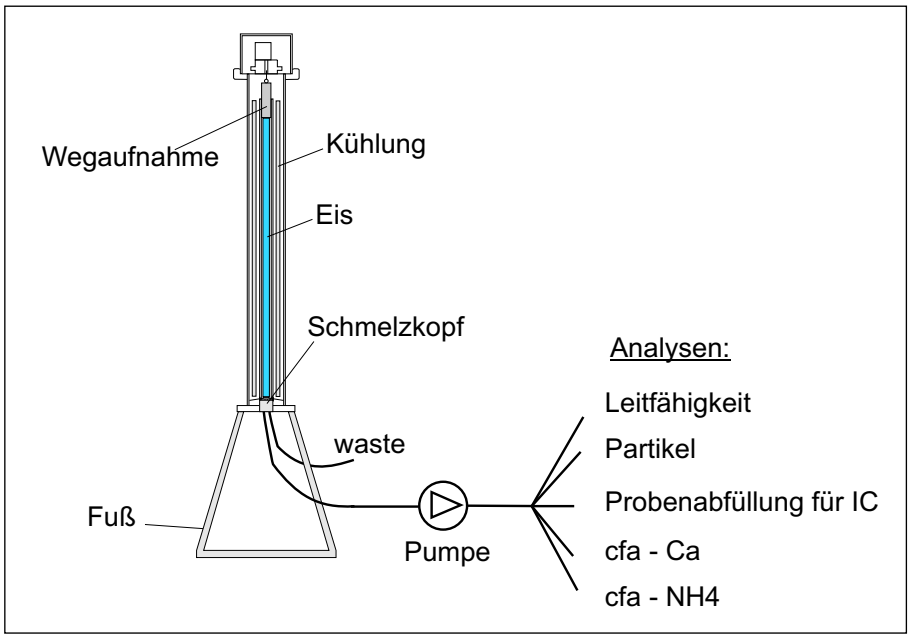


Figure B.1: Schematische Darstellung der Schmelzapparatur und Analysesysteme. Verändert und ergänzt nach [*Saey*, 1998].

das Kernstück in aller Regel einen rechteckigen Querschnitt besitzt, liegt es nur mit seinen vier Kanten, nicht aber mit den Seitenflächen an dem zylindrischen Gleitrohr an; dadurch ist die Gefahr minimiert, dass das Kernstück am Gleitrohr anfriert oder infolge erhöhter Reibung stecken bleibt. Je nach Kernquerschnitt werden Gleitrohre mit verschiedenen Innendurchmessern verwendet.

Zum Beladen der Einheit kann das Kühlrohr in waagerechte Position gekippt werden, wodurch das Einführen der "Ladung" erleichtert wird. Zum Starten des Schmelzvorgangs wird das Kühlrohr in senkrechte Position gekippt und die Schmelzkopfheizung eingeschaltet. Während des Schmelzens liefert ein Wegaufnehmer die absolute Position des Eisendes, die für die spätere Tiefenzuweisung bekannt sein muss. Das Kühlsystem ist so ausgeführt, dass es mit einer Vakuumpumpe evakuiert werden kann, um es anschließend mit Stickstoff oder einem anderen Schutzgas zu befüllen. Dadurch wird besonders beim Schmelzen von Firnkernen die Kontamination durch $NH_4^+$ und $CO_2$ reduziert, die sich in der Luft im Porenraum des Firns befindet und beim Schmelzen in die Probe gelangen.

Der Schmelzkopf ist das zentrale Stück der Schmelzanlage. Er besteht aus harteloxiertem Aluminium und besitzt einen inneren und einen äußeren Bereich, die getrennt voneinander abgepumpt werden können (siehe Abbildung B.2). Die Schmelzflüssigkeit des inneren Bereichs liefert den Probenstrom für die Analysen und die Probenabfüllung;

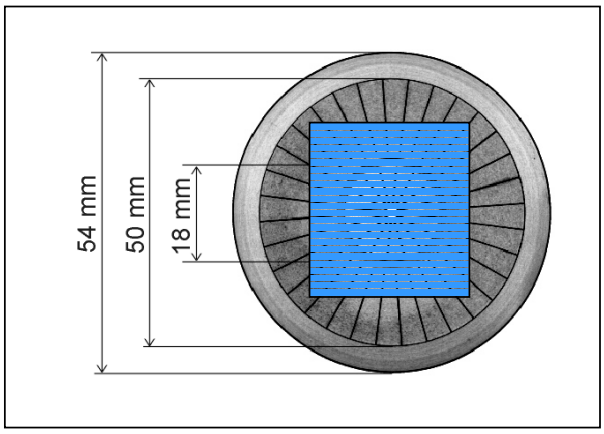


Figure B.2: Firnschmelzkopf mit Eisquerschnitt.

die Flüssigkeit des äußeren Bereichs wird verworfen oder für nicht kontaminationsgefährdete Analysen verwendet. Die Eiskernstücke müssen so dimensioniert sein, dass das Schmelzwasser der kontaminierten Außenflächen nur in den äußeren, nicht aber in den inneren Bereich des Schmelzkopfes gelangen kann; so gelangt nur kontaminationsfreies Probenmaterial in den inneren Bereich. Besonders beim Prozessieren von porösem Firn muss darauf geachtet werden, dass der Kernstückdurchmesser deutlich größer ist als der Durchmesser des inneren Schmelzkopfbereiches.

Der in Abbildung B.2 dargestellte Schmelzkopf ist speziell zum Schmelzen von Firn entwickelt worden. Beim Schmelzen von Firn tritt das Problem auf, dass das Schmelzwasser durch die im Porenraum entstehenden Kapillarkräfte vom Schmelzkopf weg in den Porenraum des Firns hineingesogen wird. Dadurch wird die strenge stratigraphische Schichtung beeinträchtigt und die Auflösung durch zusätzliche Signaldispersion reduziert. Ferner besteht die Gefahr der Probenkontamination, da beim Schmelzen verunreinigtes Probenmaterial aus dem äußeren Bereich in den inneren Bereich der Probe wandern könnte. Dem wird durch eine geschlitzte Oberfläche des Schmelzkopfes begegnet: An den Schlitzen entstehen nun ebenfalls Kapillarkräfte, die die Kapillarwirkung des Firns kompensieren, sodass beim Schmelzen von Firn keine zusätzliche Signaldispersion gegenber dem Schmelzen von Eis auftritt.

Der Schmelzkopf wird über einen kombinierten Temperaturregler und Leistungsdosierer geheizt, der zwei verschiedene Betriebsarten zulässt: Schmelzen bei konstanter Temperatur oder Schmelzen bei konstanter Heizleistung. Letzteres hat den Vorteil, dass sich beim Prozessieren von Kernmaterial mit grossen Dichteunterschieden – wie z.B. beim Firn von Severnaya Zemlya, der viele Eislagen enthält – diese Dichteunterschiede stärker in der Schmelzgeschwindigkeit abbilden; hier kann man die Variabilität der Schmelzgeschwindigkeit als Approximation für die Variabilität der Dichte benutzen.

| | |
|---|---|
| Kühltemperatur | -20$^o$C |
| Schmelzkopftemperatur | +20$^o$C |
| Schmelzgeschwindigkeit (Eis) | 2.6 cm/min |
| Schmelzgeschwindigkeit (Firn) | 3.9 cm/min |

Table B.1: Typische Werte der Arbeitsparameter Kühltemperatur und Schmelzkopftemperatur sowie typische Werte der resultierenden Schmelzgeschwindigkeit für Eis- und Firnproben.

Typische Parameter für einen Schmelzdurchgang sind in Tabelle B.1 aufgeführt.

### B.3.2 Schlauchsystem mit Pumpen

Für den Aufbau des Schlauchsystems wurde grundsätzlich Schlauchmaterial aus Teflon mit 1/32-inch (1.6 mm) Außendurchmesser verwendet. Je nach Anforderung kamen Innendurchmesser von 0.5 mm, 0.8 mm oder 1.0 mm zum Einsatz. Dieses Schlauchmaterial hat sich durch seine Reinheit und Belastbarkeit bewährt. Schlauchverbindungen wurden wenn möglich immer verschraubt ("flangeless fingertight fittings"); und nur die Verbindungen zu den weicheren Pumpschläuchen oder den Silikonschläuchen der Probenabfüllung wurden gesteckt. Als Pumpen wurden Peristaltik-Pumpen (auch Schlauchpumpen oder Quetschpumpen genannt) der Firmen Perimax und Ismatec verwendet. Bei diesen Pumpen wird der sogenannte Pumpschlauch im Halbkreis auf eine langsam rotierende, mit Walzen besetzte Trommel gedrückt; der Flüssigkeitstransport kommt dadurch zustande, dass die Walzen den Schlauch zusammendrücken und bei ihrer Drehbewegung die Flüssigkeit vor sich herschieben. Die Pumpleistung wird durch die Rotationsgeschwindigkeit der Pumpe und den Pumpschlauchinnendurchmesser bestimmt. Eine Pumpe hat mehrere Kanäle; durch Verwendung unterschiedlicher Pumpschlauchdurchmesser können die Pumpleistungen der jeweiligen Kanäle relativ zueinander eingestellt werden. Für die Pumpschläuche wird PVC-Material verwendet.

Eine schematische Skizze des Messaufbaus ist in Abbildung B.3 dargestellt. Das Schmelzwasser aus dem äußeren Bereich des Schmelzkopfes wird verworfen (waste); das Schmelzwasser aus dem inneren Bereich wird über einen Debubbler und das Ventil `V1` in das Analysesystem geleitet und an der Stelle `Y` in zwei Untersysteme verzweigt. Der Debubbler (Accurel-Membran) hat die Funktion, Luftblasen aus dem Schmelzwasserstrom zu entfernen, weil diese das Verzweigungsverhältnis des Probenstroms an der Stelle `Y` beeinflussen können; da die anschließenden Blasenfängerkammern `B` Luftblasen nicht vollständig entfernen, kann durch Verwendung des vorgeschalteten Membran-Debubblers zuverlässiger gewährleistet werden, dass der Probenstrom die Analysesy-

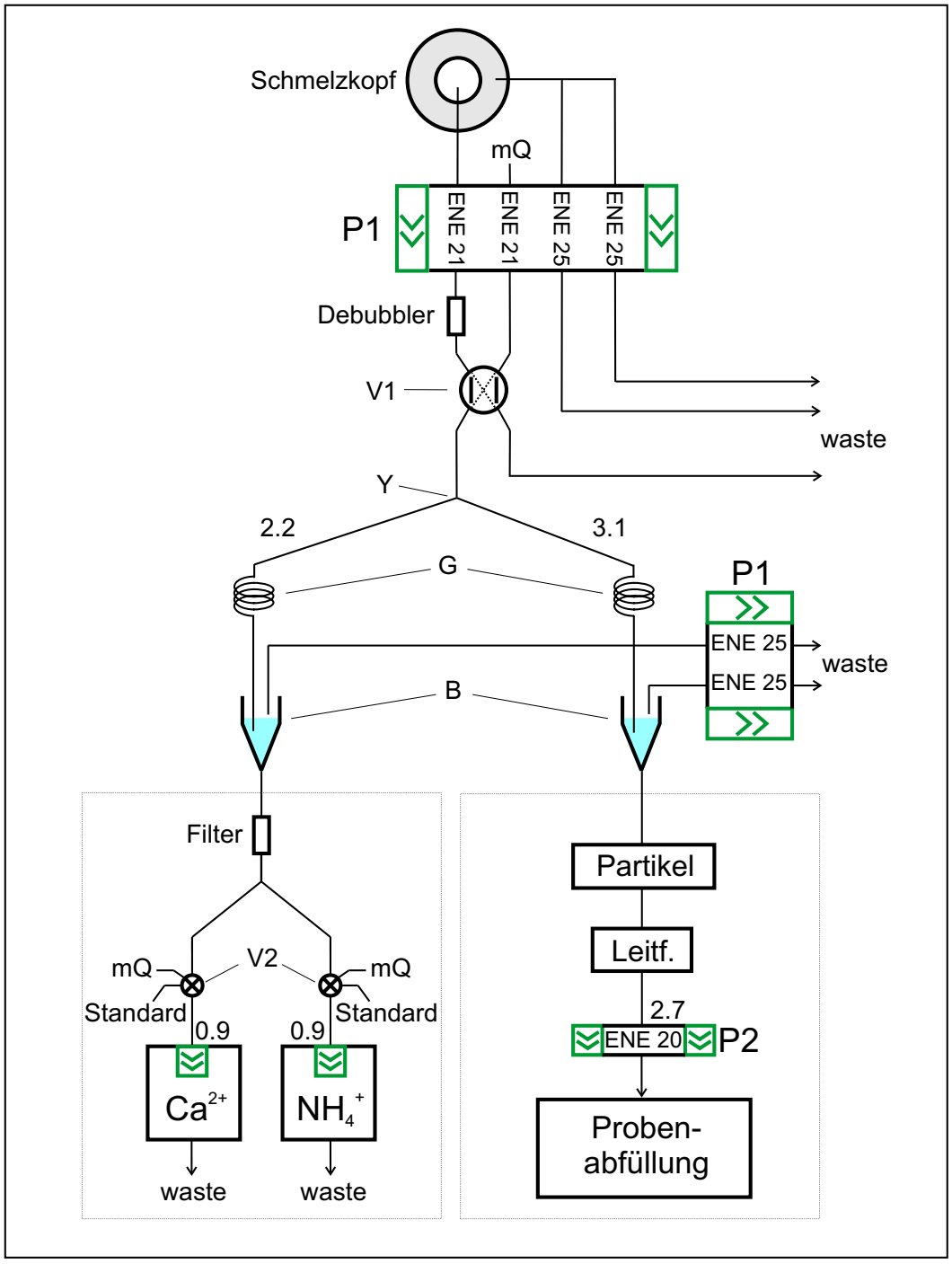


Figure B.3: Schematische Darstellung des Schlauchsystems mit Analyseeinheiten. An den Pumpen `P1` und `P2` sind die verwendeten Pumpschlauchdimensionen angegeben ('ENE-Nr.'); die Pumpe `P1` mit insgesamt sechs Kanälen wurde zur übersichtlicheren Darstellung aufgeteilt. Einzelne Zahlen im Diagramm beziffern Fließraten in ml/min. Zur Erläuterung siehe Text.

steme tatsächlich luftblasenfrei erreicht. Das Ventil V1 ermöglicht es, vor oder nach dem Schmelzvorgang Reinstwasser in das System einzuspeisen (Nullwasser für den Leerlaufbetrieb).

Nach der Verzweigung Y sind die Gegendruckschleifen G zur Stabilisierung des Verzweigungsverhältnis notwendig, da in Ermangelung eines weiteren Pumpkanals an der Pumpe P1 die Probenflüssigkeit durch die Verzweigung gedrückt werden muss und nicht gesaugt werden kann. Als Blasenfängerkammern B, die auch in ihrer Funktion als Puffergefäße notwendig sind, werden 1000$\mu$l-Pipettenspitzen genommen. Im Mittel wird etwa 10%-20% mehr Probe zugeführt, als für das Analysesystem entnommen wird. Die überschüssige Probe wird abgesaugt und verworfen. Verringert sich der Probenfluss – z.B. durch geringere Schmelzgeschwindigkeit oder erhöhten Luftgehalt der Probe – können kurzzeitige Schwankungen im Probenfluss ausgeglichen werden und die Analysesysteme fallen nicht trocken. Dazu sind die Schläuche im Puffergefäß so justiert, dass die Zuführung einige Millimeter unterhalb der Absaugung liegt. Dies ist wichtig, da in manchen Nachweissystemen Luftblasen zu sehr starken Störungen führen, die nachträglich nicht herauskorrigiert werden können. Die chemischen Nachweissysteme werden durch einen Glaswollefilter vor groben Partikeln geschützt; in dem Zweig mit der Partikelmessung wurde bewusst darauf verzichtet, um die Partikelmessung nicht zu verfälschen. Hier befindet sich außerdem die Pumpe P2 hinter dem Partikelmessgerät, da von [*Saey*, 1998] berichtet wurde, dass die Pumpschläuche einen erhöhten Partikelblank verursachten.

### B.3.3 Nachweissysteme

Die Systeme für die Messung der elektrolytischen Leitfähigkeit und für die Partikelmessung werden im Anhang C bzw. in Kapitel 3 genauer beschrieben. Das $Ca^{2+}$- und das $NH_4^+$-Nachweissystem wurden freundlicherweise von der Arbeitsgruppe um Prof. B. Stauffer von der Universität Bern zur Verfügung gestellt. Beide Systeme sind beispielsweise in [*Röthlisberger et al.*, 2000] beschrieben. Die Nachweise beruhen auf chemischen Reaktionen mit anschließender Fluoreszenzspektroskopie. In der chemischen Reaktion wird dem nachzuweisenden Ion selektiv und quantitativ ein fluoreszierender Indikator "angeheftet" wird, der dabei seine Fluoreszenzeigenschaften verändert. Dadurch ist die Stärke des Fluoreszenzlichtes proportional zur Konzentration des nachzuweisenden Ions.

### B.3.4 Probenabfüllung

Während die Probenflüssigkeit der chemischen Analysen mit Reagenzien vermischt und damit für weitere Verwendung unbrauchbar wird, wird die Probenflüssigkeit der Leitfähigkeits– und Partikelmessung nicht beeinträchtigt und kann weiterverwendet werden. Sie wurde daher einer automatischen Probenabfüllung für spätere IC– und Aziditätsmessungen zugeführt.

Die Probenabfüllung wurde als Prototyp aus einem automatischen Probenwechsler der Fa. Dionex gebaut. Dieser dient normalerweise der automatischen Probenaufgabe bei IC-Messungen. Er wurde dahingehend modifiziert, dass die IC-Probenbehälter (sogenannte Polyvials) nicht entleert werden, sondern dass leere, messfertige Polyvials (mit bereits aufgesetzten Stopfen) mit der Probenflüssigkeit befüllt werden. Dazu wurde die normale Probenspitze durch eine Edelstahlkanüle ersetzt und die Kontakte für die Steuerungsimpulse durch ein Interface nach außen gelegt. So können alle benötigten Funktionen des Probenwechslers (Probenspitze hoch– und runterfahren, Transport zum nächsten Probengefäß) über den zentralen Messrechner gesteuert werden.

Ein Probengefäßwechsel dauert bei dem verwendeten Gerät ca. 20 s. Da währenddessen kontinuierlich Probenflüssigkeit anfällt, die nicht verloren gehen darf, muss sie während des Wechsels zwischengespeichert werden (siehe Abbildung B.4). Dazu wird für die Dauer des Probengefäßwechsels der Flüssigkeitsstrom mittels eines Magnetventils abgesperrt und ein Puffergefäß damit gefüllt. Als Puffergefäß dient eine druckdicht verschlossene 5 ml Pipettenspitze; sie wird während des Gefäßwechsels teilweise gefüllt und entleert sich anschliessend durch den aufgebauten Druck von selbst. Bei der Dimensionierung des Puffergefäßes hat es sich bewährt, das Gefäßvolumen etwa fünfmal größer zu wählen als das zu puffernde Flüssigkeitsvolumen. Dadurch ist der Druckaufbau einerseits groß genug, dass eine vollständige Entleerung statt findet; andererseits ist der Druckaufbau im Puffergefäß niedrig genug, so dass es im Moment des Öffnens des Absperrventils nicht zu Druckschwankungen im vorgeschalteten Flusssystem kommt, wodurch vor allem die Partikelmessung beeinträchtigt würde.

Um den Schmelzvorgang mit Probenabfüllung von der anschliessenden IC– und Aziditätsmessung organisatorisch zu entkoppeln, wurden die gewonnenen Proben nicht sofort gemessen, sondern zwischengelagert. Hierzu wurden sie unverzüglich eingefroren, um einer Veränderung durch chemische oder biologische Prozesse vorzubeugen. Kurze Zeit vor der Messung können sie an der Umgebungsluft oder vorsichtig in einem Mikrowellenofen wieder aufgetaut werden.

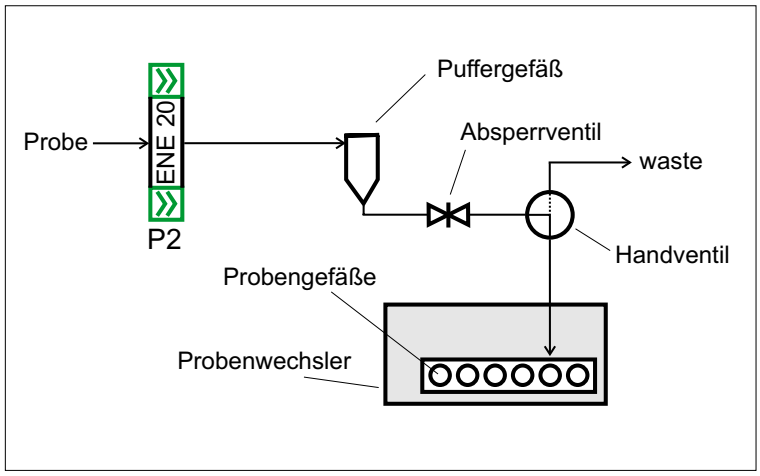


Figure B.4: Schematische Darstellung der Probenabfüllung.

### B.3.5 Datenaufnahme und Prozesssteuerung

Die Kühlung der Schmelzapparatur und die Heizung des Schmelzkopfes sind autark gesteuert. Die gesamte Datenaufnahme und die Steuerung des Probengefäßwechsels jedoch wird von einem zentralen Messrechner aus durchgeführt. Hierfür wird das Data-Aquisition (DAQ)-Interface DAQ-Pad Mio16XE50 der Fa. National Instruments verwendet, das mit einem selbstgeschriebenen Lab-View Programm angesteuert wird. Sowohl die Relaissteuerung für das Absperrventil und die TTL-Steuerung für den Probenwechsler als auch die Datenaufnahme werden von dem Programm `"Schmelzview 4komp.vi"` bewerkstelligt. Es ermöglicht die Aufzeichnung der Wegaufnehmerposition und von vier analogen Messkanälen und ist leicht auf mehr Komponenten erweiterbar. Aus Gründen der Datensicherheit werden die Messdaten in 1-Sekunden-Mittelwerten fliessend auf Festplatte geschrieben (data stream to file). Bei der Steuerung der Probenabfüllung kann zwischen einer rigiden Zeitsteuerung (Probenabfüllung z.B. alle 90 s) und einer Tiefensteuerung (Probenwechsel bei frei wählbaren Kernpositionen) gewählt werden. Im Routinebetrieb wurde hauptsächlich die Zeitsteuerung verwendet, da sie weniger anfällig gegenüber Störungen des Schmelzbetriebes ist.

Die aufgenommenen Messdaten der letzten 100 Sekunden werden in Verlaufsdiagrammen dargestellt. Aufgrund unterschiedlicher Laufzeiten der Probenflüssigkeit vom Schmelzkopf zum jeweiligem Nachweissystem sind die Datensätze zum Zeitpunkt der Datenaufnahme gegeneinander verschoben, d.h. sie sind nicht ”synchron” in Bezug auf die Kernposition. Dies kann erst im Rahmen der Datenauswertung (siehe unten) korrigiert werden. Die Verlaufsdiagramme sind jedoch sehr hilfreich, um Fehlfunktionen der Nachweissysteme oder der Schmelzanlage zu erkennen und um einen ersten

Eindruck von der Signalstärke und Variabilität der Messgrößen zu gewinnen. Das Programm überwacht ferner die Schmelzgeschwindigkeit und warnt den Betreiber, falls ein frei vorgebbarer Minimalwert unterschritten wird. Dies ist besonders von Vorteil am Ende des Schmelzvorgangs oder falls der Kern einmal stecken bleibt.

## B.4 Kalibration, Blanks und Tiefenauflösung

Die jeweiligen Nachweissysteme erfordern Kalibrationen in unterschiedlicher Häufigkeit. Der Partikelzähler besitzt im eingesetzten Größenbereich eine Zähleffizienz von Eins und braucht daher nicht kalibriert zu werden. Koinzidenzverluste werden bis zu einem bestimmten Grad geräteintern kompensiert; sie machen sich erst oberhalb 4000 Partikel pro Sek. bemerkbar, d.h. oberhalb der Zählrate, bei der der Analogausgang in die Sättigung läuft (siehe Kapitel 3) [*Saey*, 1998]. Zur Bestimmung einer Grössenverteilung und der Partikelvolumenkonzentration muss allerdings eine Größenkalibration durchgeführt werden. Dies ist ebenfalls in Kapitel 3 beschrieben.

Bei der Kalibration der Leitfähigkeitsmessung wurde darauf geachtet, Konsistenz zwischen den verschiedenen verwendeten Zellen herzustellen. Die Zellen wurden auf eine WTW-Tauchelektrode abgestimmt, welche zuvor mittels einer hochverdünnten KCl-Lösung bekannter Leitfähigkeit kalibriert worden war. Die Kalibration wurde einmal wöchentlich überprüft.

Die Nachweissysteme für $Ca^{2+}$ und $NH_4^+$ verhalten sich zwar hochgradig linear, allerdings mit variabler (linearer) Kennlinie. Sie wurden daher bei jedem zweiten Schmelzdurchgang (d.h. etwa alle 1.5 Stunden) mit einer 2-Punkt-Kalibration nachkalibriert, wobei mittels Nullwasser die Basislinie und mittels eines Standards die Steigung einer linearen Antwortfunktion bestimmt wurde. Insgesamt wurde bei einem Vergleich von CFA- und IC-Messungen eine gute Übereinstimmung mit Abweichungen von wenigen Prozent festgestellt [*Armbruster*, 2000]; neuere Ergebnisse zeigen allerdings, dass eine genaue Untersuchung des $Ca^{2+}$-Nachweises im Hinblick auf die Lösung von $CaCO_3$ wünschenswert wäre (siehe Kapitel 4).

Blankwerte sind die Konzentrationen, die für Nullproben bestimmt werden. Für die CFA $Ca^{2+}$- und $NH_4^+$-Systeme wird der Wert des Mess-Blanks durch das Setzen der Basislinie kompensiert. Dasselbe würde auch für die Partikelmessung gelten; allerdings liegt hier die Basislinie ohnehin bei Null und braucht daher nicht berücksichtigt zu werden. Eine systematische Verfälschung der Leitfähigkeitsmessung durch etwaige Verunreinigungen, die während des Schmelzvorgangs in den Probenstrom gelangen, kann vernachlässigt werden. Die Leitfähigkeit kann lediglich durch in der Probenflüssigkeit

| | |
|---|---|
| $F^-$ | 0.3±0.2 ppb |
| $MSA^-$ | 0.7±0.1 ppb |
| $Cl^-$ | 0.8±0.3 ppb |
| $NO_3^-$ | 0.4±0.2 ppb |
| $SO_4^{2-}$ | 9.4±2.3 ppb |

Table B.2: Prozessblanks von Kernvorbereitung, Schmelzen, automatischer Abfüllung und IC-Messung.

gelöstes $CO_2$ aus dem Laborluftsystem verfälscht werden. Dieser Effekt wurde im Rahmen der vorliegenden Arbeit jedoch nicht systematisch untersucht. Alle verwendeten Nachweissysteme sind anfällig für "episodische" Verunreinigungen, die aufgrund unzulänglicher Dekontamination am Schmelzkopf in das Nachweissystem gelangen. Dies kann dadurch verursacht werden, dass Material vom äußeren Rand des Kernstücks in den inneren Bereich des Schmelzkopfes gerät (beispielsweise weil ein Kernstück zu schmal gesägt wurde, oder es etwa kurz vor einem Bruch in der Kernführung verkippt) oder dass es während der Kernvorbereitung an den Stirnflächen nicht ausreichend dekontaminiert wurde. Verunreinigungen dieser Art müssen während der Datenauswertung identifiziert und die entsprechenden Eintragungen aus dem Datensatz entfernt werden.

In Tabelle B.2 sind die IC-Anionen-Prozessblanks der mit der Schmelzanlage abgefüllten Proben zusammengefasst. $F^-$, $MSA^-$, $Cl^-$ und $NO_3^-$ zeigen sehr gute Werte. Das Ergebnis für $SO_4^{2-}$ dagegen ist mangelhaft. Die Verunreinigungsquelle für die $SO_4^{2-}$-Kontamination konnte auf den Schmelzkopf eingeschränkt werden, doch trotz gründlicher Reinigung des Schmelzkopfes mit Wasser und Isopropanol unter Ultraschall blieb der hohe $SO_4^{2-}$-Blank bestehen. Möglicherweise wird die Kontamination durch einen schwer löslichen Film von $CuSO_4$ oder durch Fertigungsrückstände der Eloxierung verursacht. Hier zeigt sich ein Nachteil des Firnschmelzkopfes gegenüber einfacher gebauten Modellen; durch seine komplexe Bauform lässt er sich schlechter reinigen als z.B. ein Eisschmelzkopf wie er von der Universität Bern verwendet wird.

Die Tiefenauflösung einer Online-Messung wird bestimmt durch die Schmelzgeschwindigkeit, die Probendispersion im Schmelzkopf und im anschliessenden Schlauchsystem (Vermischung in Totvolumina und longitudinale Dispersion) sowie durch das Ansprechverhalten des Messgerätes. In Tabelle B.3 sind typische Tiefenauflösungen der CFA-Nachweiskomponenten aufgeführt, wie sie in dieser Arbeit erzielt wurden. Die Werte wurden ermittelt aus dem Anstieg und Abfall der Signale beim Schmelzen einer Abfolge von künstlich präparierten Kernen mit unterschiedlichen Konzentratio-

| | |
|---|---|
| Leitfähigkeit | 0.7 cm |
| Partikel | 0.6 cm |
| $Ca^{2+}$ | 1.1 cm |
| $NH_4^+$ | 0.7 cm |

Table B.3: Typische Werte der Tiefenauflösung der CFA-Nachweiskomponenten; die angegebenen Werte sind $1/e$-Werte für Eisproben, die unter Bedingungen der in Tabelle B.1 angegebenen Parameter geschmolzen wurden.

nen (siehe auch [*Armbruster*, 2000]).

## B.5 Vorbereitung der Proben im Kühllabor

Die Heidelberger Schmelzanlage kann Längsaliquote von maximal 71 cm Länge und einem Querschnitt von 2.5 cm x 2.5 cm bis 3.1 cm x 3.1 cm aufnehmen. Diese Kernstücke werden im Kühllabor bei Temperaturen zwischen -10$^o$C und -20$^o$C vorbereitet. Ein gerades Zuschneiden ist dabei sehr wichtig, damit auch längere Kernstücke bündig in die zylindrischen Gleitrohre aus Plexiglas passen. Kernstücke, die länger als 71 cm sind, müssen zerteilt und nacheinander gemessen werden. Es können auch mehrere kürzere Kernstücke zu einer Ladung zusammengefasst werden. Eine neue Version der Schmelzanlage kann bis zu 1.15 m lange Kernstücke aufnehmen.

Nach dem Zuschneiden der Kernstücke werden ihre Längsseiten mit einem Keramikmesser oder Mikrotom grob gereinigt, um anhaftende Fussel oder grobe Partikel zu entfernen. Denn schon kleine Verunreinigungen auf dem Schmelzkopf (auch im äußeren Bereich!) können die Schmelzgeschwindigkeit um über 50% reduzieren. Daher ist es wichtig, dass bei diesen Arbeitsschritten fasernde Textilhandschuhe (Wolle, Flies etc.) immer nur unter PE-Schutzhandschuhen getragen werden.

Beim Verarbeiten der Kernstücke ist es wichtig, dass die Stirnseiten von Kernstücken, die innerhalb einer Ladung aneinandergrenzen, plan und senkrecht zur Kernachse präpariert werden. Ist die Grenzfläche schräg, so können sich die Stücke unmittelbar am Schmelzkopf – unter dem Druck des darüber liegenden Eises – gegeneinander verschieben oder verdrehen, was zu Kontamination im inneren Schmelzkopfbereich führen kann. Außerdem müssen die Stirnseiten mit einem Skalpell oder Mikrotom dekontaminiert werden.

Jede Ladung beginnt mit einem ca. 5 cm langen Kunsteisstück aus mQ-Wasser (hochreines, vollentsalztes Wasser mit einer Leitfähigkeit $< 0.1$ $\mu$S/cm); dies hat mehrere Gründe: Zum einen hat sich das Ungleichgewicht der Temperatur am Schmelzkopf, das

zu Beginn jedes Schmelzvorgangs entsteht, innerhalb der ersten 5 cm ausgeglichen, so dass stabile Schmelzbedingungen herrschen, sobald echtes Kernmaterial geschmolzen wird. Zum anderen kann das Umschalten des Messsystems vom Leerlaufbetrieb (Nullwasser) auf den Messbetrieb (Probe) vorgenommen werden, während das mQ-Eis schmilzt; so kommen keine Luftblasen in das Analysesystem und es geht keine echte Probenflüssigkeit verloren.

Während der gesamten Vorbereitungsprozedur ist eine genaue Protokollierung der vorhandenen Lücken und der während der Vorbereitung entfernten Kernbereiche notwendig. Diese Information wird für die Tiefenzuweisung benötigt, die während der Datenauswertung erfolgt. Die messfertigen Kernstücke werden zusammen mit dem mQ-Eisstück in die vorgekühlten Plexiglasgleitrohre geschoben und für die Messung in das Kühlrohr der Schmelzapparatur eingeschoben.

Das Arbeiten mit der Schmelzapparatur ist nur dann zweckmäßig, wenn hinreichend lange Kernstücke vorhanden sind. Ist der Kern stark in kurze Stücke zerbrochen (etwa $< 15$ cm), dann steigt der Aufwand für die Kernvorbereitung und die Nachbearbeitung der Messprofile deutlich an; gleichzeitig werden die Profile der hochaufgelösten Messungen durch die Lücken an den Bruchstellen zunehmend unzusammenhängend, worunter die Interpretierbarkeit leidet. Große Lücken im Kernprofil entstehen auch an stark schräg verlaufenden oder splittrigen Brüchen oder auch an Stellen, die infolge eines Sägefehlers zu schmal geschnitten worden sind; denn solche Stellen oder Kernstückenden können nicht mit der Schmelzapparatur bearbeitet werden und müssen entfernt werden. In solchen Fällen kann durch eine konventionelle Kernvorbereitung, wie sie z.B. bei [*Fischer*, 1997] beschrieben wird, flexibler auf die jeweilige Situation eingegangen werden.

## B.6 Datenauswertung

Während des Schmelzvorgangs werden die Messdaten sekündlich als Spannungen aufgezeichnet; diese müssen im Zuge der Datenauswertung in Konzentrationen umgerechnet werden. Außerdem müssen die Messdaten einer bestimmten Kerntiefe zugeordnet werden. Diese Tiefenzuweisung, d.h. die Transformation von Laborzeit nach Kerntiefe, ist für jede Messkomponente unterschiedlich, da die Pumpzeiten der Probenflüssigkeit vom Schmelzkopf bis zur jeweiligen Nachweiskomponente unterschiedlich sind.

Für diese beiden Aufgaben (Kalibration und Tiefenzuweisung) wurde ebenfalls ein LabView Programm entwickelt (`"Datenauswertung.vi"`). Es liest die Rohdatenfiles ein und lässt den Benutzer für alle aufgezeichneten Komponenten diejenigen Messdaten

herausschneiden, die sich auf gemessenes Kernmaterial beziehen. Dies geschieht durch Setzen von Start– und Stopmarkern (Startmarker beim Konzentrationssprung von mQ-Eis zu Probe, Stopmarker am Kernende). Auf diese Weise kann die Zeitverzögerung zwischen Schmelzen und Messung für jede Komponente individuell korrigiert werden. Das ausgeschnittene Intervall jeder Komponente wird linear auf das Wegaufnehmer-Profil abgebildet; so wird in einem ersten Schritt jedem Messdatenpunkt eine Position innerhalb der Ladung des Schmelzdurchganges zugeordnet. In einem zweiten Schritt wird die Position innerhalb der Ladung in echte Kerntiefe überführt, wobei Daten aus dem Logging-Protokoll verwendet werden. In diesem zweiten Schritt wird fehlendes Kernmaterial an Brüchen berücksichtigt, indem an den entsprechenden Stellen "NaN" (für "not a number") eingetragen wird.

Die Umrechnung der Messdaten in Konzentrationen geschieht wie folgt: Beim Partikelzähler ist die aufgezeichnete Spannung proportional zur Zählrate (Partikel pro Sekunde); Division durch die Fließrate ergibt die Anzahlkonzentration (Partikel pro Milliliter). Die Ausgangsspannung des Leitfähigkeitsdetektors ist bis auf einen Versatz, der korrigiert werden muss, proportional zur Leitfähigkeit. Für die Kalibration der chemischen Nachweise ($Ca^{2+}$ und $NH_4^+$) wird das Spannungssignal der Basislinie sowie das eines Standards ausgewertet und daraus eine lineare Kennlinie bestimmt.

Nach erfolgter Tiefenzuweisung und Kalibration werden alle aufgenommenen Profile auf einer Tiefenachse synoptisch dargestellt. Dies ermöglicht das genaue Überprüfen der Tiefenzuweisung anhand von eindeutigen Ereignissen, die "gleichzeitig" in mehreren Nachweiskomponenten auftauchen. Hierzu kommen beispielsweise Signalstörungen durch Luftblasen oder Verunreinigungen an Brüchen in Frage oder prominente Einzelereignisse, die zu starken Peaks in mehreren Komponenten führen. Eine solche Überprüfung ist sinnvoll, wenn später Verhältnisse der verschiedenen Komponenten gebildet werden oder die relativen Phasenlagen der saisonalen Variabilitäten von verschiedenen Komponenten untersucht werden sollen. Wird festgestellt, dass die Tiefenzuweisung fehlerhaft war, so kann sie wiederholt werden. Das Datenauswertungsprogramm ermöglicht auch das Entfernen von offensichtlich fehlerhaften Messwerten aus einem oder aus mehreren Profilen (verursacht durch Luftblasen, Kontamination, Fehlfunktion etc.).

# Appendix C

# Die elektrolytische Leitfähigkeit

## C.1 Physikalische Grundlagen

Die elektrische Leitfähigkeit $\sigma$ einer Substanz ist der Proportionalitätsfaktor zwischen resultierender Stromdichte $\mathbf{j}$ und vorhandenem elektrischen Feld $\mathbf{E}$:

$$\mathbf{j} = \sigma \mathbf{E}.$$

Für die Leitfähigkeit gilt $\sigma = 1/\rho$ ($\rho$: spezifischer Widerstand); und mit $R = L/A \cdot \rho$ ($R$: ohmscher Widerstand, $L$: Länge und $A$: Querschnittsfläche eines leitenden Körpers) erhält man $\sigma = 1/R \cdot L/A$. Hieran werden die SI-Einheiten für die Leitfähigkeit deutlich: $[\sigma]$=Sm$^{-1}$.

Im Falle von Elektrolytlösungen wird die elektrische Leitfähigkeit durch die Wanderung der Ionen im elektrischen Feld bewirkt; man spricht von *elektrolytischer Leitfähigkeit*. Hier ist die Definition der auf die Konzentration $c$ bezogenen molaren Leitfähigkeit $\lambda_m$ sinnvoll: $\lambda_m = \sigma/c$. Mit abnehmender Konzentration nimmt $\lambda_m$ infolge einer Zunahme der elektrolytischen Dissoziation bzw. infolge einer Abnahme der elektrischen Kräfte zwischen den Ionen zu und nähert sich der *Leitfähigkeit in unendlicher Verdünnung* $\lambda_\infty$ (Grenzleitfähigkeit). Im Grenzfall der unendlichen Verdünnung sind die molaren Leitfähigkeiten konzentrationsunabhängig. Dieser wichtige Spezialfall ist für polare Eiskernproben gegeben. Dadurch ist hier die Gesamtleitfähigkeit eine Linearkombination der Ionenkonzentrationen und deren respektiven molaren Grenzleitfähigkeiten.

Für mehrwertige Elektrolyte definiert man die Äquivalenzleitfähigkeit $\lambda_{eq} = \lambda_m/z$ bzw. $\lambda_{eq,\infty} = \lambda_\infty/z$ ($z$: Wertigkeit). Die Äquivalenzleitfähigkeiten einiger für die Eisbohrkernanalytik wichtigen Ionen sind in Tabelle C.1 zusammengestellt. Die vergleichsweise hohen Leitfähigkeiten von $H^+$- und $OH^-$-Ionen sind auf einen unterschiedlichen

| Ionenart | Äquivalentleitfähigkeit $\lambda_{eq}$ [S mol$^{-1}$ cm$^2$] |
|---|---|
| **$H^+$** | **349.8** |
| $NH_4^+$ | 73.7 |
| $K^+$ | 73.5 |
| $Ca^{2+}$ | 59.8 |
| $Na^+$ | 55.1 |
| $Mg^{2+}$ | 53.0 |
| **$OH^-$** | **197** |
| $SO_4^{2-}$ | 80.0 |
| $Cl^-$ | 76.4 |
| $NO_3^-$ | 71.5 |
| $HCO_3^-$ | 44.5 |

Table C.1: Äquivalentleitfähigkeiten (bei unendlicher Verdünnung) einiger Ionenarten in wässriger Lösung bei 25$^o$C [*Linde*, 1995].

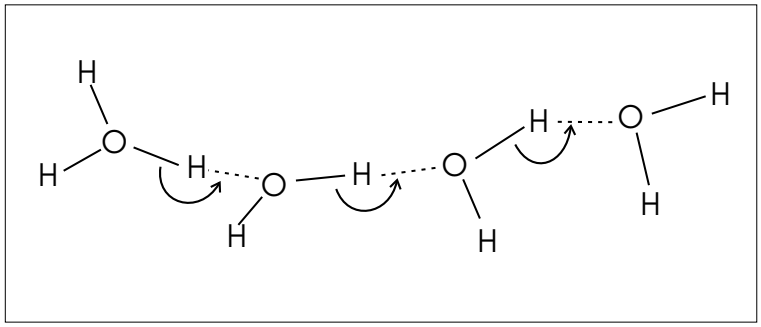


Figure C.1: Prinzip der Wanderladung von $H^+$-Ionen in wässriger Lösung.

Mechanismus des Ladungstransports zurückzuführen. Bei diesen Ionen wandert nicht das Ion selbst durch das Lösungsmittel, sondern der Ladungstransport kommt dadurch zustande, dass Protonen von einem Wassermolekül zum nächsten überspringen können. Dadurch muss kein Massetransport stattfinden. Dieser Sprungmechanismus, der nur für $H^+$- und $OH^-$-Ionen möglich ist, ist in Abbildung C.1 illustriert.

Die Leitfähigkeit von wässrigen Lösungen ist temperaturabhängig; denn mit der Temperatur steigt die Beweglichkeit der Ionen und damit die Leitfähigkeit. Angaben der Leitfähigkeit müssen daher auf eine bestimmte Temperatur bezogen werden; als Referenztemperatur wird üblicherweise 25$^o$C genommen. *Klein* [2001] hat die Temperaturabhängigkeit der elektrolytischen Leitfähigkeit verschiedener Polareisproben zu

$(2.0 \pm 0.2)\%$ $K^{-1}$ bestimmt.

## C.2 Durchflussmesszellen für den CFA- oder FIA-Betrieb

Die Leitfähigkeit eines Elektrolyten ist mit einem Elektrodenpaar bestimmbar, an dem eine Wechselspannung anliegt und das in die Lösung eingetaucht wird. Aus Spannung und Strom kann der Widerstand und mit Hilfe eines Geometriefaktors, der auch Zellkonstante genannt wird, die Leitfähigkeit der Lösung bestimmt werden. Die Zellkonstante muss experimentell ermittelt werden.

Im Rahmen dieser Arbeit wurde mit verschiedenen bereits existierenden Durchflussmesszellen experimentiert. Die Zellen unterschieden sich im Material (Glas, Plexiglas, Kunststoff), Bauform und Totvolumen. Es wurden selbst gebaute und kommerzielle Messzellen verwendet. Im Routinebetrieb am besten bewährt hat sich eine Messzelle der Fa. Dionex, die ein sehr kleines Totvolumen besitzt und auch temperaturkompensiert ist. Die selbstgebauten Zellen hatten zudem das Problem, dass sie nicht ideal auf die verwendeten Detektoren abgestimmt waren. Beim Selbstbau von Leitfähigkeitsmesszellen sollte möglichst nichtbenetzender Kunststoff verwendet und das Totvolumen so klein wie möglich gehalten werden. Gleichzeitig sollten die Elektroden großflächig sein und dicht beisammen liegen, d.h. die Zellkonstante sollte möglichst klein sein.

## C.3 Reduzierte Leitfähigkeit

Die Leitfähigkeit stellt einen Pauschalparameter für die ionischen Spurenstoffkonzentrationen einer Probe dar. Da gegenseitige Wechselwirkungen der Ionen untereinander für stark verdünnte Lösungen wie Polareisproben vernachlässigt werden können, ist die Leitfähigkeit $\sigma$ einer Polareisprobe die Summe der Leitfähigkeiten $\sigma_i$ der enthaltenen Elektrolyte. Mit den Konzentrationen $c_i$, Wertigkeiten $z_i$ und Äquivalenzleitfähigkeiten $\lambda_i$ gilt:

$$\sigma = \sum_i \sigma_i = \sum_i \lambda_i z_i c_i.$$

Bei Proben, deren Leitfähigkeit von einer Ionenart $i_0$ oder einer Gruppe $A$ von Ionen ($i \in A$) dominiert wird, kann es lohnen, den Leitfähigkeitsbeitrag dieser Ionenart oder Gruppe zu ermitteln und von der Gesamtleitfähigkeit abzuziehen. Die verbleibende

*reduzierte* Leitfähigkeit $\sigma_R$ trägt dann Informationen über die Konzentrationen aller übrigen Ionen:

$$\sigma_R = \sigma - \sum_{i \in A} \lambda_i z_i c_i = \sum_{i \notin A} \lambda_i z_i c_i.$$

Kennt man die Konzentrationen, Äquivalenzleitfähigkeiten und Wertigkeiten aller Komponenten von $A$, so lässt sich $\sigma_R$ aus $\sigma$ berechnen.

Einen Sonderfall stellt das Seesalzaerosol dar, denn die Konzentrationen der Seesalzkomponenten sind mit Ausnahme von Bicarbonat sehr gut proportional zueinander (von geringen Fraktionierungen abgesehen). Kennt man beispielsweise $\sigma$ und die Konzentration $c_j$ einer Seesalzkomponente, so kann – unter der Annahme dass $c_j$ rein maritimen Ursprungs ist – die reduzierte Leitfähigkeit in Bezug auf Seesalz, d.h. die nicht-Seesalz-Leitfähigkeit $\sigma_{nss}$, berechnet werden:

$$\sigma_{nss} = \sigma - a c_j$$

In der Praxis ist es sinnvoll, den Faktor $a$ nicht analytisch zu berechnen, sondern durch Messungen zu bestimmen.

# Appendix D

# Die Azidität

## D.1 pH-Wert und Azidität

### D.1.1 Der pH-Wert

Das übliche Maß für die Säuren- oder Basenstärke einer wässrigen Lösung ist der pH-Wert. Er stellt eine Quantifizierung des Arrhenius'-Konzepts der Säure mittels des Massenwirkungsgesetzes dar. Nach dem Arrhenius-Konzept bildet eine Säure in Wasser $H^+$- und eine Base $OH^-$-Ionen. Als quantitatives Maß für den Säuregrad wird die $H^+$-Konzentration $[H^+]$ genommen; der pH-Wert ist definiert als:

$$\mathrm{pH} = -\log_{10}[H^+].$$

In wässrigen Lösungen bei $25^oC$ gilt: $[H^+] \cdot [OH^-] = 1.008 \cdot 10^{-14}$ mol$^2$/l$^2$ (Autoprotolyse des Wassers). Ist die Lösung neutral, so ist $[H^+] = [OH^-] = 1.0 \cdot 10^{-7}$ mol/l, d.h. pH = 7; in sauren Lösungen ist $[H^+] > [OH^-]$, d.h. pH < 7; in basischen Lösungen ist $[H^+] < [OH^-]$, d.h. pH > 7.

Polareisproben bilden Lösungen mit geringer Pufferstärke; hier wird die $H^+$-Konzentration nicht nur durch die ursprünglich gelösten Substanzen bestimmt, sondern auch durch kleinste Mengen nachträglich hinzugefügter Säuren oder Basen. So kann atmosphärisches $CO_2$, das sich vor oder während der Messung zusätzlich zum a priori vorhandenen $CO_2$ in der flüssigen Probe löst, den pH-Wert der Probe verändern. Daher ist der pH-Wert kein geeignetes Maß für die Säurestärke von Polareisproben.

### D.1.2 Das Carbonat-System

Geht atmosphärisches $CO_2$ in Lösung, so bleibt der Großteil als Gas hydratisiert ($CO_{2,aq}$), und nur ein kleiner Teil reagiert zu Kohlensäure $H_2CO_3$, die anschließend

| Temperatur $^o$C | $-\log K_H$ | $-\log K_1$ | $-\log K_2$ |
|---|---|---|---|
| 0 | 1.11 | 6.58 | 10.63 |
| 5 | 1.19 | 6.52 | 10.56 |
| 10 | 1.27 | 6.46 | 10.49 |
| 15 | 1.34 | 6.42 | 10.43 |
| 20 | 1.41 | 6.38 | 10.38 |
| 25 | 1.46 | 6.35 | 10.33 |
| 30 | 1.52 | 6.33 | 10.29 |
| 40 | 1.62 | 6.30 | 10.22 |
| 50 | 1.71 | 6.29 | 10.17 |

Table D.1: Werte der Konstanten des Carbonat-Gleichgewichts für unendliche Verdünnung bei verschiedenen Temperaturen. Aus [*Hutzinger*, 1980].

dissoziiert:

$$CO_{2,Gas} + H_2O \longleftrightarrow CO_{2,aq} + H_2O \longleftrightarrow H_2CO_3 \longleftrightarrow H^+ + HCO_3^- \longleftrightarrow 2H^+ + CO_3^-$$

Häufig ist es schwierig, zwischen aquatisiertem $CO_2$-Gas ($CO_{2,aq}$) und dem echten Kohlensäuremolekül $H_2CO_3$ zu unterscheiden; daher hat es sich als nützlich erwiesen, die "scheinbare" oder "zusammengesetzte" Kohlensäure $H_2CO_3$* zu betrachten. Ihre Konzentration ist $[H_2CO_3^*] := [CO_{2,aq}] + [H_2CO_3]$. Da nur ca. 0.3 % des gelösten $CO_2$ in der Form $H_2CO_3$ vorliegen (bei $25^oC$), gilt: $[H_2CO_3^*] \approx [CO_{2,aq}]$ (siehe [*Sigg and Stumm*, 1991]). Hiermit lässt sich der Lösungsvorgang von $CO_2$ folgendermaßen beschreiben:

$$CO_{2,Gas} + H_2O \overset{(1)}{\longleftrightarrow} {H_2CO_3}^* \overset{(2)}{\longleftrightarrow} H^+ + HCO_3^- \overset{(3)}{\longleftrightarrow} 2H^+ + CO_3^-.$$

Dieses System ist durch folgende Gleichgewichte charakterisiert.

(1) $[H_2CO_3^*] = K_H \cdot p_{CO_2}$

(2) $[H^+] \cdot [HCO_3^-] = K_1 \cdot [H_2CO_3^*] \approx K_1 \cdot [CO_{2,aq}]$

(3) $[H^+] \cdot [CO_3^{2-}] = K_2 \cdot [HCO_3^-]$.

Tabelle D.1 zeigt eine Zusammenstellung der Gleichgewichtskonstanten. Für pH $< 9$ kann der zweite Dissoziationsschritt vernachlässigt werden [*Stumm and Morgan*, 1981]. Man kann daher vereinfachend schreiben:

$$CO_{2,Gas} + H_2O \longleftrightarrow H^+ + HCO_3^-.$$

| Bezeichnung | Definition |
|---|---|
| **Mineralische Azidität =** **– Alkalinität** | $[H^+] - [HCO_3^-] - 2[CO_3^{2-}] - [OH^-]$ |
| $CO_2$-Azidität = – p-Alkalinität | $[H_2CO_3^*] + [H^+] - [CO_3^{2-}] - [OH^-]$ |
| Azidität = – Caustische Alkalinität | $2[H_2CO_3^*] + [HCO_3^-] - [H^+] - [OH^-]$ |

Table D.2: Definition verschiedener Aziditäten.

Für durchschnittliche Außenluft mit $p_{CO_2} = 385$ ppmV erhält man mit den Werten aus Tabelle D.1 bei 25$^o$C: $[H_2CO_3^*] = 1.34 \cdot 10^{-5}$ mol/l und $[H^+] \approx \sqrt{K_1[H_2CO_3^*]} = 2.44 \cdot 10^{-6}$ mol/l, oder pH = 5.61.

### D.1.3 Die Azidität

Da der pH-Wert anfällig gegen "$CO_2$-Kontamination" und daher nicht zur Beschreibung der Säurestärke von Polareisproben geeignet ist, muss ein konservatives Maß gefunden werden, das robust gegenüber Veränderungen der Menge an gelöstem $CO_2$ ist. Hier kann das Konzept der Azidität und Alkalinität angewandt werden. Azidität und Alkalinität werden auch "base neutralizing capacity" (BNC) bzw. "acid neutralizing capacity" (ANC) genannt. Früher wurden sie ausschließlich durch Titration bestimmt; daher unterscheidet man je nach Endpunkt der Titration verschiedene Definitionen (zur Erläuterung der Endpunkte siehe [*Stumm and Morgan*, 1981]). In Tabelle D.2 sind die verschiedenen Definitionen zusammengestellt.

Im folgenden wird ausschließlich die *mineralische Azidität* bzw. die normale Alkalinität verwendet. Für Polareisproben kann der zweite Dissoziationsschritt wieder vernachlässigt und außerdem $[OH^-] \ll [HCO_3^-]$ angenommen werden. Dadurch vereinfacht sich die Definition der (mineralischen) Azidität $S$ zu: $S = [H^+] - [HCO_3^-]$ .

Im allgemeinen Gebrauch [*Weddeling*, 1991; *Kolb*, 1995; *Hausbrand*, 1998; *Armbruster*, 2000] hat es sich mittlerweile eingebürgert, die "negative normale Alkalinität" schlicht "Azidität" zu nennen, d.h. den Zusatz "mineralisch" wegzulassen. Dies ist zwar nicht konform mit der klassischen Definition, doch da die klassisch definierte Azidität in dieser Arbeit nicht verwendet wird, besteht keine Verwechslungsgefahr. Daher wird auch im folgenden so verfahren.

Man erkennt, dass der Wert der Azidität robust gegen Zugabe von $CO_2$ ist; denn

beim Lösungsvorgang $CO_2 + H_2O \longrightarrow H^+ + HCO_3^-$ nehmen $[H^+]$ und $[HCO_3^-]$ beide zu, und an der Azidität, in die nur die Differenz $[H^+] - [HCO_3^-]$ eingeht, ändert sich nichts. Vereinfachend kann gesagt werden, dass die Azidität gleich der $H^+$-Konzentration ist, die nicht durch gelöstes $CO_2$ verursacht worden ist, d.h. $S = [H^+_{\text{gesamt}}] - [H^+_{CO_2}] = [H^+_{\text{gesamt}}] - [HCO_3^-]$.

Der Vorteil der Azidität gegenüber dem pH-Wert ist also die Unabhängigkeit von der jeweiligen $CO_2$-Konzentration der Lösung. Wohingegen der pH-Wert von reinem Wasser unter Schutzgasatmosphäre 7.0 beträgt, im Gleichgewicht mit der Umgebungsluft aber nur $\approx 5.6$, ist die Azidität in beiden Fällen gleich (nämlich Null). Im Falle eines $CO_2$-freien Systems ist die Azidität gleich dem entfalteten pH-Wert, d.h. $S = 10^{-\text{pH}_{CO_2-\text{frei}}}$.

Zwischen pH-Wert und Azidität $S$ kann folgender formaler Zusammenhang abgeleitet werden:

$$S = [H^+] - [HCO_3^-]$$

$$S = 10^{-\text{pH}} - \frac{K_1[H_2CO_3^*]}{[H^+]} = 10^{-\text{pH}} - K_1 K_H p_{CO_2} 10^{\text{pH}}$$

Mit dem Ionenprodukt der Kohlensäure $L = K_1 K_H p_{CO_2} \approx 10^{-11.22 \frac{\text{mol}^2}{\text{l}}}$ (bei $25^o$C und $p_{CO_2} = 385$ ppmV) erhält man:

$$S = 10^{-\text{pH}} - L \cdot 10^{\text{pH}}. \tag{D.1}$$

Die Umkehrfunktion hierzu lautet mit $\text{pL} = -\log_{10} L$:

$$\text{pH} = \frac{1}{\ln 10} \text{arsinh}\left(\frac{-S}{2\sqrt{L}}\right) + \frac{\text{pL}}{2}. \tag{D.2}$$

Bei Kenntnis von $L$ lassen sich also pH-Wert und Azidität ineinander umrechnen.

## D.2 Messung der Azidität

### D.2.1 Grundlagen

Die Bestimmung der Azidität erfolgt häufig durch Titration. Dabei wird nicht nur bis zu einem fixen Endpunkt titriert, sondern eine Gran-Titration durchgeführt [*Sigg and Stumm*, 1991; *Legrand*, 1980]. Dieses Verfahren lässt sich aber nicht – oder nur schwierig – an bereits bestehende Messsysteme wie IC oder die Schmelzapparatur ankoppeln. Eine weitere Methode zur Bestimmung der Azidität ist eine pH-Messung

bei konstantem $p_{CO_2}$. Diese wird bevorzugt, da sie als Fließ-Injektions-Analyse (FIA) betrieben und an einen Ionenchromatographen angekoppelt werden kann [*Kolb*, 1995]. Nach Bestimmung des pH-Werts der Probe bei bekanntem $p_{CO_2}$ wird der Messwert in die Azidität überführt, um ein robustes Maß der $H^+$-Konzentration zu erhalten. Dazu könnte theoretisch mit Gleichung D.1 die Azidität aus dem pH-Wert und aus $p_{CO_2}$ berechnet werden. Da aber im vorliegenden Aufbau die Probe verdünnt wird und außerdem das Messgerät während der FIA-Messung keinen Gleichgewichtszustand erreicht, ist es notwendig, die theoretische Beziehung von Gleichung D.1 durch eine Kalibration zu ersetzen (siehe Abschnitt D.2.3).

Im allgemeinen besteht die große Schwierigkeit der Aziditätsmessung darin, den pH-Wert einer nur sehr schwach leitenden, hochverdünnten Lösung zu bestimmen. Dies hat lange Einstellzeiten der Elektrodenpotentiale und eine hohe Störanfälligkeit gegenüber Fremdeinflüssen zur Folge.

### D.2.2 Messaufbau

Der hier verwendete Messaufbau wurde in Zusammenarbeit mit *Armbruster* [2000] erstellt. Es wurde dabei auf den Aufbau von *Hausbrand* [1998] zurückgegriffen, doch wurde ein anderes pH-Meter verwendet, wodurch auch Änderungen am Schlauchsystem notwendig wurden.

Die Messung basiert auf der Ableitung einer Potentialdifferenz, die sich je nach Verwendung an einer ionenselektiven Membranelektrode oder an einer Glaselektrode einstellt. An der Oberfläche der Elektrode streifen die $H^+$-Ionen ihre Hydrathülle ab und diffundieren in das Membransystem, während die entgegengesetzt geladenen Ionen wegen der sie umhüllenden Wassermoleküle nicht folgen können. Es bildet sich dadurch eine Potentialdifferenz aus, die pro pH-Einheit 59.2 mV beträgt (*Nernst'sche Gleichung*).

Das verwendete pH-Meter der Firma *ZABS GmbH*, Marburg, ist bereits bei [*Armbruster*, 2000] beschrieben worden. Es ist ein Durchfluss-pH-Meter, das in einem FIA-Aufbau an das IC-Gerät gekoppelt wurde. Da der elektrische Eingang der Potentialableitung einen sehr hohen Innenwiderstand besitzt (ca. $10^{15}$ Ω), führen bereits kleinste Ladungsverschiebungen zu deutlichen Spannungssignalen. Dies schlägt sich in einer sehr hohen Störanfälligkeit gegenüber Fremdeinflüssen nieder, die beim Betrieb unbedingt berücksichtigt werden müssen. So ist eine galvanische Entkopplung und eine Druckentkopplung zwischen dem Pumpsystem und der Messelektrode durch eine Tropfenkammer notwendig. Außerdem ist eine geerdete Abschirmung des Messeingangs sowie eine Erdung der Probenflüssigkeit (!) in der Tropfenkammer notwendig.

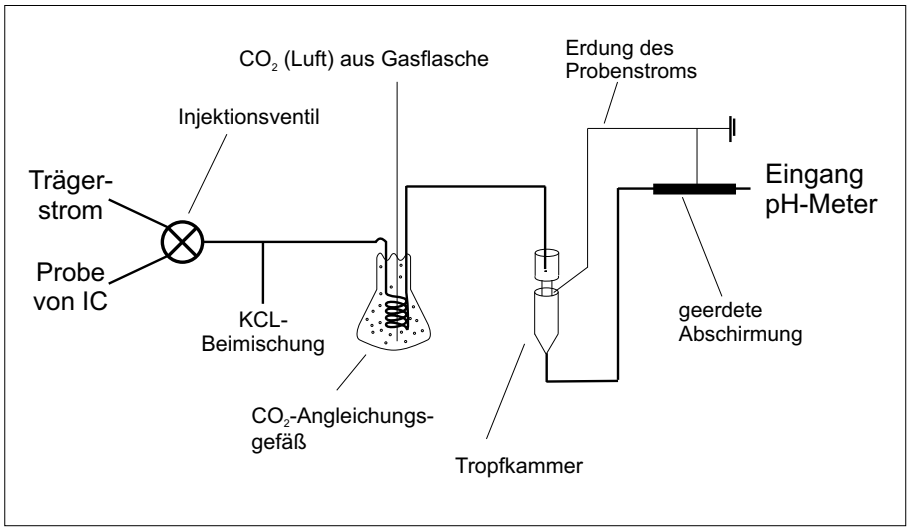


Figure D.1: Ankopplung der Aziditätsmessung an das IC-Gerät. Verändert und ergänzt nach [*Armbruster*, 2000].

Um das Signalrauschen zu verringern wurde die Leitfähigkeit der Messlösung durch dosierte KCl-Beimischung erhöht. Abbildung D.1 zeigt den schematischen Aufbau des Fließsystems der Aziditätsmessung.

Um den Einfluss von gelöstem $CO_2$ aus der Umgebungsluft auf die pH-Messung eliminieren zu können, wird bei konstantem $p_{CO_2}$ gearbeitet. Dazu durchfließt die Probe in einem 2 m langen dünnwandigen Silikonschlauch ein Angleichungsgefäß. Dieses enthält ein Wasserreservoir, das sich im Lösungsgleichgewicht mit konstantem Luft-$CO_2$ befindet. Durch die dünne Wand des Silikonschlauches hindurch findet eine Angleichung der $CO_2$-Konzentration in der Probe statt, so dass die $CO_2$-Konzentration bei allen Proben gleich ist. Durch Kalibration mittels präparierter Standards bekannter Azidität, die ebenfalls dem $CO_2$-Angleich unterworfen werden, kann der Einfluss von Luft-$CO_2$ ausgeschaltet werden.

Die KCl-Zugabe zur Probe ist nötig, um das Rauschen zu vermindern. Allerdings wird durch die KCl-Zugabe auch die Signalhöhe vermindert. Abbildung D.2 zeigt die Veränderung der Signalhöhe und des Rauschens bei unterschiedlichen Konzentrationen der beigemischten KCl-Lösung. Die Fließraten bei der Mischung betrugen 0.30 ml/min für die KCl-Lösung und 0.88 ml/min für den Probenstrom. Als Referenzsignal wurde die Differenz der Peakhöhe eines $-8.0$ $\mu$eq/l-Standards und eines 8.2 $\mu$eq/l-Standards verwendet. Man erkennt, dass die Signalhöhe oberhalb einer KCl-Leitfähigkeit von 10 $\mu$S/cm abnimmt. Dagegen ist das Rauschen erst ab ca. 100 $\mu$S/cm klein genug, um die Datenauswertung nicht mehr zu behindern. Daher wurde als Arbeitspunkt eine

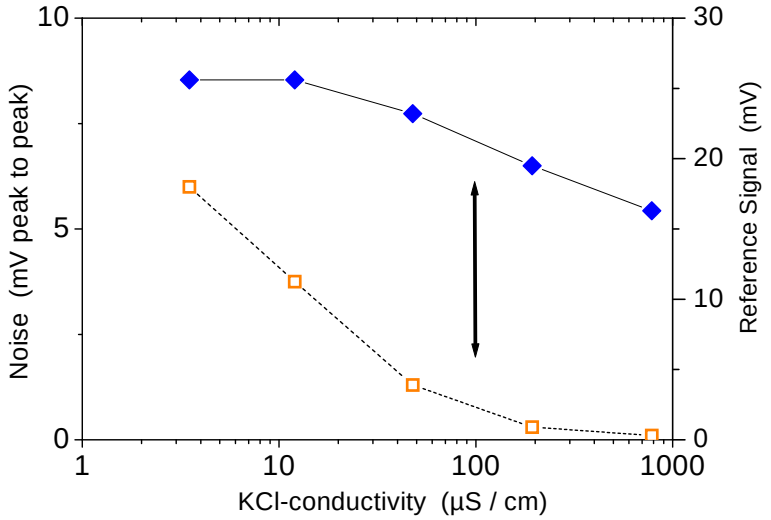


Figure D.2: Veränderung von Rauschen (offene Symbole, linke Achse) und Signalhöhe (ausgefüllte Symbole, rechte Achse) bei Zugabe von KCl unterschiedlicher Konzentration. Der Pfeil markiert den optimalen Arbeitspunkt bei ca. 100 $\mu$S/cm. Siehe Text für Detailinformationen.

KCl-Konzentration von ca. 0.08 mmol/l (entsprechend ca. 100 $\mu$S/cm) gewählt.

### D.2.3 Kalibration

Zur Kalibration werden Standards mit bekannter Azidität verwendet. Dabei kommen stark verdünnte, wässrige Lösungen von $H_2SO_4$ und NaOH zum Einsatz. Diese Standards haben ein ähnliches Pufferverhalten wie die Polareisproben gegenüber $CO_2$-Eintrag aus der Umgebung. Ferner können kommerzielle Pufferlösungen wegen ihrer hohen Ionenstärke nicht verwendet werden, weil dies ein unterschiedliches Ansprechverhalten der Messelektroden bewirkt.

Abbildung D.3 zeigt den Potentialverlauf eines sauren und eines basischen Standards. Die Messkurven können entweder über die Peakhöhe oder die Peakfläche ausgewertet werden. Hierbei bringt die Auswertung über die Peakfläche mehrere Vorteile. Zum einen ist das Verhältnis von Peakhöhe zu Peakbreite bei sauren und basischen Proben unterschiedlich, wodurch sich die Peak*höhe* bei sauren und basischen Proben asymmetrisch ändert; dagegen ändert sich die Peak*fläche* bei sauren und basischen Proben symmetrisch. Wird daher über die Peakhöhe ausgewertet, so führt dies zu unterschiedlichen Steigungen im sauren und basischen Ast der Kalibrationskurve. Wird dagegen über die Peakfläche ausgewertet, so erhält man eine über große Bereiche symmetrische Kalibrationskurve.

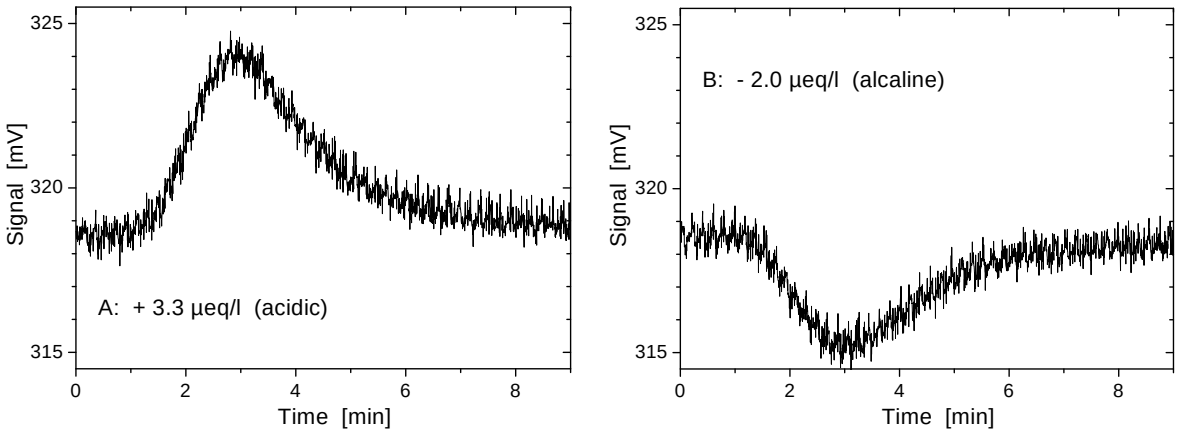


Figure D.3: Beispiele zur Aziditätsmessung. Gezeigt ist der Potentialverlauf eines sauren (A) und eines basischen (B) Standards mittlerer Stärke.

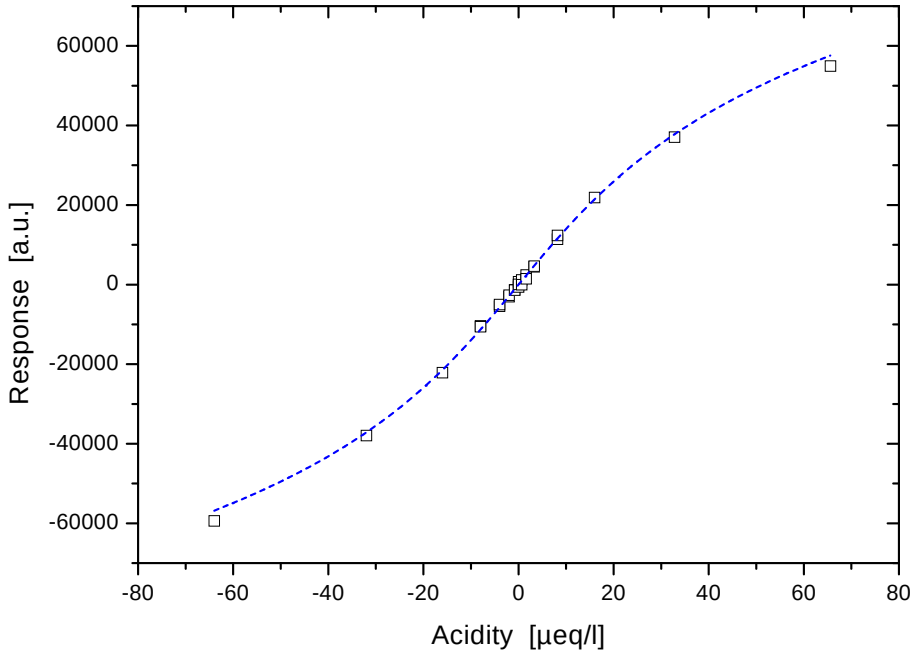


Figure D.4: Kennlinie der Aziditätsmessung. Durch Auswertung der Peakfläche erhält man die erwartete, symmetrische Kurve.

Eine Kalibrationskurve, die durch Auswertung der Peakfläche gewonnen wurde, ist in Abbildung D.4 gezeigt. Dargestellt sind die Messpunkte einer Serie von Standardmessungen und eine durch Parameteroptimierung angepasste Fit-Funktion. Da die Signalantwort und der pH-Wert linear miteinander verknüpft sind, kann mittels Gleichung D.2 als Fit-Funktion $y = c + a \cdot \operatorname{arcsinh}(b \cdot x)$ gewählt werden. Da ferner nur die Signalveränderungen gegenüber der Basislinie ausgewertet werden und die Basislinie

einer neutralen Probe entspricht, gilt zudem $c = 0$.

Ein weiterer Vorteil der Auswertung über die Peakfläche ist, dass gelegentlich auftretende Über- oder Unterschwinger nicht fälschlich als Messkurvenmaxima oder -minima interpretiert werden, wie dies bei früheren Arbeiten regelmäßig der Fall gewesen war.

# Bibliography


Abbatt, J. P. D., Interaction of HNO3 with water-ice surfaces at temperatures of the free troposphere, *Geophysical Research Letters, 24*(12), 1479–1482, 1997.

Aitchison, J., and J. A. C. Brown, *The Longnormal Distribution*, University of Cambridge, Cambridge, 1957.

Alfaro, S. C., and L. Gomes, Modeling mineral aerosol production by wind erosion: emission intensities and aerosol size distributions in source areas, *Journal of Geophysical Research, 106*(D16), 18075–18084, 2001.

Andersen, K. K., A. Armengaud, and C. Genthon, Atmospheric dust under glacial and interglacial conditions, *Geophysical Research Letters, 25*(13), 2281–2284, 1998.

Andersen, K. K., and P. D. Ditlevsen, Glacial - interglacial variations of meridional transport and washout of dust: a one-dimensional model, *Journal of Geophysical Research, 103*(D8), 8955–8962, 1998.

Armbruster, M., 2000, *Stratigraphical dating of high Alpine ice cores over the last 1000 years (in German)*, M.Sc. thesis, University of Heidelberg.

Bagnold, R., *The Physics of Blown Sand and Desert Dunes*, Methuen, London, 1941.

Bay, R. C., B. P. Price, G. D. Clow, and A. J. Gow, Climate logging with a new rapid optical technique at Siple Dome, *Geophysical Research Letters, 28*(24), 4635–4638, 2001.

Bigler, M., 2000, *Entwicklung und Anwendung einer neuen Methode zur kontinuierlichen, hochaufgelösten Messung der Sulfatkonzentration an alpinen und polaren Eisbohrkernen*, M.Sc. thesis, University of Berne.

Bigler, M., 2002, *Dissertation in preparation*, Ph.D. thesis, University of Berne.

Biscaye, P. E., F. E. Grousset, M. Revel, S. Van der Gaast, G. A. Zielinski, A. Vaars, and G. Kukla, Asian provencance of glacial dust (stage 2) in the Greenland Ice Sheet Project 2 ice core, Summit, Greenland, *Journal of Geophysical Research, 102*(C12), 26765–26781, 1997.

Boutron, C., 1978, *Influences of aerosols of natural and antropogenic origin on the chemistry of polar snows (in French)*, Ph.D. thesis, University of Grenoble.

Bowen, H. J. M., *Environmental Chemistry of the Elements*, Academic Press, London, 1979.

Cadle, R. D., *Particle Size Determination*, Interscience Publishers, New York London, 1955.

Chylek, P., G. Lesins, and U. Lohmann, Enhancement of dust source area during past glacial periods due to changes of the Hadley circulation, *Journal of Geophysical Research, 106*(D16), 18477–18485, 2001.

Clausen, H. B., C. U. Hammer, C. S. Hvidberg, D. Dahl-Jensen, J. P. Steffensen, J. Kipfstuhl, and M. Legrand, A comparison of the volcanic records over the past 4000 years from the Greenland Ice Core Project and Dye 3 Greenland ice cores, *Journal of Geophysical Research, 102*(C12), 26707–26723, 1997.

Clausen, H. B., and C. C. Langway, The ionic deposits in polar ice cores, in *The Environmental Record in Glaciers and Ice Sheets*, edited by H. Oeschger and C. C. Langway Jr., pp. 225–247, Wiley, New York, 1989.

Colin, J. L., B. Lim, E. Herms, F. Genet, E. Drab, J. L. Jaffrezo, and C. I. Davidson, Air-to-snow mineral transfer – crustal elements in aerosols, fresh snow and snowpits on the Greenland ice sheet, *Atmospheric Environment, 31*(20), 3395–3406, 1997.

Cragin, J. H., M. M. Herron, C. C. Langway Jr., and G. Klouda, Interhemisheric comparison of changes in the composition of atmospheric precipitation during the late Cenozoic era, in *Polar Oceans*, edited by M. J. Dunbar, pp. 617–631, Arctic Institute of North America, Calgary, AB, Canada, 1977.

D'Almeida, Guillaume, A., and L. Schütz, Number, mass and volume distributions of mineral aerosol and soils of the Sahara, *Journal of Climate and Applied Meteorology, 22*, 233–243, 1983.

Dansgaard, W., S. J. Johnsen, J. Møller, and C. C. Langway Jr., One thousand centuries of climatic record from Camp Century on the Greenland ice sheet, *Science, 166*, 377–381, 1969.

Davidson, C. I., M. H. Bergin, and H. D. Kuhns, The deposition of particles and gases to ice sheets, in *Chemical Exchange Between the Atmosphere and Polar Snow*, edited by E. W. Wolff and R. C. Beales, pp. 275–306, Springer Verlag, Berlin Heidelberg, 1996.

Davies, C. N., Size distribution of atmospheric particles, *Aerosol Science, 5*, 293–300, 1974.

De Angelis, M., M. Legrand, J. R. Petit, N. I. Barkov, Y. S. Korotkevitch, and V. M. Kotlyakov, Soluble and insoluble impurities along the 950 m deep Vostok ice core (Antarctica) - climatic implications, *Journal of Atmospheric Chemistry, 1*, 215–239, 1984.

De Angelis, M., J. P. Steffensen, M. Legrand, H. Clausen, and C. Hammer, Primary aerosol (sea salt and soil dust) deposited in greenland ice during the last climatic cycle: Comparison with east antarctic records, *Journal of Geophysical Research, 102*(C12), 26681–26698, 1997.

Delmonte, B., J. R. Petit, and V. Maggi, Glacial to Holocene implications of the new 27,000-year dust record from the EPICA Dome C (East Antarctica) ice core., *Climate Dynamics,*, in press, 2002.

Dibb, J. E., J. W. Talbot, J. W. Munger, D. J. Jacob, and M. Fan, S, Air-snow exchange of HNO3 and NOy at Summit, Greenland, *Journal of Geophysical Research, 103*(D3), 3475–3486, 1998.

Dibb, J. E., R. W. Talbot, and M. H. Bergin, Soluble acidic speecies in air and snow at Summit, Greenland, *Geophysical Research Letters, 21*(15), 1627–1630, 1994.

Dubowski, V., A. J. Colussi, and M. R. Hoffmann, Nitrogen dioxid release in the 302 nm band photolysis of spray-frozen aqueous nitrate solutions. Atmospheric implications, *Journal of Physical Chemistry, 105*(20), 4928–4932, 2001.

Felzer, B., Climate impacts of an ice sheet in East Siberia during the Last Glacial Maximum, *Quaternary Science Reviews, 20*, 437–447, 2001.

Fischer, H., 1997, *Spacial Variability in Ice Core Time Series of North East Greenland (in German)*, Ph.D. thesis, University of Heidelberg.

Fischer, H., and D. Wagenbach, Large-scale spatial trends in recent firn chemistry along an east-west transect through central Greenland, *Atmospheric Environment, 30*(19), 3227–3238, 1996.

Fischer, H., D. Wagenbach, and J. Kipfstuhl, Sulfate and nitrate firn concentrations on the Greenland ice sheet 1. Large-scale geographical deposition changes, *Journal of Geophysical Research, 103*(D17), 21927–21934, 1998.

Fuchs, N. A., *The Mechanics of Aerosols*, Pergamon Press, Oxford, London, Edinburgh, New York, Paris, Frankfurt, 1964.

Fuhrer, K., E. W. Wolff, and S. J. Johnsen, Timescales for dust variability in the Greenland Ice Core Projct (GRIP) ice core in the last 100,000 years, *Journal of Geophysical Research, 104*(D24), 31043–31052, 1999.

Geis, K., 1988, *Concentration and Size Distribution of Microscopical Particles in Ice Cores from High Alpine Glaciers: First Results with a Electrosensorical Measuring Technique (in German)*, M.Sc. thesis, University of Heidelberg.

Gillette, D. A., J. Adams, A. Endo, and D. Smith, Threshold velocities for input of soil particles into the air by desert soils, *Journal of Geophysical Research, 85*(C10), 5621–5630, 1980.

Gillette, D. A., I. H. J. Blifford, and D. W. Fryrear, The influence of wind velocity on the size distributions of aerosols generated by the wind erosion of soils, *Journal of Geophysical Research, 79*(27), 4068–4075, 1974.

Gillette, D. A., and R. Passi, Modelling dust emission causd by wind erosion, *Journal of Geophysical Research, 93*(D11), 14233–14242, 1988.

Grootes, P. M., and M. Stuiver, Oxygen 18/16 variability in Greenland snow and ice with 10-3 - to 10-5 -year time resolution, *Journal of Geophysical Research, 102*(C12), 26,455–26,470, 1997.

Grousset, F. E., P. E. Biscaye, M. Revel, J. R. Petit, K. Pye, S. Joussaume, and J. Jousel, Antarctic (dome c) ice core dust at 18 k.y. BP: isotopic constraints and origins, *Earth and Planetary Science Letters, 111*, 175–182, 1992.

Hammer, C. U., Dating of Greenland ice cores by microparticle concentration analyses, in *Isotopes and Impurities in Snow and Ice*, pp. 297–301, IAHS-AISH publication no. 118, Grenoble, 1977.

Hammer, C. U., H. B. Clausen, W. Dansgaard, A. Neftel, P. Kristinsdottir, and E. Johnson, Continuous impurity analysis along the Dye 3 deep core, in *Greenland Ice Core: Geophysics, Geochemistry, and the Environment*, edited by C. C. Langway Jr., H. Oeschger, and W. Dansgaard, Volume 33 of *Geophysical Monograph 33*, pp. 90–94, American Geophysical Union, Washington, 1985.

Hanisch, F., and J. N. Crowley, Heterogeneous reactivity of gaseous nitric acid on A1203 CaCO3 and atmospheric dust samples: A Knudsen cell study, *Journal of Physical Chemistry, 105*(13), 3096–3106, 2001.

Hansson, M. E., The Renland ice core. A Nothern hemisphere record of aerosol composition over 120'000 years, *Tellus, 46B*, 390–418, 1994.

Harder, S. L., S. G. Warren, R. J. Charlson, and D. S. Covert, Filtering of air through snow as a mechanism for aerosol deposition to the Antarctic ice sheet, *Journal of Geophysical Research, 101*(D13), 18729–18743, 1996.

Hauglustaine, D. A., C. Granier, G. P. Brasseur, and G. Mgie, The importance of atmospheric chemistry in the calculation of radiative forcing on the climate system, *Journal of Geophysical Research, 99*(D1), 1173–1184, 1994.

Hausbrand, R., 1998, *Direktmessung der Azidität in einem Eisbohrkern aus Nordwestgrönland*, M.Sc. thesis, University of Heidelberg.

Herdan, G., and M. L. Smith, *Small Particles Statistics*, Elsevier Publishing Company, Amsterdam Houston New York Paris, 1953.

Herron, M. H., Impurity sources of F-, Cl-, NO3-, SO4- in Greenland and Antarctic precipitation, *Journal of Geophysical Research, 87*(C4), 3052–3060, 1982.

Hinkley, T., F. Pertsiger, and L. Zavjalova, The modern atmospheric background dust load: recognition in Central Asian snowpack, and compositional contraints, *Geophysical Research Letters, 24*(13), 1607–1610, 1997.

Honrath, R. E., S. Guo, M. C. Peterson, M. P. Dziobak, J. E. Dibb, and M. A. Arsenault, Photochemical production of gas phase NOx from ice chrystal NO3-, *Journal of Geophysical Research, 105*(D19), 24183–24190, 2000.

Hua, L., 1999, *An integrated wind erosion modelling system with emphasis on dust emission and transport*, Ph.D. thesis, University of New South Wales.

Hutzinger, O., *The Handbook of Environmental Chemistry*, Springer Verlag, Heidelberg, 1980.

Janecek, T. R., and D. K. Rea, Quaternary fluctuations in the northern hemisphere trade winds and westerlies, *Quaternary Reasearch, 24*, 150–163, 1985.

Johnsen, S. J., H. B. Clausen, W. Dansgaard, N. S. Gundestrup, C. U. Hammer, U. Andersen, K. K. Andersen, C. S. Hvidberg, D. Dahl-Jensen, J. P. Steffensen, H. Shoji, A. E. Sveinbjrnsdttir, J. W. C. White, J. Jouzel, and D. Fisher, The $\delta^{18}$O record along the Greenland Ice Core Project deep ice core and the problem of possible Eemian climatic instability, *Journal of Geophysical Research, 102*(C12), 26397–26410, 1997.

Jones, A. E., R. Weller, A. Minikin, E. W. Wolff, W. T. Sturges, H. P. McIntyre, S. R. Leonard, O. Schrems, and S. Bauguitte, Oxidized nitrogen chemistry and speciation in the Antarctic troposphere, *Journal of Geophysical Research, 104*(D17), 21355–21366, 1999.

Jones, A. E., R. Weller, E. W. Wolff, and H. W. Jacobi, Speciation and rate of photochemical NO and NO2 production in Antarctic snow, *Geophysical Research Letters, 27*(3), 345–348, 2000.

Junge, C., The importance of mineral dust as an atmospheric constituant, in *Saharan Dust*, edited by C. Morales, pp. 49–60, John Wiley and Sons, New York, 1979.

Junge, C. E., *Air Chemistry and Radioactivity*, Academic Press, New York, 1963.

Junge, C. E., Processes responsible for the trace content in precipitation, in *Isotopes and Impurities in Ice and Snow*, IAHS-AISH publication no. 118, Grenoble, 1977.

Kahl, J. D. W., D. A. Martinez, H. Kuhns, C. I. Davidson, J.-L. Jaffrezo, and J. M. Harris, Air mass trajectories to Summit, Greenland: A 44-year climatology and some episodic events, *Journal of Geophysical Research, 102*(C12), 26861–26875, 1997.

Kapsner, W. R., R. B. Alley, C. A. Shuman, S. Anandakrishnan, and P. M. Grootes, Dominant influence of atmospheric circulation on snow accumulation in Greenland over the past 18,000 years, *Nature, 373*, 52–54, 1995.

Klein, J., 2001, *Rezente Verteilung der Aerosoldeposition auf einem hochalpinen Firnsattel*, Staatsexamensarbeit, University of Heidelberg.

Kolb, L., 1995, *Einsatz einer Schmelzsonde zur Probennahme und Routinemessung von Leitfähigkeit und Azidität von Eisbohrkernen*, M.Sc. thesis, University of Heidelberg.

Kreutz, K. J., and P. A. Mayewski, Spatial variability of Antarctic surface snow glaciochemistry: implications for palaeoatmospheric circulation reconstructions, *Antarctic Science, 11*(1), 105–108, 1999.

Krinner, G., and C. Genthon, GCM simulations of the Last Glacial Maximum surface climate of Greenland and Antarctica, *Climate Dynamics, 14*, 741–758, 1998.

Lagroix, F., and S. K. Banerjee, Paleowind directions from the magnetic fabric of loess profiles in central Alaska, *Earth and Planetary Science Letters, 195*, 99–112, 2002.

Lamy, F., D. Hebbeln, and G. Wefer, High-resolution marine records of climatic change in mid-latitude Chile during the last 28,000 years based on terrigenous sediment parameters, *Quaternary Research, 51*, 83–93, 1999.

Legrand, M., 1980, *Measurement of Acidity And Electrical Conductivity of Antarctic Precipitations (in French)*, Ph.D. thesis, University of Grenoble.

Legrand, M., and S. Kirchner, Origins and variations of nitrate in South Polar precipitation, *Journal of Geophysical Research, 95*(D4), 3493–3507, 1990.

Legrand, M., E. Wolff, and D. Wagenbach, Antarctic aerosol and snow fall chemistry: Implications for deep Antarctic ice core chemistry, *Annals of Glaciology, 29*, 66–72, 1999.

Linde, D. R., *Handbook of Chemistry and Physics*, CRC-press, 1995.

Maggi, V., Mineralogy of atmospheric microparticles deposited along the Greenland Ice Core Project ice core, *Journal of Geophysical Research, 102*(C12), 26725–26734, 1997.

Mahowald, N., K. Kohfeld, M. Hansson, Y. Balkanski, S. P. Harrison, I. C. Prentice, M. Schulz, and H. Rodhe, Dust sources and deposition during the last glacial maximum and current climate: a comparison of model results with paleodata from ice cores and marine sediments, *Journal of Geophysical Research, 104*(D13), 15895–15916, 1999.

Mayewski, P. A., W. B. Lyons, M. J. Spencer, M. S. Twickler, C. F. Buck, and S. Whitlow, An ice-core record of atmospheric response to anthropogenic sulphate and nitrate, *Nature, 346*, 554–556, 1990.

Meese, D. A., A. J. Gow, R. B. Alley, G. A. Zielinski, P. M. Grootes, M. Ram, K. C. Taylor, P. A. Mayewski, and J. F. Bolzan, The Greenland Ice Sheet Project 2 depth-age scale: methods and results, *Journal of Geophysical Research, 102*(C12), 26411–26423, 1997.

Mulvaney, R., D. Wagenbach, and E. W. Wolff, Postdepositional change in snowpack nitrate from observation of year-round near-surface snow in coastal Antarctica, *Journal of Geophysical Research, 103*(D9), 11021–11031, 1998.

Mulvaney, R., and E. W. Wolff, Spatial variability of the major chemistry of the Antarctic ice sheet, *Annals of Glaciology, 20*, 440–447, 1994.

Narita, H., Specific surface of deposited snow ii, *Low Temperature Science, A29*, 69–81, 1971.

Neftel, A., J. Beer, H. Oeschger, F. Zürcher, and C. Finkel, Sulphate and nitrate concentrations in snow from South Greenland 1895-1978, *Nature, 314*, 611–613, 1985.

Nicholson, K. W., The dry deposition of small particles: a review of experimental measurements, *Atmospheric Enviroment, 22*(12), 2653–2666, 1988.

Patterson, E. M., and D. A. Gillette, Commonalities in measured size distributions for aerosols having a soil-derived component, *Journal of Geophysical Research, 82*(15), 2074–2082, 1977.

Petit, J.-R., M. Briat, and A. Royer, Ice age aerosol content from East Antarctic ice core samples and past wind strenght, *Nature, 293*, 391–394, 1981.

Petit, J. R., J. Jouzel, D. Raynaud, N. Barkov, J.-M. Barnola, I. Basile, M. Bender, J. Chappellaz, M. Davis, G. Delaygue, M. Delmotte, V. M. Kotlyakov, M. Legrand, V. Y. Lipenkov, C. Lorius, L. Ppin, C. Ritz, E. Saltzmann, and M. Stievenard, Climatic and atmospheric history of the past 420,000 years from the Vostok ice core, Antarctica, *Nature, 399*, 429–436, 1999.

Petit, J. R., L. Mounier, J. Jouzel, Y. S. Korotkevich, V. I. Kotlyakov, and C. Lorius, Palaeoclimatological and chronological implications of the Vostok core dust record, *Nature, 343*, 56–58, 1990.

Porter, S. C., and A. Zhisheng, Correlation between climate events in the North Atlantic and China during the last glaciation, *Nature, 375*, 305–308, 1995.

Prospero, J. M., R. J. Charlson, V. Mohnen, R. Jaenicke, A. C. Delany, J. Moyers, W. Zoller, and K. Rahn, The atmospheric aerosol systen: an overview, *Reviews of Geophysics and Space Physics, 21*(7), 1607–1629, 1983.

Pye, K., *Aeolian dust and dust deposits*, Academic Press, London, 1987.

Rahn, K. A., and R. D. Borys, The Asian source of Arctic haze bands, *Nature, 268*, 713–715, 1977.

Ram, M., and M. Illing, Polar ice stratigraphy from laser-light scattering: scattering from meltwater, *Journal of Glaciology, 40*(136), 504–508, 1994.

Ram, M., and G. Koenig, Continuous dust concentration profile of pre-Holocene ice from the Greenland Ice Sheet Projct 2 ice core: dust stadials, interstadials, and the Eemian, *Journal of Geophysical Research, 102*(C12), 26641–26648, 1997.

Ramanathan, V., P. J. Crutzen, J. T. Kiehl, and D. Rosenfeld, Aerosols, climate, and the hydrological cycle, *Science, 294*, 2119–2124, 2001.

Rea, D. K., The paleoclimatic record provided by eolian deposition in the deep sea: the geologic history of wind, *Reviews of Geophysics, 32*(2), 159–195, 1994.

Röthlisberger, R., M. Bigler, A. Hutterli, S. Sommer, B. Stauffer, H. G. Junghans, and D. Wagenbach, Technique for continious high-resolution analysis of trace substances in firn and ice cores, *Environmental Science Technology, 34*, 338–342, 2000.

Röthlisberger, R., A. Hutterli, S. Sommer, E. W. Wolff, and R. Mulvaney, Factors controlling nitrate in ice cores: Evidence from the Dome C deep ice core, *Journal of Geophysical Research, 105*(D16), 20565–20572, 2000.

Royer, A., M. De Angelis, and J. R. Petit, A 30000 year record of physical and optical properties of microparticles from an East Antarctic ice core and implications for paleoclimate reconstruction models, *Climate Change, 4*, 381–412, 1983.

Ruth, U., D. Wagenbach, M. Bigler, J. P. Steffensen, and R. Röthlisberger, High resolution dust profiles at NGRIP: case studies of the calcium-dust relationship, *Annals of Glaciology, 35*, in press, 2002.

Saey, P., 1998, *Concentration and size distribution of microparticles in Alpine and polar ice cores (in German)*, M.Sc. thesis, University of Heidelberg.

Sarnthein, M., Sand deserts during glacial maximum and climatic optimum, *Nature, 272*, 43–46, 1978.

Sehmel, G. A., Particle and gas dry deposition: a review, *Atmospheric Enviroment, 14*, 983–1011, 1980.

Seinfeld, J. P., and S. N. Pandis, *Atmospheric Chemistry and Physics*, Wiley, New York, 1998.

Sigg, L., and W. Stumm, *Aquatische Chemie*, B. G. Teubner Verlag, Stuttgart, 1991.

Sokolik, I. N., D. M. Winker, G. Bergametti, D. A. Gillette, G. Carmichael, Y. J. Kaufman, L. Gomes, L. Schuetz, and J. E. Penner, Introduction to special section: Outstanding problems in quantifying the radiative impacts of mineral dust, *Jourmal of Geophysical Research, 106*(D16), 18015–18027, 2001.

Sommer, S., 2000, *Klimainformation chemischer Spurenstoffe in polaren Eisbohrkernen*, Ph.D. thesis, University of Bern.

Stanzick, A., 2001, *Space-Time-Variations of $^{10}Be$, $^{210}Pb$, and $^{36}Cl$ in the Greenlandic Firn Cover: Air-Firn-Transfer and Recent Trends*, Ph.D. thesis, University of Heidelberg.

Steffensen, J. P., Microparticles in snow from the south greenland ice sheet, *Tellus, 37B*, 286–295, 1985.

Steffensen, J. P., Analysis of the seasonal variation in dust, Cl, NO3 and SO4 in two Central Greenland firn cores, *annals of Glaciology, 10*, 171–177, 1988.

Steffensen, J. P., 1995, *Microparticles and chemical impurities in ice cores from Dye 3, South Greenland and their interpretation in palaeoclimatic reconstructions*, Ph.D. thesis, University of Copenhagen.

Steffensen, J. P., The size distribution of microparticles from selected segments of the Greenland Ice Core Project ice core representing different climatic periods, *Journal of Geophysical Research, 102*(C12), 26755–26763, 1997.

Steffensen, J. P., H. B. Clausen, and J. M. Christensen, On the spatial variability of impurity content and stable isotopic composition in recent summit snow, in *Chemical*

*exchange between the atmosphere and polar snow*, edited by E. W. Wolff and R. C. Bales, Volume I 43 of *NATO ASI*, pp. 607–615, Springer Verlag, Berlin Heidelberg, 1996.

Stumm, W., and J. J. Morgan, *Aquatic Chemistry*, John Wiley and Sons, New York, 1981.

Sugimae, A., Elemental constituents of atmospheric particulates and particle density, *Nature, 307*, 145–147, 1984.

Svensson, A., P. E. Biscaye, and F. E. Grousset, Characterization of late glacial continental dust in the Greenland Ice Core Projct ice core, *Journal of Geophysical Research, 105*(D24), 4637–4656, 2000.

Taylor, K. C., R. B. Alley, G. W. Lamorey, and P. Mayewski, Electrical measurements on the Greenland Ice Sheet Project 2 Core, *Journal of Geophysical Research, 102*(C12), 26511–26517, 1997.

Tegen, I., and I. Fung, Modeling of mineral dust in the atmosphere: sources, transport, and optical thickness, *Journal of Geophysical Research, 99*(D11), 22897–22914, 1994.

Tegen, I., and D. Rind, Influence of the latitudinal temperature gradient on soil dust concentration and deposition in Greenland, *Journal of Geophysical Research, 105*(D6), 7199–7212, 2000.

Thibert, E., and F. Domin, Thermodynamics and kinetics of the solid solution of HNO3 in ice, *Journal of Physical Chemistry B, 102*, 4432–4439, 1998.

Thompson, L. G., and E. Mosley-Thompson, Microparticle concentration variations linked with climatic change: Evidence from polar ice cores, *Science, 212*, 812–815, 1981.

Unnerstad, L., and M. Hansson, Simulated airborne particle size distributions over Greenland during Last Glacial Maximum, *Geophysical Research Letters, 28*(2), 287–290, 2001.

Wagenbach, D., and K. Geis, The mineral dust record in a high altitude Alpine glacier (Colle Gnifetti, Swiss Alps), in *Paleoclimatology and Paleometeorology: Modern and Past Patterns of Global Atmospheric Transprot*, edited by M. Leinen and M. Sarnthein, pp. 543–564, Kluwer, 1989.

Wang, Y. J., H. Cheng, R. L. Edwards, Z. S. An, J. Y. Wu, C.-C. Shen, and J. A. D'Orale, A high-resolution absolute-dated late pleistocene Monsoon record from Hulu cave, China, *Science, 294*, 2345–2348, 2001.

Weddeling, P., 1991, *Ionische Zusammensetzung und Säuregehalt eines hochalpinen Firnsattels*, M.Sc. thesis, University of Heidelberg.

Werner, M., U. Mikolajewicz, M. Heimann, and G. Hoffmann, Borehole versus isotope temperatures on Greenland: seasonality does matter, *Geophysical Research Letters, 27*(5), 723–726, 2000.

Wesely, M. L., and B. B. Hicks, A review of the current status of knowledge on dry deposition, *Atmospheric Environment, 34*, 2261–2282, 2000.

Wolff, E. W., Nitrate in polar ice, in *Ice core sudies of global biochemical cycles*, edited by R. J. Delmas, Volume I 30 of *NATO ASI*, pp. 195–224, Springer Verlag, Berlin, 1995.

Wolff, G. T., On the nature of nitrate in coarse continental aerosols, *Atmospheric Environment, 18*(5), 977–981, 1984.

Wurzler, S., T. G. Reisin, and Z. Levin, Modification of mineral dust particles by cloud processing and subsequent effects on drop size distributions, *Journal of Geophysical Research, 105*(D4), 4501–4512, 2000.

Yang, Q., P. Mayewski, S. Whitlow, M. Twickler, M. Morrison, R. Talbot, J. Dibb, and E. Linder, Global perspective of nitrate flux in ice cores, *Journal of Geophysical Research, 101*(D3), 5113–5121, 1995.

Yang, Q., P. A. Mayewski, E. Linder, S. Whitlow, and M. Twickler, Chemical species spatial distribution and relationship to elevation and snow accumulation rate over the Greenland ice sheet, *Journal of Geophysical Research, 101*(D13), 18629–18637, 1996.

Zielinski, G. A., Paleoenvironmental implications of the insoluble microparticle record in the GISP2 (Greenland) ice core during the rapidly changing climate of the Pleistocene-Holocene transition, *Geological Society of America Bulletin, 109*(5), 547–559, 1997.

# Dank

Viele Personen haben auf ganz unterschiedliche Weise zu dieser Arbeit beigetragen. Freunden, Familie und Kollegen danke ich für ihre vielfältige Unterstützung.

Mein ganz besonderer Dank gilt Dr. Dietmar Wagenbach. Er hat die Arbeit im Alltag betreut, und durch sein umweltphysikalisches Einfühlungsvermögen hat sie sehr gewonnen. Außerdem hat Dietmar mein Verständnis von Umweltphysik nachhaltig geprägt und mir zu manch philosophischer Einsicht verholfen.

Prof. Dr. H. Miller hat als Schirmherr dieser Arbeit in entscheidenden Augenblicken weittragende Entscheidungen getroffen und mir zur Beteiligung an mehreren hochinteressanten Projekten verholfen. Für diese Weitsicht danke ich ihm ebenso wie für das große Vertrauen, das er mir bei vielen Entscheidungen entgegengebracht hat. Sein schier unübertrefflicher Optimismus hat mich sehr beeindruckt.

Prof. Dr. K. Herterich danke ich für die freundliche Übernahme des Koreferats und für das ausgeprägte Interesse, das er für meine Arbeit hatte.

Prof. Dr. U. Bleil, Prof. Dr. H. Villinger, Dr. Hubertus Fischer, Dr. Andre Paul, Dr. Karl Fabian, Claudia Piel und Marie-Louise Siggard-Andersen danke ich für ihre Bereitschaft, in der Prüfungskomission mitzuwirken.

Meinen netten Kollegen am Institut für Umweltphysik (IUP) der Universität Heidelberg, am Alfred-Wegener-Institut (AWI), an der Uni Bern, am British-Antarctic-Survey und an der Uni Kopenhagen möchte ich dafür danken, dass sie wirklich nette Kollegen waren. Dies waren insbesondere (um zumindest einige namentlich zu nennen): Michael Huke, Christoph von Roden, Lothar Keck, Marc Armbruster, Martin Schock, Ronny Friedrich, Andreas Stanzick, Paul Saey, Hubertus Fischer, Fidan Goektas, Hans Oerther, Sepp Kipfstuhl, Uwe Nixdorf, Birgit Mieding, Marie-Louise Siggard-Andersen, Andreas Frenzel, Fernando Valero, Matthias Bigler, Regine Roethlisberger, Stefan Sommer, Eric Wolff, Rob Mulvaney, J.P. Steffensen und viele andere.

Unvergessliche Erlebnisse waren die Feldexpeditionen zur Probennahme nach Zentralgrönland, Severnaya Semlya und in die Alpen. In diesem Zusammenhang werde ich besonders Lothar Keck, Heiri Rufli, Susanne Preunkert und Diedrich Fritzsche noch lange in guter Erinnerung behalten. Matthias Bigler und Regine Roethlisberger danke ich darüber hinaus für die ganz ausserordentlich gute Zusammenarbeit vor, während und nach der NGRIP-2000 Feldsaison.

Diese Arbeit fand im Rahmen einer Kooperation zwischen dem AWI und dem IUP statt und wurde dadurch auch erst ermöglicht. Den Initiatoren und Trägern dieser Kooperation möchte ich an dieser Stelle ausdrücklich danken.

# Abbreviations

| | |
|---|---|
| AWI | Alfred-Wegener-Institut for Polar and Marine Research, Bremerhaven |
| ACR | Antarctic Cold Reversal |
| B/A | Bølling/Allerød |
| CC | Coulter Counter |
| CFA | Continuous Flow Analysis |
| D/O | Dansgaard-Oeschger |
| Dome-C | Dome-Concordia, Antarctica |
| EPICA | European Project for Ice Coring in Antarctica |
| FIA | Flow Injection Analysis |
| IC | Ion Chromatography |
| IS | Interstadial |
| GISP/2 | Greenland Ice Sheet Project |
| GRIP | Greenland Ice Core Project |
| IUP | Institut für Umweltphysik, University of Heidelberg |
| LGM | Last Glacial Maximum |
| LS | Laser Sensor |
| MIS | Marine Isotope Stage |
| MND | Mean Number Diameter |
| mQ | milli-Q (ultra-pure water) |
| MVD | Mean Volume Diameter |
| NaN | Not a Number |
| NGRIP | North Greenland Ice Core Project |
| ppb | parts per billion by mass ($= 10^{-9}$) |
| ppmV | parts per million by volume ($= 10^{-6}$) |
| Preb. | Preboreal |
| TTL | Transistor Transistor Logic |
| YD | Younger Dryas |